

PHASE 2 - 2D SEISMIC INVESTIGATION IGNACE AREA, REPORT

APM-REP-01332-0308

July 2022

VIBROMETRIC

nwmo

NUCLEAR WASTE
MANAGEMENT
ORGANIZATION

SOCIÉTÉ DE GESTION
DES DÉCHETS
NUCLÉAIRES



Nuclear Waste Management Organization
22 St. Clair Avenue East, 4th Floor
Toronto, Ontario
M4T 2S3
Canada

Tel: 416-934-9814
Web: www.nwmo.ca



Phase 2

2D Seismic Investigations, Ignace Area, Report

NWMO Document #:
APM-REP-01332-0308

2022

*By Nicoleta Enescu and Calin Cosma
for*

NWMO, Canada

CLIENT INFORMATION

Project Name: 2D seismic reflection planning, acquisition, processing and interpretation in granitoid bedrock in Northwestern Ontario (Ignace, Ontario)

NWMO Document Number: APM-REP-01332-0308

Client PO Number: 2000476

Document ID: NWMO_Ignace2Dseismics

Client: Nuclear Waste Management Organization (NWMO)
22 St. Clair Avenue East, 6th Floor
Toronto, Ontario, Canada, M4T 2S3

Client Contact: Mostafa Khorshidi and Maria Sánchez-Rico Castejón
Email: mkhorshidi@nwmo.ca and msanchez@nwmo.ca

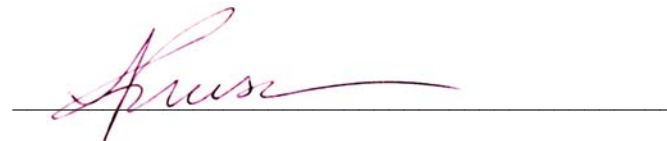
ISSUE / REVISION INDEX

Issue Code	Revision					Revision details
	No.	By	Rev'd	App	Date	
RR	1	NE			15 Nov. 2021	Draft of factual report released for review and comments
RR	2		MK		29 Nov. 2021	NWMO comments
RR	3	NE			27 Dec. 2021	Draft of factual report released for review and comments
RR	4		MK, AD		14 Jan. 2022	NWMO comments / change of scope
RR	5	NE		CC	06 Apr. 2022	Draft of report for publishing, released for review and comment
RR	6		MK, AD, MS		20 Apr. 2022	NWMO comments
RR	7	NE		CC	23 May 2022	Final Draft of report for publishing released for review and comments
RR	8	NE		CC	17 June 2022	Final report for publishing released for review and comments
RI	9	NE		CC	18 July 2022	Final report for publishing released for information

Issue codes: RR = Released for Review and comments, RI = Released for Information

SIGNATURES

Prepared by:



Nicoleta Enescu, Ph.D. – Senior Geophysicist

Approved by:



Calin Cosma, Ph.D. – Senior Geophysicist – Project Manager

Contents

1	INTRODUCTION.....	8
1.1	GEOLOGICAL SETTING	8
1.2	SUPPORTING GEOLOGICAL DATA.....	10
1.3	OBJECTIVES OF THE SEISMIC SURVEY	11
2	FIELD ACTIVITIES.....	12
2.1	FIELD EQUIPMENT	12
2.1.1	<i>Seismic source VIBSIST-3000.....</i>	<i>12</i>
2.1.2	<i>Seismic Receivers and Data recorder.....</i>	<i>14</i>
2.2	SEISMIC SURVEY.....	15
2.2.1	<i>Survey Design</i>	<i>15</i>
2.2.2	<i>Survey Parameters.....</i>	<i>17</i>
3	2D DATA PROCESSING	19
3.1	DECODING THE VIBSIST IMPACT SEQUENCES.....	19
3.2	PRECONDITIONING OF THE DATA PROFILES	21
3.3	ARRIVAL TIME PICKING AND FIRST STAGE REFRACTION STATICS	23
3.4	VELOCITY ANALYSIS, 3D TOMOGRAPHIC INVERSIONS FOR P WAVE VELOCITY IN THE NEAR SURFACE.....	25
3.5	STATIC CORRECTIONS	27
3.6	CONDITIONING OF THE DATA PROFILES	29
3.6.1	<i>Removal of direct wave fields</i>	<i>29</i>
3.6.2	<i>Image Point filtering and reflector enhancement.....</i>	<i>31</i>
3.7	MIGRATED PROFILES POSITIONING AND DATUM.....	32
3.8	3D KIRCHHOFF MIGRATION & 3D CMP RADON MIGRATION	33
3.8.1	<i>3D migrations, Line 1</i>	<i>39</i>
3.8.2	<i>3D migrations, Line 1.1</i>	<i>40</i>
3.8.3	<i>3D migrations, Line 1.2</i>	<i>41</i>
3.8.4	<i>3D migrations, Line 2</i>	<i>42</i>
3.8.5	<i>3D migrations, Line 3</i>	<i>43</i>
3.8.6	<i>3D migrations, Line 3.1</i>	<i>44</i>
3.8.7	<i>3D migrations, Line 4</i>	<i>45</i>
3.8.8	<i>3D migrations, Line 5</i>	<i>46</i>
4	REFLECTOR INTERPRETATION AND POSITIONING	47
4.1	VALIDATION OF REFLECTORS IN MULTIPLE SEISMIC LINES	53
4.1.1	<i>Line 1.1 and Line 1.2</i>	<i>53</i>
4.1.2	<i>All Seismic Lines.....</i>	<i>55</i>
4.2	SHALLOW OFF-LINE REFLECTIONS.....	58
5	SUMMARY	62
6	REFERENCES.....	64
APPENDIX A.	SYNTHETIC SEISMOGRAMS.....	66
APPENDIX B.	THE CMP RADON 3D MIGRATION METHOD.....	71
APPENDIX C.	KIRCHHOFF MIGRATED SECTIONS	74
APPENDIX D.	REFLECTOR INTERPRETATION	79

List of Figures

Figure 1. Geological map of the Revell Batholith and study area for the Revell Site. Data from three boreholes (IG_BH01, IG_BH02 and IG_BH03) were incorporated in this report to provide an initial assessment of the subsurface bedrock geology at the Revell Site. Drilling had completed in IG_BH04, however the results from this borehole were still preliminary at the time of this interpretation and were not used to constrain the interpretation at this time.9

Figure 2. VIBSIST-3000 source being used on Line 4..... 13

Figure 3. Installation of the acquisition system in the field, both on the line extensions (top) and along the lines (bottom). 14

Figure 4. The acquisition recorder truck in the field and operator during acquisition. 15

Figure 5. Map of planned seismic lines: Line 1 (green), Line 2 (magenta), Line 3 (dark green), Line 3-1 (red), Line 4 (brown) and Line 5 (blue) to be covered with both sources and receivers, while the line paddings (all shown in orange) were only covered with receivers. 16

Figure 6. Map of the measured seismic lines, similar to the one shown in Figure 5. Sources are shown in red and receivers are shown in blue. Line extensions were only covered with receivers. 17

Figure 7. Example of a section of a coded impact sequence from a field record. Axes are Time (ms) and Length (m) (same as in Figure 8)..... 20

Figure 8. Decoded impact sequence, raw data profile recorded from one source location (source 20, Line1)..... 20

Figure 9. Line 1: average spectra (left) and average spectra in a window before the ground-roll arrival (right) at two different locations along the line. 21

Figure 10. Line 1: average spectra (left) and average spectra in a window before ground-roll (right) at two adjacent receiver locations along the line, receiver 250 is shown on top and receiver 251 is shown in the bottom. 22

Figure 11. Same as in Figure 8, band pass filtered in the 20 – 50 Hz (left) and in the 20 – 160 Hz (right) frequency band. 22

Figure 12. Picked arrival times (cyan) for a receiver gather for source 20 on Line 1. 23

Figure 13. Same as in Figure 12, with a reduced velocity display, with $V = 6000$ m/s. 23

Figure 14. Same as in Figure 13, without the display of picked first arrival times. 24

Figure 15. Same as in Figure 14, after applying first stage static corrections. 24

Figure 16. View from top of the 2D lines and their best fit planar approximations (shown as straight lines), with two options for Line 1 (top: entire line was fitted; bottom: this line was split into two, overlapping sections: Line1.1 and Line1.2), which is the longest and most crooked. Easting and Northing labels show reduced coordinates (after removal of least significant digits: 5480000 was subtracted on Northing and 550000 was subtracted on Easting). 25

Figure 17. P wave velocity in the near surface along the 2D lines, from top to bottom: Line 1.1, Line 1.2, Line 2, Line 3, Line 3.1, Line 4 and Line 5. The velocity scale is the same for all lines, from 3100 m/s (red) to 6100 m/s (blue). 26

Figure 18. 3D view of the near surface P wave velocity derived on: (a) best fit linearly approximated crooked lines, (b) linear best-fit line approximations and 3D crooked line representations, and (c) velocity reconstruction along crooked lines. Easting and Northing show reduced coordinates (after removal of least significant digits) and the color scale is the same as in Figure 17, from 3100 m/s (red) to 6100 m/s (blue). 27

Figure 19. Receiver gather for source 20 on Line 1, before (left) and after (right) static corrections were applied and datum set at -75m below surface. 28

Figure 20. Receiver gather for source 20 on Line 1, after static corrections were applied and with arrival times computed on the P wave velocity field derived by tomographic inversion (shown in Figure 17) and with the datum set at -75m below surface.28

Figure 21. Receiver gather for source 20 on Line 1, after removal of shear (V_s 2900 – 3400 m/s) and surface wave fields (V_{surf} 1900 – 2300 m/s).30

Figure 22. Same as in Figure 21, after removal of compression wave field.....30

Figure 23. Same as in Figure 22, after amplitude equalization & trace balancing.31

Figure 24. Same as in Figure 22, after amplitude equalization and Image Point filtering.32

Figure 25. Line 1.2, Kirchhoff migration (with amplitude equalization & trace balancing)...34

Figure 26. Line1.2 3D CMP Radon migration, (with amplitude equalization & trace balancing).34

Figure 27. Same as in Figure 26, with band pass filtering and spectral equalization.35

Figure 28. 3D migration oriented to different directions around the migration axis. 0 denotes vertical down direction below the migration axis, while ± 10 , ± 20 and ± 30 mark the directions 10° , 20° and 30° laterally up from vertical, on both sides of the vertical down plane.36

Figure 29. Line 1.2 migrated section, with $V_p=5750$ m/s, together with the reflectivity log along borehole IG_BH01 and the near surface velocity profile along the same line. Depth scale is as shown in Figure 35.....37

Figure 30. Line 1.2 migrated section, with $V_p=6000$ m/s, together with the reflectivity log along borehole IG_BH01 and the near surface velocity profile along the same line. Depth scale is as shown in Figure 35.....37

Figure 31. Line1 3D CMP Radon migration with amplitude equalization & trace balancing.39

Figure 32. Same as in Figure 31, with bi-dimensional band pass filtering and spectral equalization.39

Figure 33. Line1.1 3D CMP Radon migration, with amplitude equalization & trace balancing.40

Figure 34. Same as in Figure 33, with bi-dimensional band pass filtering and spectral equalization.40

Figure 35. Line 1.2 3D CMP Radon migration with amplitude equalization & trace balancing.41

Figure 36. Same as in Figure 35, with bi-dimensional band pass filtering and spectral equalization.41

Figure 37. Line 2 3D CMP Radon migration with amplitude equalization & trace balancing.42

Figure 38. Same as in Figure 37, with bi-dimensional band pass filtering and spectral equalization.42

Figure 39. Line 3 3D CMP Radon migration with amplitude equalization & trace balancing.43

Figure 40. Same as in Figure 39, with bi-dimensional band pass filtering and spectral equalization.43

Figure 41. Line 3.1 3D CMP Radon migration with amplitude equalization & trace balancing.44

Figure 42. Same as in Figure 41, with bi-dimensional band pass filtering and spectral equalization.44

Figure 43. Line 4 3D CMP Radon migration with amplitude equalization & trace balancing.45

Figure 44. Same as in Figure 43, with bi-dimensional band pass filtering and spectral equalization.45

Figure 45. Line 5 3D CMP Radon migration with amplitude equalization & trace balancing.46

Figure 46. Same as in Figure 45, with bi-dimensional band pass filtering and spectral equalization.	46
Figure 47. Full-band migrated profiles viewed from the S-SE. Scale bar is in meters.	49
Figure 48. High band pass filtered migrated profiles viewed from the S-SE. Scale bar is in meters.	50
Figure 49. Full-band migrated profiles viewed from the N-NW. Scale bar is in meters.	51
Figure 50. High band pass filtered migrated profiles viewed from the N-NW. Scale bar is in meters.	52
Figure 51. 3D view of migrated sections for Line 1.1 (same as in Figure 34) and Line 1.2 (same as in Figure 36), together with the seismic reflectivity log along borehole IG-BH01. View from S-SW.	54
Figure 52. 3D view of migrated sections for Line 1.1 (same as in Figure 34) and Line 1.2 (same as in Figure 36), together with the seismic reflectivity log along borehole IG-BH01 and the interpreted seismic reflectors. View from S-SW.	54
Figure 53. 3D view from S-SE of the bi-dimensional high-pass migrated profiles from all 2D lines, with the interpreted seismic reflectors.	56
Figure 54. 3D view from N-NW of the bi-dimensional high-pass migrated profiles from all 2D lines, with the interpreted seismic reflectors.	57
Figure 55. Tomographic reconstruction of the P wave velocity in the near surface along Line 5 with overlaid refracted rays for one source and all receivers. The velocity scale is the same for all lines, from 3100 m/s (red) to 6100 m/s (blue).	58
Figure 56. 3D view of the horizontally migrated profiles from Line 1.2 and Line 4, together with the steeply dipping dyke (red).	59
Figure 57. View from top of the horizontally migrated profiles from Line 1.2 and Line 4, together with the steeply dipping dyke (red).	60
Figure 58. Wavelets and their amplitude and phase spectra for the minimum phase wavelets used for generating the synthetic seismograms for the Ignace site boreholes.	66
Figure 59. Zoeppritz synthetics along borehole IG_BH01, on a time interval from 0 to 360 ms, corresponding to a TVD interval from 70 to 1000m. Colored lines on the 10 – 150 Hz CDP gather mark inclined incidence angles (15, 25, 35 and 45 degrees) with respect to the vertical (shown as the yellow line, labeled 0). The next synthetic gathers were computed in the 10 – 100 Hz and 10 – 50 Hz bands, respectively.	66
Figure 60. Line 1.2 migrated section (middle), with the synthetic seismograms along borehole IG_BH01, in depth (TVD), on the left the lower frequency synthetic gather (10 – 50 Hz) and on the right the higher synthetic gather (10 – 100 Hz) on which the amphibolite “marker” reflector at 665.93m (this depth corresponds to peak amplitude of the reflector) in borehole IG_BH01 is underlined by the green dot and arrow. This “marker” reflector corresponds to the prominent density log variation at 660m, as seen in Figure 61.	67
Figure 61. Borehole IG-BH01 logs: S & P wave velocities, density and reflectivity.	68
Figure 62. Borehole IG-BH02 logs: S & P wave velocities, density and reflectivity.	69
Figure 63. Borehole IG-BH03 logs: S & P wave velocities, density and reflectivity.	70
Figure 64. Line 1, Kirchhoff migration with amplitude equalization & trace balancing.	74
Figure 65. Line 1.1, Kirchhoff migration with amplitude equalization & trace balancing.	75
Figure 66. Line 1.2, Kirchhoff migration with amplitude equalization & trace balancing.	75
Figure 67. Line 2, Kirchhoff migration with amplitude equalization & trace balancing.	76
Figure 68. Line 3, Kirchhoff migration with amplitude equalization & trace balancing.	77
Figure 69. Line 3.1, Kirchhoff migration with amplitude equalization & trace balancing.	77
Figure 70. Line 4, Kirchhoff migration with amplitude equalization & trace balancing.	78
Figure 71. Line 5, Kirchhoff migration with amplitude equalization & trace balancing.	78
Figure 72. Interpreted seismic reflectors on Line 1.1 (same as in Figure 34), view from SE.	79

- Figure 73. Interpreted seismic reflectors on Line 1.2 (same as in Figure 36), together with the seismic reflectivity log along borehole IG-BH01 (also shown in Figure 61), view from SW.79
- Figure 74. Interpreted seismic reflectors on Line 2 (same as in Figure 38), together with the seismic reflectivity log along borehole IG_BH03 (also shown in Figure 63), view from E. ..80
- Figure 75. Interpreted seismic reflectors on Line 3 (same as in Figure 40), view from S.....80
- Figure 76. Interpreted seismic reflectors on Line 3.1 (same as in Figure 42) together with the seismic reflectivity log along borehole IG_BH02 (also shown in Figure 62), view from E. ..81
- Figure 77. Interpreted seismic reflectors on Line 4 (same as in Figure 44), view from NE. ..81
- Figure 78. Interpreted seismic reflectors on Line 5 (same as in Figure 46), view from E.82

List of Tables

Table 1. VIBSIST-3000 Specifications.	13
Table 2- Estimated 2D seismic line lengths with extensions.....	16
Table 3- Measured lengths of the 2D seismic lines, with extensions.	18
Table 4. Processing sequence for the crooked 2D lines.....	19
Table 5. Processing sequence for removal of direct waves arrivals.	29
Table 6. Processing line elevations for the midlines of the migrated 2D profiles.	33

1 Introduction

This report documents the results from a newly acquired 2D seismic reflection survey within the Revell Batholith. This survey is completed as part of Phase 2 Geoscientific Preliminary Field Investigations of the NWMO's Adaptive Phased Management (APM) Site Selection Phase (NWMO, 2010). Execution of the survey included planning, acquisition, processing and interpretation of 2D seismic reflection data near a series of drilled boreholes in the northern portion of the Revell Batholith in an effort to better understand the subsurface conditions away from the boreholes.

The regional bedrock geology including the Revell Batholith is presented in Section 1.1. Section 1.2 summarizes the geological data sets that were useful in supporting the interpretation of seismic reflection data. Sections 1.1 and 1.2 have been contributed by NWMO, through personal communications (NWMO, 2022, email communication, 14 Jan.)

This report describes all stages of the project, with details on the work done for acquisition, processing and interpretation of six 2D seismic reflection lines, used to target and image geologic features in the subsurface, with a particular focus on imaging gently dipping structures in the top 1500 m.

1.1 Geological Setting

The 2D seismic reflection survey was completed within the northern portion of the Revell Batholith. The approximately 2.7-billion-year-old Revell Batholith is located in the western part of the Wabigoon Subprovince of the Archean Superior Province. The Batholith is roughly elliptical in shape trending northwest, is approximately 40 km in length, 15 km in width, and covers an area of approximately 455 km². Based on recent geophysical modelling, the Batholith has a relatively flat base that extends to depths of nearly 4 km in some regions (SGL, 2020). The Batholith is surrounded by supracrustal rocks of the Raleigh Lake (to the north and east) and Bending Lake (to the southwest) greenstone belts (Figure 1). For a detailed description of the regional bedrock geology, including the Revell Batholith, see Parmenter et al (2020).

Three main suites of plutonic rock are recognized in the Revell Batholith (Figure 1), including, from oldest to youngest: a Biotite Tonalite to Granodiorite suite, a Hornblende Tonalite to Granodiorite suite, and a Biotite Granite to Granodiorite suite. Plutonic rocks of the Biotite Tonalite to Granodiorite suite occur along the southwestern and northeastern margins of the Revell Batholith. The principal type of rock within this suite is a white to grey, medium-grained, variably massive to foliated or weakly gneissic, biotite tonalite to granodiorite. The Hornblende Tonalite to Granodiorite suite occurs in two irregularly shaped zones surrounding the central core of the Revell Batholith. Rocks of the Hornblende Tonalite to Granodiorite suite range compositionally from tonalite through granodiorite to granite and also include significant proportions of quartz diorite and quartz monzodiorite. Rocks of the Biotite Granite to Granodiorite suite underlie most of the northern, central and southern portions of the Revell Batholith. Rocks of this suite are typically coarse-grained, massive to weakly foliated, and white to pink in colour. The Biotite Granite to Granodiorite suite ranges compositionally from granite through granodiorite to tonalite. This suite includes the oval-shaped potassium-feldspar megacrystic granite body in the central portion of the Revell Batholith. The seismic survey was completed in rock composed of biotite granodiorite-tonalite primarily within the Biotite Granite to Granodiorite suite. In proximity to the boreholes, and the seismic survey lines, bedrock exposure is generally very good due to minimal overburden, few water bodies, and relatively recent forestry activities.

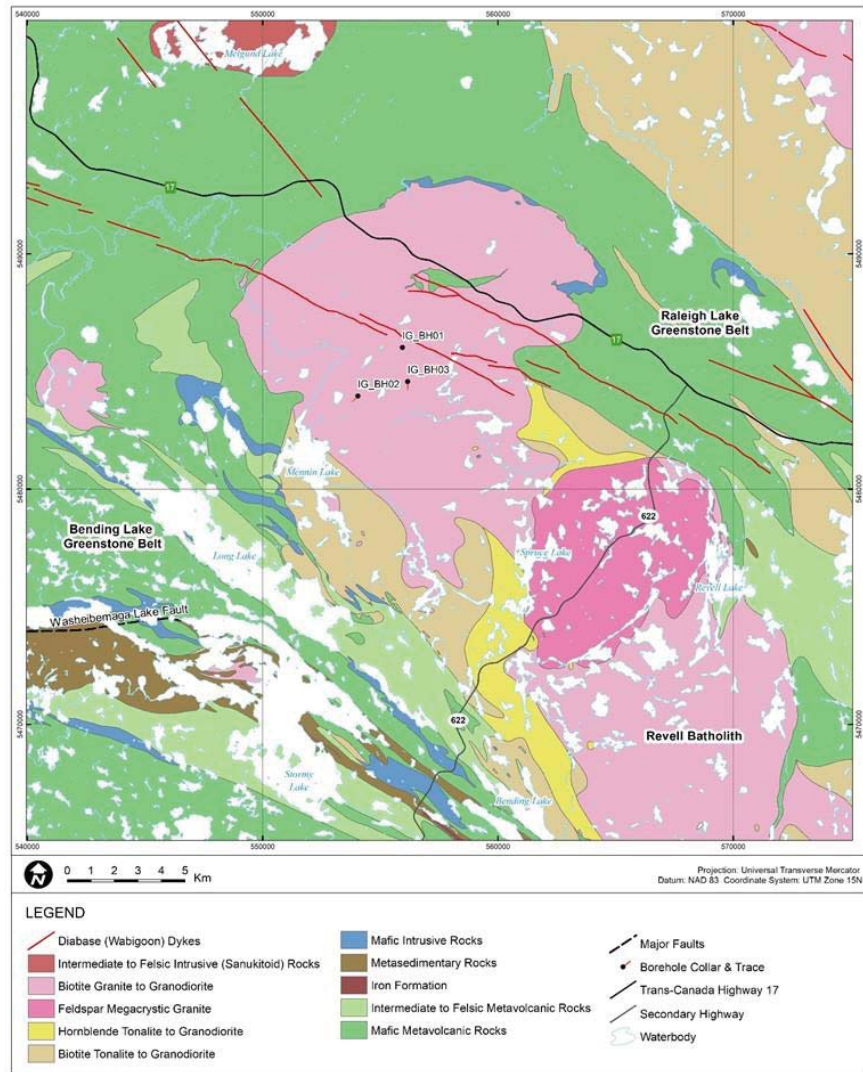


Figure 1. Geological map of the Revell Batholith and study area for the Revell Site. Data from three boreholes (IG_BH01, IG_BH02 and IG_BH03) were incorporated in this report to provide an initial assessment of the subsurface bedrock geology at the Revell Site. Drilling had completed in IG_BH04, however the results from this borehole were still preliminary at the time of this interpretation and were not used to constrain the interpretation at this time.

A west-northwest trending mafic dyke interpreted from aeromagnetic data and observed during detailed mapping to be approximately 15-20 m wide, extends across the northern portion of the Batholith (Figure 1; Golder and PGW, 2017). This dyke is associated with several other similarly-oriented mafic dykes that stretch across the northern portion of the Revell Batholith and into the surrounding greenstone belts. All of these mafic dykes have a similar character and are interpreted to be part of the Wabigoon dyke swarm. It is assumed based on surface measurements that these mafic dykes are sub-vertical (Golder and PGW, 2017).

DesRoches et al (2021) summarized the initial subsurface understanding based on the first three deep boreholes drilled onsite. The Batholith was described as an extremely homogeneous, Archean granitoid rock association composed primarily of biotite granodiorite-tonalite to biotite tonalite (representing more than 97% of the bedrock encountered in those three boreholes), accessory felsic dykes and amphibolite. Though minor by volume, the amphibolite

occurrences in all boreholes represent marker units used to subdivide the bedrock into distinct, gently dipping rock units. The average amphibolite contact orientation across the site was interpreted to be shallowly dipping, with a mean dip angle of 30° towards the north. In addition to amphibolites, a low volume of felsic dykes is also present at the site-scale.

DesRoches et al (2021) also describe a gently inclined, north-dipping to sub-horizontal structural grain in the bedrock. This structural grain is represented by a discontinuous network of sub-horizontal to gently inclined fracture zones. It is acknowledged that there may be uncertainty at this initial stage of the investigation based on the limited subsurface information available at this time. However, the sub-horizontal nature of the subsurface geological information is important for the interpretation of the 2D seismic reflection data. For additional description of the initial subsurface geology based on the first three boreholes see DesRoches et al (2021).

1.2 Supporting Geological Data

Data from three boreholes (IG_BH01, IG_BH02 and IG_BH03) were incorporated in this report to provide an initial assessment of the subsurface bedrock geology at the Revell Site. Drilling had completed in IG_BH04, however the results from this borehole were still preliminary at the time of this interpretation and were not used to guide the interpretation at this time. Approximately 1000 m of continuous HQ core was recovered from each borehole allowing for detailed logging of rock type, alteration, structure, and geotechnical properties. IG_BH01 was drilled nearly vertical with a main objective to evaluate the integrity of the bedrock away from fracture zones assumed to correspond to interpreted lineaments on the ground surface (Golder, 2018a). IG_BH02 and IG_BH03 were drilled with a planned incline of 70° towards the southwest (225°) and the south (180°), respectively (Golder, 2020d, 2020a). The inclination and azimuth of these boreholes were chosen to increase the likelihood of intersecting high-angle fractures in the subsurface that may correspond in part to such fracture zones.

Following the completion of coring and sampling, a comprehensive suite of geophysical logs was acquired over the entire length of each borehole (Golder, 2019, 2020c, 2020f). To support the interpretation of seismic reflection data, geophysical logs, particularly P- and S-wave velocity logs from full waveform sonic data, and bulk density logs were assessed and used for computing the acoustic impedance and generating synthetic seismograms (Appendix A). Synthetic logs were computed for IG_BH01 primarily because that borehole is vertical and is located directly adjacent to one of the seismic reflection lines. Upper parts of the logs measured in the borehole casing were disregarded due to the influence of the steel casing on the density values.

In addition to geophysical logs, the observed rock types and fracture frequencies along the boreholes assisted with the interpretation of reflections being able to infer any possible geological features responsible. This was particularly feasible where the seismic reflection lines were in close proximity to the boreholes. Fracture and rock type distributions within each borehole are presented in Parmenter et al (2021a, 2021b and 2021c – *in preparation*). Combined assessment of rock types and geophysical logs, together with the synthetic seismograms, suggest that the presence of amphibolite may contribute to dominant seismic reflectors in the subsurface. The amphibolites present an apparent bulk density contrast with the main host rock of approximately 0.15 to 0.2 g/cc (grams per cubic centimeter). Whenever possible, the seismic reflection data were tied into the existing deep boreholes in the area. Geophysical logs and fracture logs were used to aid the depth calibration and the interpretation of the reflectors mapped by seismic.

1.3 Objectives of the seismic survey

The general goal of the 2D seismic survey was to better characterize the upper 1500 m of subsurface, in particular, to correlate any seismic reflection data with information obtained from a set of three initial boreholes drilled between 2017 and 2020. In particular, the objectives are summarized as:

- Target and image possible sub-horizontal and dipping geological features which may manifest as seismic reflections ($<45^\circ$) through 2D seismic reflection surveying with a particular focus on depths ranging between 300 – 700 m below ground surface, and to a maximum depth of 1500 m.
- Detect, trace and characterize reflectors in the seismic data that may correspond to fracture zones, or lithological boundaries between rock units.

The 2D seismic reflection data acquisition and processing were planned to produce an optimum result, in terms of both resolution and geometrical coverage for depths ranging between 300 – 700 m below ground surface. Crooked lines were laid following existing logging roads and newly opened trails and were processed in a manner permitting also off-line reflectors, i.e. reflectors whose images are not located vertically beneath the seismic line, to be imaged. The seismic lines were extended with ~500 m at both ends of the shooting lines by planting additional geophones, so that deeper dipping reflectors could also be imaged and positioned, to a depth of 1500 m. This also helped to retain the fold coverage at the end of the lines.

Based on available data, the main geological features that could be potential targets may include sub-horizontal to moderately inclined fracture zones and amphibolites. These amphibolite features are reported to be fairly thin (with transverse dimensions in the meter range, possibly as thin as ~ 1 - 3 m, see Parmenter et al 2021a, 2021b and 2021c). If the local seismic impedance contrast between intact and altered rock is sufficiently large, features with transverse dimensions of the order of meters can be mapped with wavelengths of the order of tens of meters, as those recorded at the kilometer scale of the seismic survey. The data acquisition and processing were designed to allow the detection of such targets. However, the thickness of features with transverse dimensions of meters cannot be resolved by seismic reflection with wavelengths of tens of meters.

2 Field Activities

Vibrometric conducted the acquisition of the 2D seismic reflection data from the end of November to the middle of December 2020. The characteristics of the equipment as well as the survey design and parameters were decided upon following a modeling study performed on synthetic data, conducted prior to the field campaign.

The 2D acquisition took place from an acquisition truck placed at convenient locations with respect to the 2D lines. QA/QC procedures and calibrations were done at the beginning and end of each acquisition day. Every day, a Daily Log and a Data Quality Confirmation form were issued to and reviewed by NWMO.

2.1 Field Equipment

Vibrometric supplied the field equipment and materials necessary for completion of data acquisition. The following equipment was used to carry out the 2D seismic investigations:

- One VIBSIST-3000 seismic source (Figure 2)
- One ARIES land imaging system for the 2D seismic data acquisition with up to 300 wired active channels
- SM-24 geophones and connecting cables
- Field computer for data acquisition
- Radios for transmission of pilot trigger signal from the source to the acquisition computer
- Radios for communication between acquisition shelter and the seismic source
- Wooden stakes to mark 2D shot locations

2.1.1 Seismic source VIBSIST-3000

The seismic source chosen for the Ignace 2D survey was the VIBSIST-3000, which is a multi-impact time-distributed seismic source based on the Swept Impact Seismic Technique (SIST), described in principle by Park et al., (1996) and technically elaborated and completed by Cosma and Enescu, (2001).

The VIBSIST-3000 source uses a large-size hydraulic impact hammer, powered through a computer-controlled regulator that is mounted on an all-wheel drive/all wheel steering 7-ton tool carrier, as shown in Figure 2. The seismic source can handle topography at a reasonable speed while providing high energy and a stable source signature. The hydraulic hammer is capable of delivering 2500 - 3250 J/impact at 400-800 impacts/minute. At each shot point, the VIBSIST-3000 source was activated two times for a period of 30 seconds each, with the impact frequency being varied to generate a swept impact sequence. Each sweep contains ~200 impacts. Based on data inspection in the field, the number of sweep repetitions was sufficient to obtain high-quality seismic signal for the desired investigation depth.

The VIBSIST concept requires a pilot signal to be measured by a sensor placed on the source and this was conveyed by radio to the recording station and recorded together with the signals arriving from the receivers. The main role of the pilot signal is to record the actual time history and the energy of the impacts delivered to the ground by the source.



Figure 2. VIBSIST-3000 source being used on Line 4.

The key specifications of the equipment are given in Table 1.

Table 1. VIBSIST-3000 Specifications.

Specification	Range
Impact Energy	3000 J/impact
Energy/30s sweep	900 kJ
Peak Force	336 kN
Frequency Band	Approx. 5 to 300 Hz
Repetition Rate	Programmable between 5 and 12 impacts per second
Data Transmission	Radio/Cable link for trigger and pilot signal
Impact Hammer	Hydraulic, with gas accumulator Vertical direction, adjustable stroke
Impact Plate	Steel and aluminum Area 1m ²
Total Weight	7500 kg

The source was thoroughly tested prior to mobilization and verified every day during the data acquisition campaign. The test results were recorded in daily QA/QC documents and provided to NWMO along with the daily reports during the field work.

2.1.2 Seismic Receivers and Data recorder

A 24-bits land imaging cabled system was used for the 2D seismic data acquisition, equipped with 10 Hz geophones.

Low distortion geophones, suitable for 2-D & 3-D seismic exploration needs, having a bandwidth from 10 Hz to 240 Hz, were used for acquisition of the 2D seismic profiles in the Ignace area. An example of geophone installation in the field is shown in Figure 3.



Figure 3. Installation of the acquisition system in the field, both on the line extensions (top) and along the lines (bottom).

The entire acquisition system was tested prior to mobilization and calibration checks were performed daily during the data acquisition campaign.

In the field, the geophones were planted on the ground at specified locations (approximately 10 meters intervals) and were connected by cables between adjacent stations and from the geophone nearest to the acquisition base, to the acquisition computer. The acquisition recorder was placed at convenient locations, close to the 2D line that was being acquired. Figure 4 shows an example of field acquisition setup.



Figure 4. The acquisition recorder truck in the field and operator during acquisition.

2.2 Seismic Survey

2.2.1 Survey Design

Considering the objectives and taking into account the availability of existing pathways, it was decided to acquire 2D seismic reflection data along 5 lines. However, after initial planning it was decided to separate Line 3 into two lines due to large curvature (~ 90 degree) at the western end of the line towards IG_BH02. The two resulting lines were labeled Line 3 and Line 3-1, respectively. Therefore, six lines in total were acquired during the fieldwork, as illustrated in Figure 5.

The total planned length for all six 2D lines, at full fold, was 12624 m, i.e. approximately 13 km. Table 2 lists the planned line lengths for each of the lines. With extensions of 500 meters of geophone only spreads at both ends of each line, the total planned length to be covered with receivers was 18624 meters, i.e., approximately 19 km.

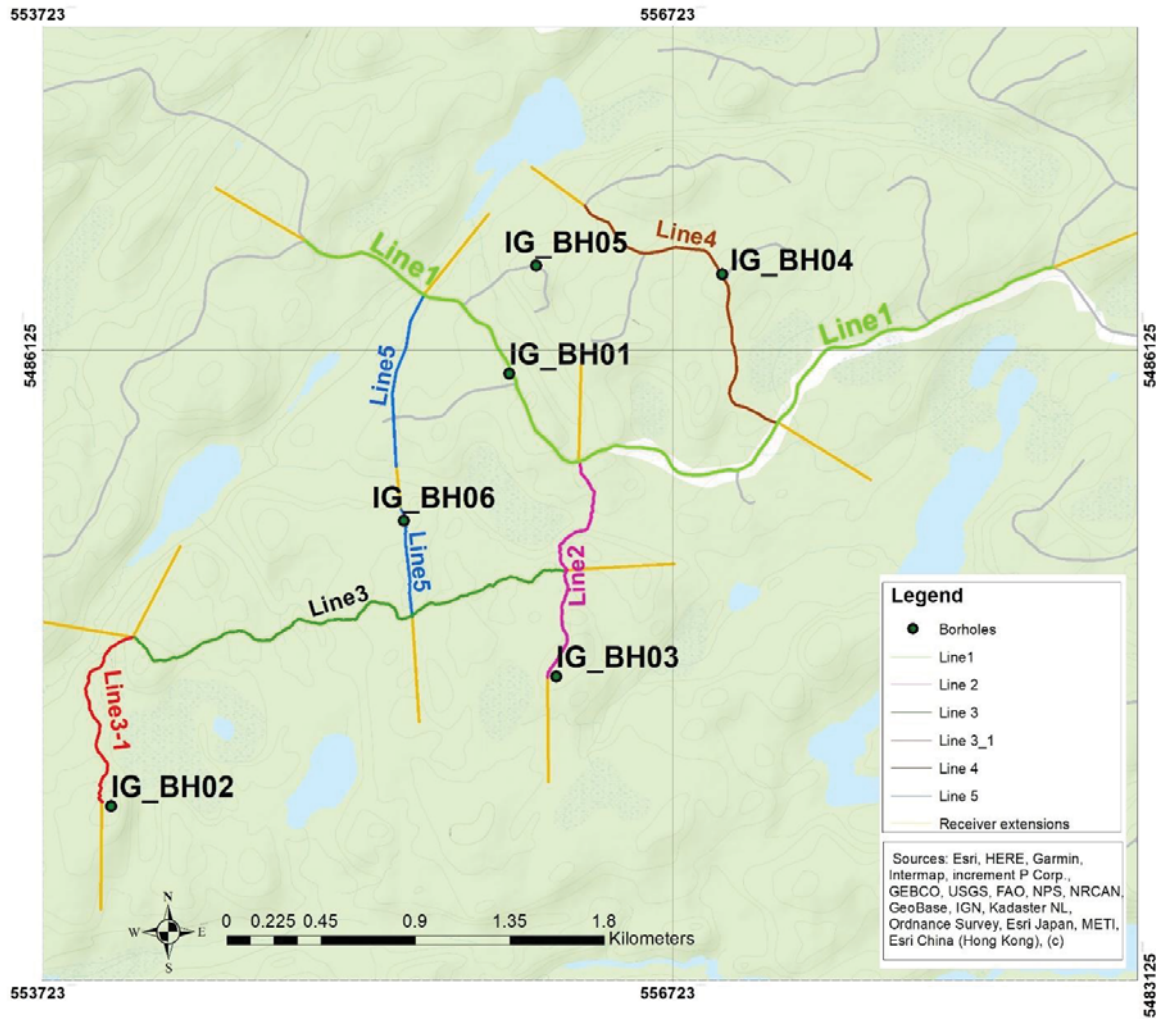


Figure 5. Map of planned seismic lines: Line 1 (green), Line 2 (magenta), Line 3 (dark green), Line 3-1 (red), Line 4 (brown) and Line 5 (blue) to be covered with both sources and receivers, while the line paddings (all shown in orange) were only covered with receivers.

Table 2- Estimated 2D seismic line lengths with extensions.

Line ID	Planned Line Length [m]	Planned number of sources	Planned Line Length with padding [m]	Planned number of receivers
Line 1	4593	231	5593	561
Line 2	1200	61	2200	221
Line 3	2381	121	3381	340
Line 3-1	980	50	1980	199
Line 4	1670	85	2670	268
Line 5	1800	72	2800	281
Total	12624	620	18624	1870

2.2.2 Survey Parameters

The receivers and cables were placed at approximately 10 m intervals along the planned 2D lines, with minor variations, determined by local conditions. When possible, the geophones were placed in the ground in order to achieve maximum data quality, while decreasing unwanted noise. A minimum of 200 channels were active at all times, meaning that at least 2 km of 2D data was acquired for each shot location. In fact, most of the records were made on 300 active channels (3 km long profiles), except for Line 3.1, which entirely consisted of 195 receivers, being only 1.95 km long. An approximately 500 m extension, at each end of each line (padding) was covered only with receivers, in order to maintain the fold of the acquired data for the length of the 2D line. The VIBSIST-3000 source was placed along each of the 2D profiles at an average distance of 20 m between shot points. Radio communication was used between the recorder truck and the source, to confirm its current location and coordinate at the start of each recording. All source locations were marked and labeled beforehand, and accurate GPS coordinates were measured just after the acquisition of each 2D line, while marks of the impact plate on the ground were still visible and stick marks were still present. The geometry of the measured 2D seismic reflection lines is shown in Figure 6, while the field survey parameters are as shown in Table 3.

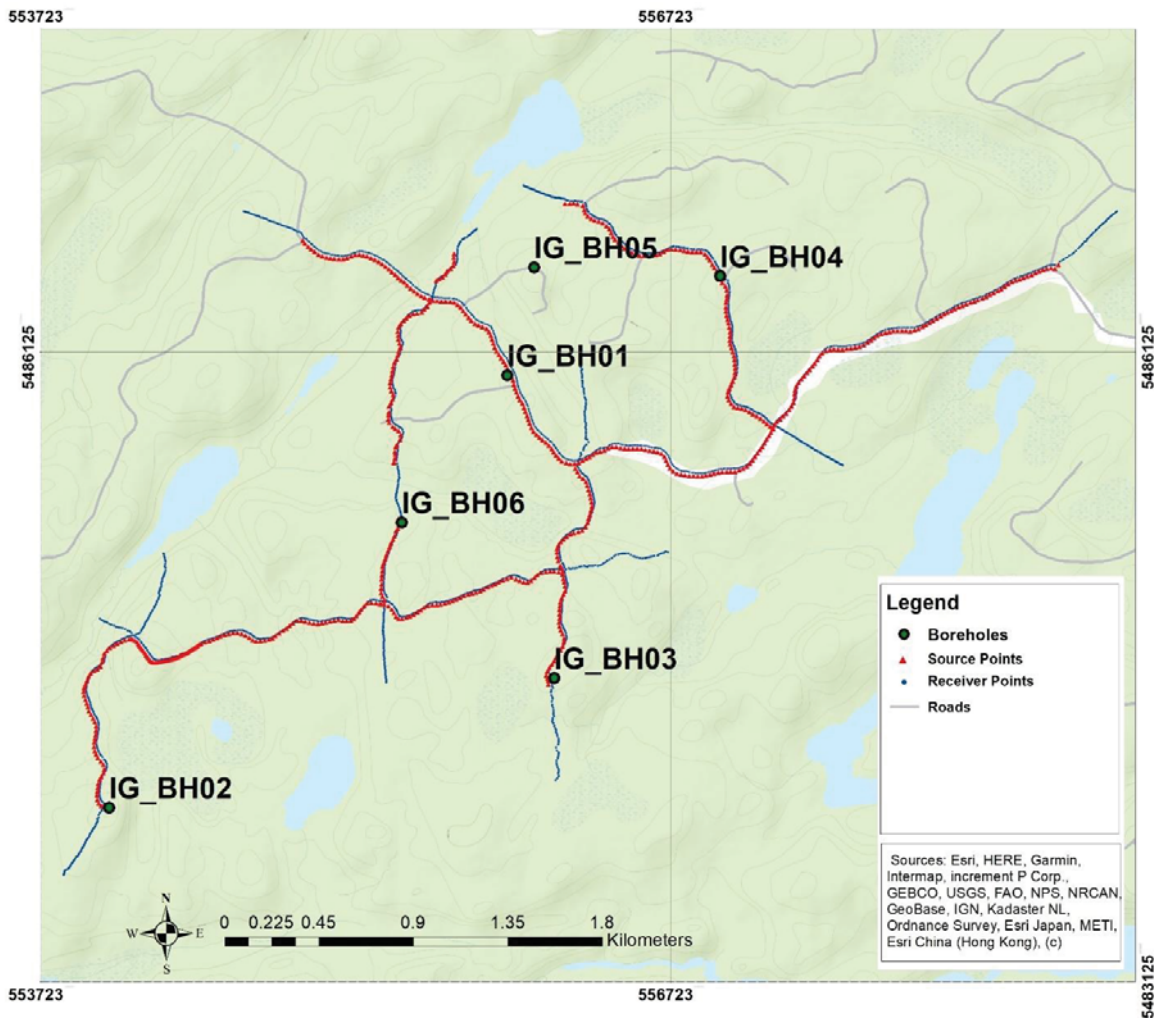


Figure 6. Map of the measured seismic lines, similar to the one shown in Figure 5. Sources are shown in red and receivers are shown in blue. Line extensions were only covered with receivers.

Table 3- Measured lengths of the 2D seismic lines, with extensions.

Line ID	Measured Source Length (m)	Spacing (min / max) (m)	Number of sources	Measured Receiver Length (m)	Spacing (min / max) (m)	Number of receivers
Line 1	4621	20 (16.5 / 23.4)	231	5329	10 (4.2 / 15.2)	560
Line 2	1197	20 (12.5 / 30.6)	61	2239	10 (6 / 17)	214
Line 3	2316	20 (16 / 24) 10 (8.5 / 13)	136	3040	10 (6.7 / 16.4)	295
Line 3-1	953	20 (10.3 / 23.6))	50	1825	10 (4.5 / 15)	195
Line 4	1791	20 (17.3 / 25.7)	90	2396	10 (3.3 / 15.9)	268
Line 5	1870	20 (5 / 28)	81	2446	10 (4.2 / 14.9)	264
Total	12748		649	17275		1796

3 2D Data Processing

The surface reflection data at Ignace were acquired along 2D crooked lines. A practical reason for this choice was the access limited to authorized roads and trails. When the survey geometry is significantly irregular and the geologic structures have cross-profile dips, as expected with seismic surveys performed in hardrock settings, several standard 2D imaging procedures severely under-perform (Nedimovic, 2003a). In such cases, reflection processing needs to take into consideration the real geometry and preferably use 3D stacking and migration routines. As illustrated in Section 3.8, Figure 28, migrations can be performed for different ‘off-plane’ dips i.e., for various rotational angles around the datum line of the profile. In a migrated section generated from crooked line data, the ‘apparent depth’ varies with the ‘off-plane’ angle. Although line-crookedness does not produce equivalent data with a full 3D setup, it can be useful with the positioning in 3D of reflectors interpreted in adjacent profiles, as shown in Section 4.1.

The static corrections used for the processing of the 2D data from the Ignace area were derived by 3D tomographic inversion (Cosma, 2017) and the migration approach was based on a 3D pre-stack migration algorithm (Cosma et. al. 2010, Enescu et. al. 2003, and Enescu et. al. 2004). The overall processing sequence is as described in Table 4.

Table 4. Processing sequence for the crooked 2D lines.

Item	Description
1	Decode the VIBSIST impact sequences
2	Apply geometry, with particular attention to handling crooked line geometry
3	Arrival time picking
4	First stage refraction statics
5	Velocity analysis, 3D tomographic inversions for determination of P-wave velocity fields in the near surface
6	Static corrections
7	Band-pass filtering and spectral shaping (equalization, blueing) 20 – 160 Hz
8	Separation of direct arrivals and reflected wave fields
9	Amplitude equalization, trace balance
10	Image Point filtering and reflector enhancement in the image space (*)
11	3D Kirchhoff migration & 3D CMP Radon migration

(*) Image Point Filtering was used to aid target recognition in the shot gathers but not used further in the processing sequence.

3.1 Decoding the VIBSIST impact sequences

The description of the Swept Impact Seismic Technique (SIST) used by the VIBSIST-3000 source is given in detail in (Cosma and Enescu, 2001b) and an example of a long, coded record is shown in Figure 7. The coding function used has been a monotonically decreasing impact time sequence from 300 ms to 150 ms over 30 seconds. The resulting decoded record is illustrated in Figure 8.

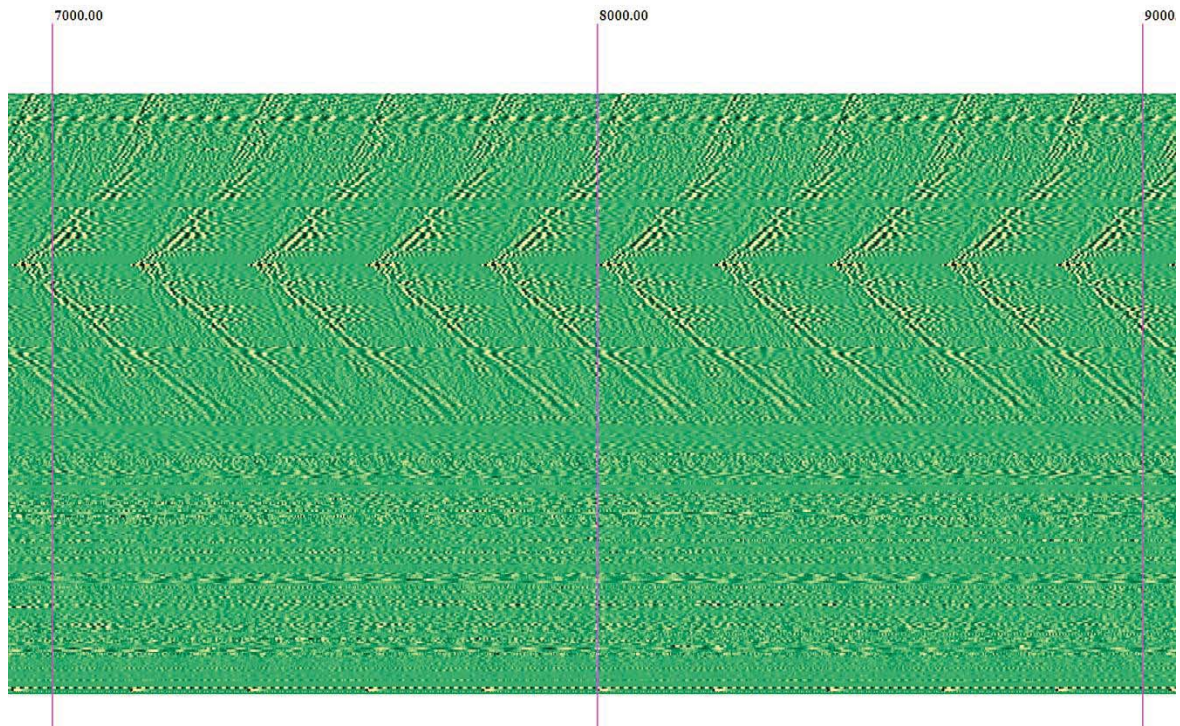


Figure 7. Example of a section of a coded impact sequence from a field record. Axes are Time (ms) and Length (m) (same as in Figure 8).

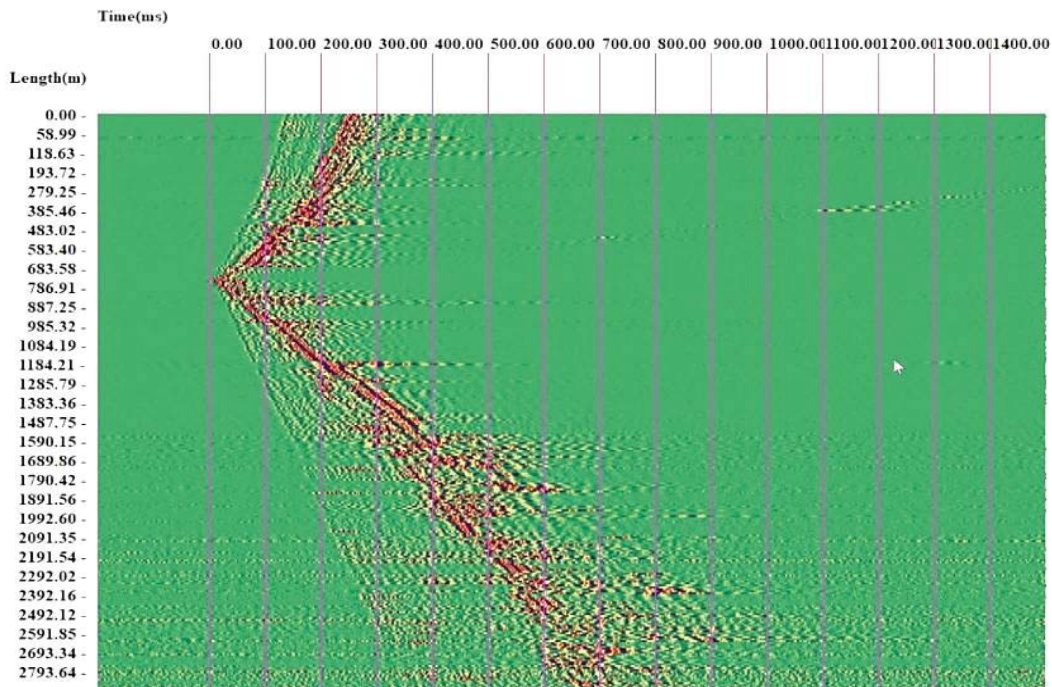


Figure 8. Decoded impact sequence, raw data profile recorded from one source location (source 20, Line1).

After decoding the records show relatively low amplitude ambient noise before the first arrivals, which is considered as a mark of good data quality. The source generated signal following the first onsets appears to be quite complex, containing recognizable refracted, diffracted and P-converted S-waves.

3.2 Preconditioning of the data profiles

During this processing stage, the following operations were completed:

- The geometry information was incorporated into the data profiles.
- The main frequency band of the P-waves was estimated to be 20 – 160 Hz (as illustrated in Figure 9 and Figure 10), hence a zero-phase band-pass filter was used for filtering all data profiles in this frequency band.
- The signal levels were adjusted so that the average amplitudes of different traces and different parts of the same trace become comparable.

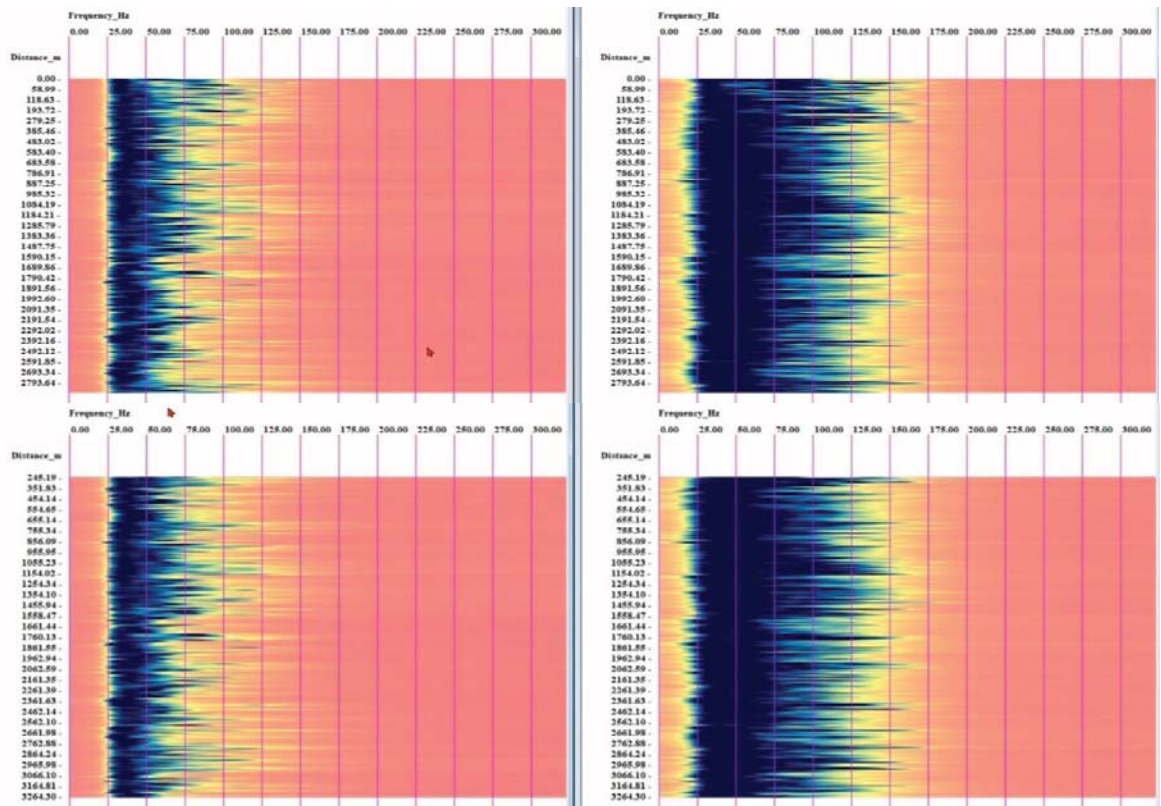


Figure 9. Line 1: average spectra (left) and average spectra in a window before the ground-roll arrival (right) at two different locations along the line.

Shot locations with better coupling of overburden to hardrock display higher frequencies than shot locations with poorer coupling of the overburden to the bedrock, where lower frequencies could be recorded. This is illustrated in Figure 10, where the average frequency spectra at two adjacent receiver locations is displayed, one receiver (#251) having better coupling to the ground, hence wider spectral frequency content, than the neighboring receiver (#250).

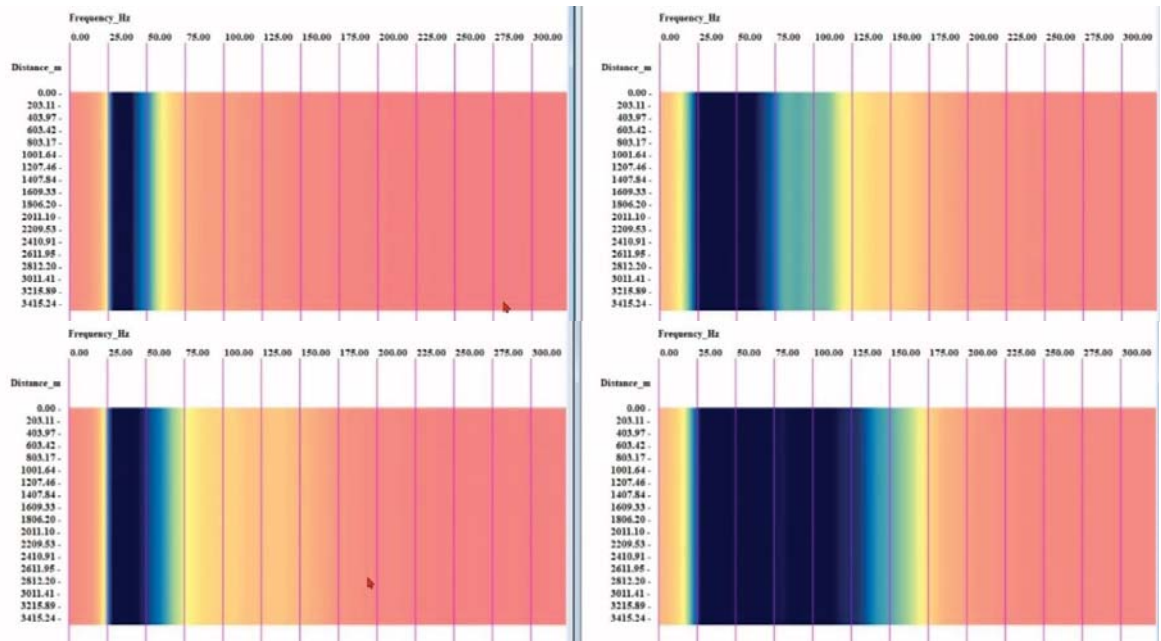


Figure 10. Line 1: average spectra (left) and average spectra in a window before ground-roll (right) at two adjacent receiver locations along the line, receiver 250 is shown on top and receiver 251 is shown in the bottom.

Several band pass filter trials were conducted, in the following bands 20 – 160 Hz, 40 – 160 Hz, 60 – 160 Hz, 80 – 160 Hz and 20 – 50 Hz, 20 – 100 Hz, 20 – 150 Hz. The retained frequency band of the P-waves was 20 – 160 Hz, although the lower part of the spectrum also contained significant energy from ground-roll and S-waves, refracted as well as coherently scattered and converted wave fields. Filtering in this band was done prior to first P-wave arrival time picking. Figure 11 shows the comparison of a receiver gather filtered in two frequency bands 20 – 50 Hz and 20 – 160 Hz.

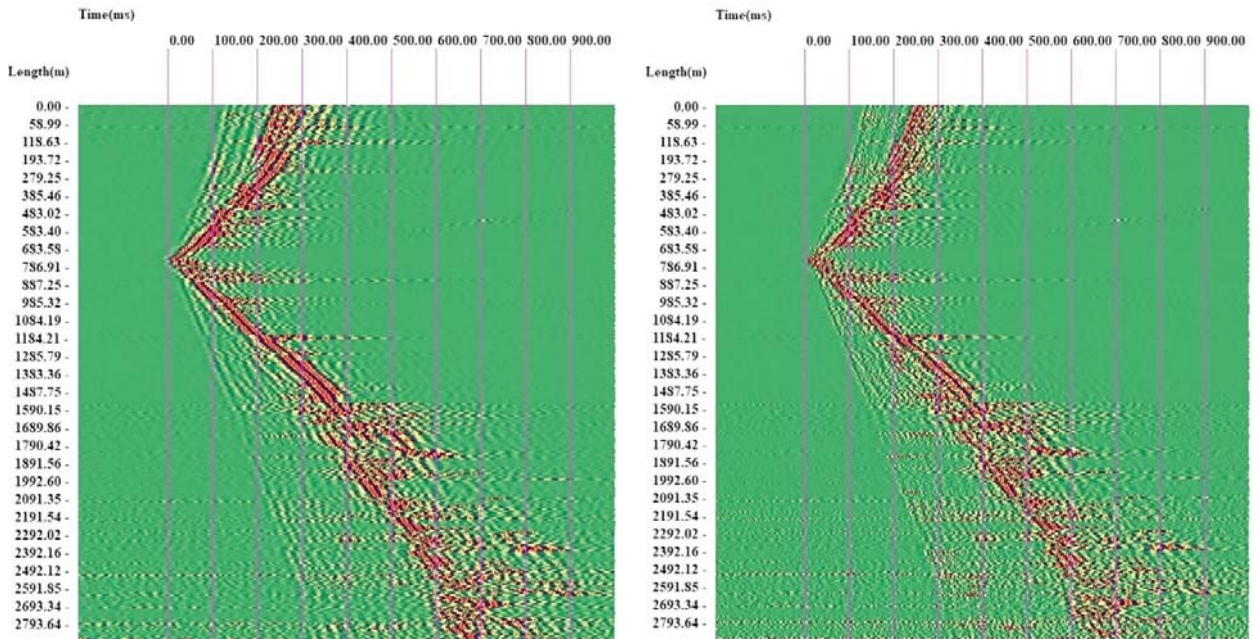


Figure 11. Same as in Figure 8, band pass filtered in the 20 – 50 Hz (left) and in the 20 – 160 Hz (right) frequency band.

3.3 Arrival time picking and First stage refraction statics

P wave first arrival times were picked accurately and without problems on most of the traces and an example of picked arrival times for a receiver gather for one source on Line 1 is shown in Figure 12 and Figure 13.

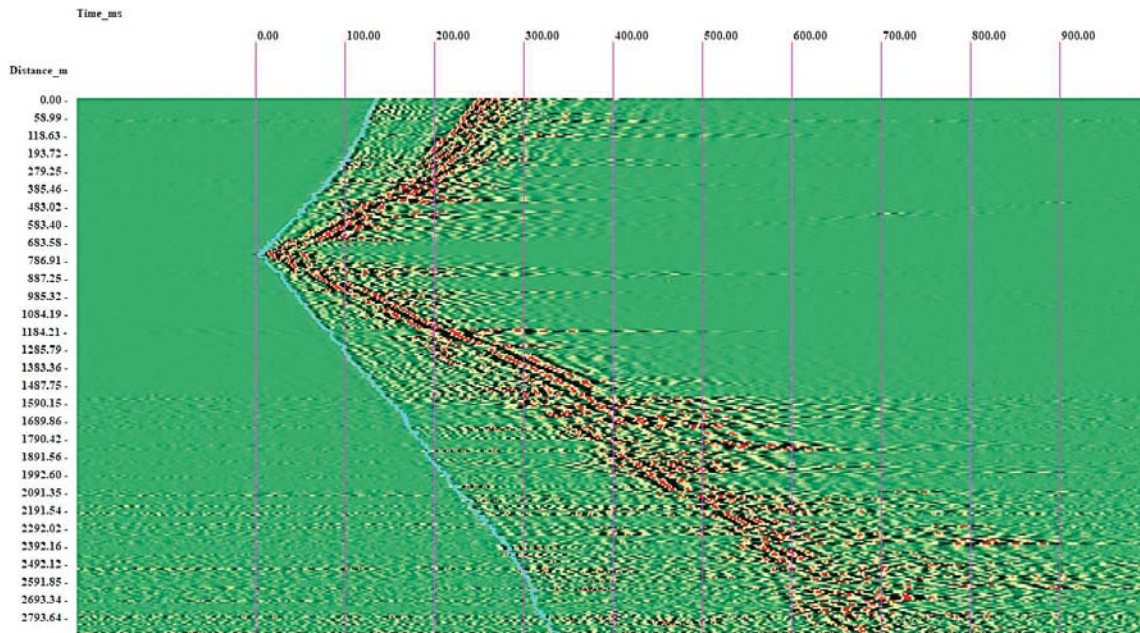


Figure 12. Picked arrival times (cyan) for a receiver gather for source 20 on Line 1.

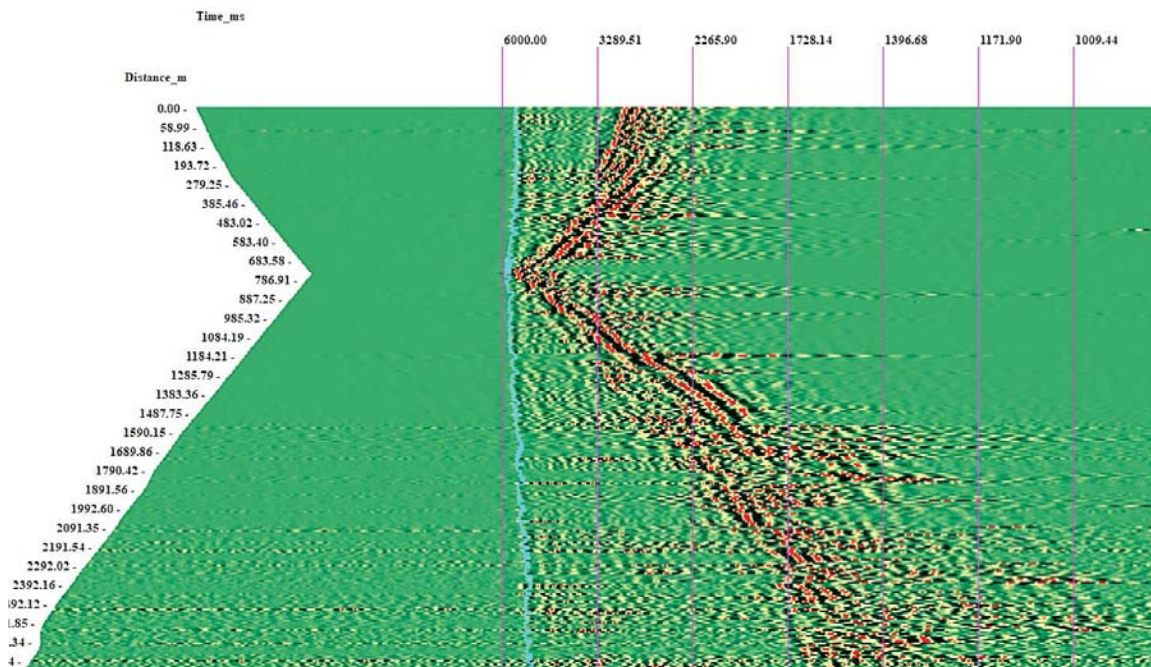


Figure 13. Same as in Figure 12, with a reduced velocity display, with $V = 6000$ m/s.

One can observe in Figure 13 a slow variation of the arrival times along the line, hence of the apparent velocity, due to refraction through and beneath a near surface lower velocity zone, as well as a trace-to-trace clutter due to varying conditions adjacent to each receiver location, which may be observed easier in Figure 14. The local clutter of the picked first arrival times was removed by first stage static corrections. An example of such corrected receiver gather is shown in Figure 15.

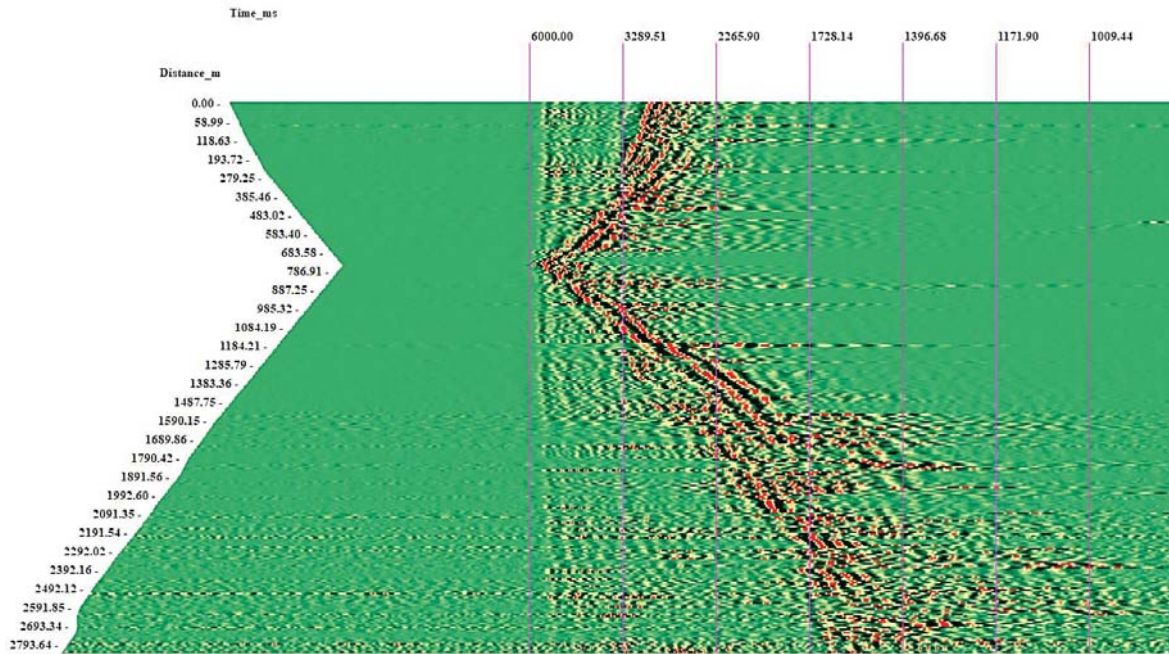


Figure 14. Same as in Figure 13, without the display of picked first arrival times.

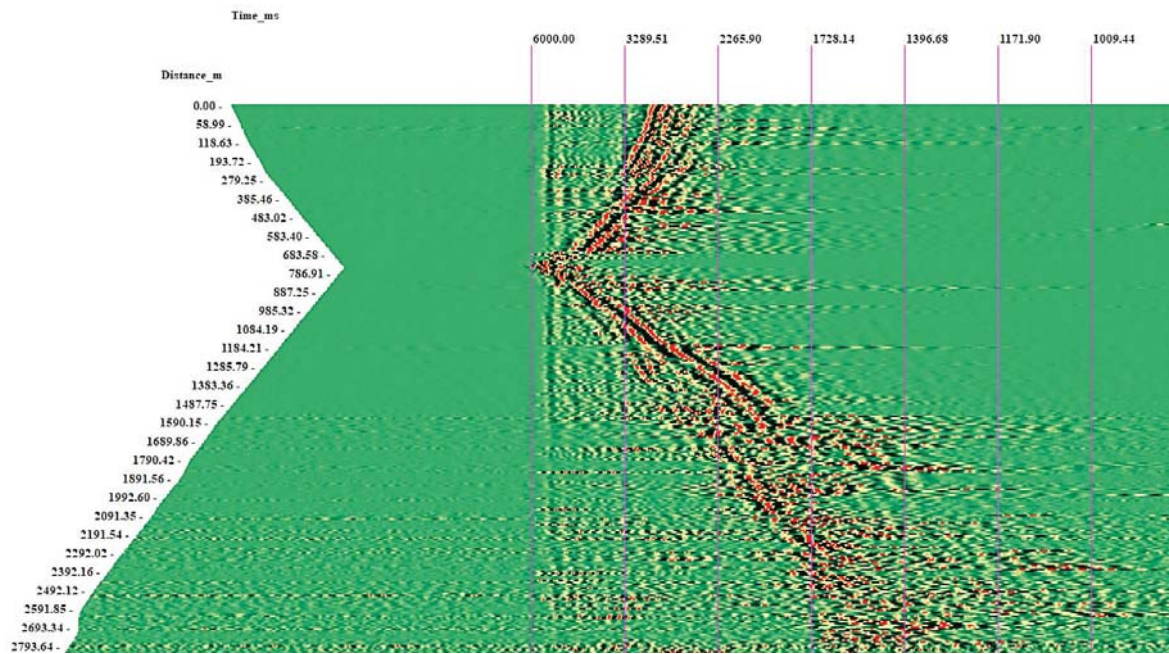


Figure 15. Same as in Figure 14, after applying first stage static corrections.

3.4 Velocity analysis, 3D tomographic inversions for P wave velocity in the near surface

Seismic tomographic inversion was used to derive spatial distributions of the seismic velocities in the near surface from the travel times measured on the crooked 2D lines. Linear best fit approximations were used for each of the crooked lines, except for Line 1 (the longest), where two attempts were made, a first one using a one line approximation and a second by splitting the line and using a two lines approximation (Line 1.1 and Line 1.2), as illustrated in Figure 16. Segmenting Line 1 into two parts appears to be the better option, as processing the whole Line 1 produces too large lateral offsets of the source-receiver refracted ray paths. As the travel times, paths, inversion block parameterization and residuals are computed in 3D, a too wide lateral spread can lead to poor coverage (low fold) of the inversion blocks and therefore larger inversion artifacts.

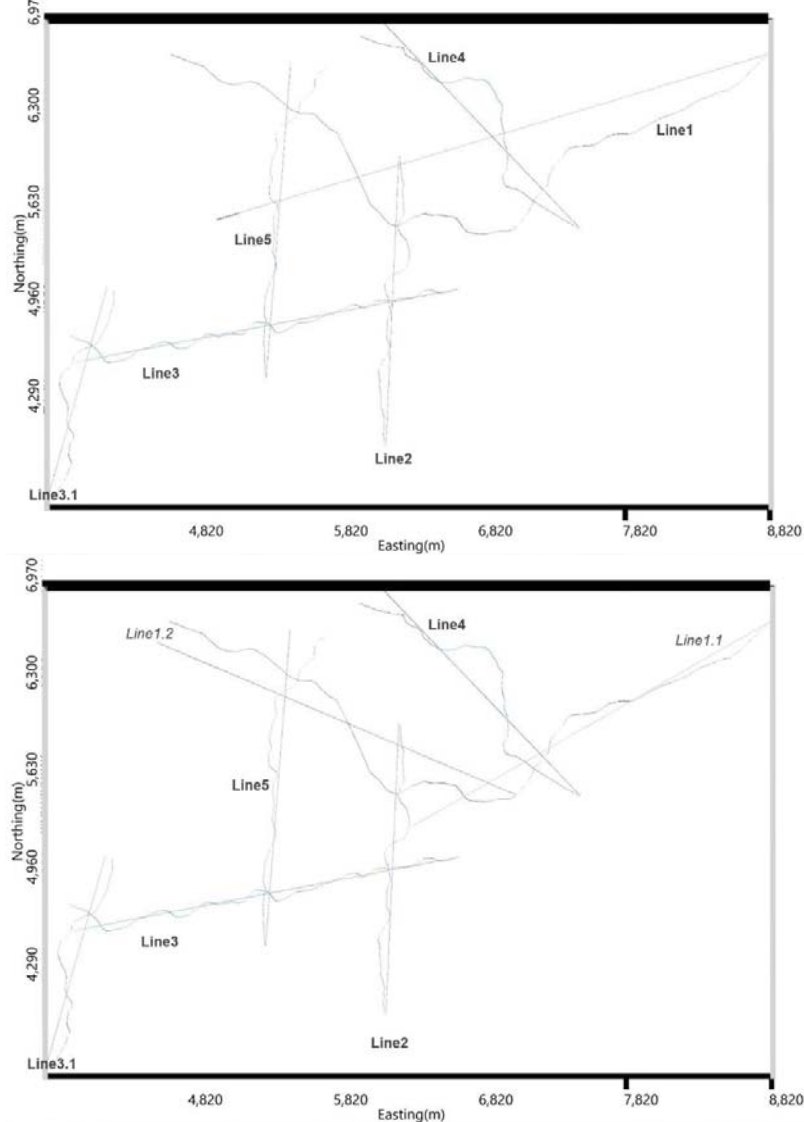


Figure 16. View from top of the 2D lines and their best fit planar approximations (shown as straight lines), with two options for Line 1 (top: entire line was fitted; bottom: this line was split into two, overlapping sections: Line1.1 and Line1.2), which is the longest and most crooked. Easting and Northing labels show reduced coordinates (after removal of least significant digits: 5480000 was subtracted on Northing and 550000 was subtracted on Easting).

Figure 17 displays the near-surface velocity field representations derived from P-wave first arrivals by tomographic inversion projected along the best fit lines. The velocity scale is the same for all lines, from 3100 (red) to 6100 (blue) m/s. The transition from the low-velocity near-surface zone to competent bedrock lies at approximately 75m depth or above along all lines.

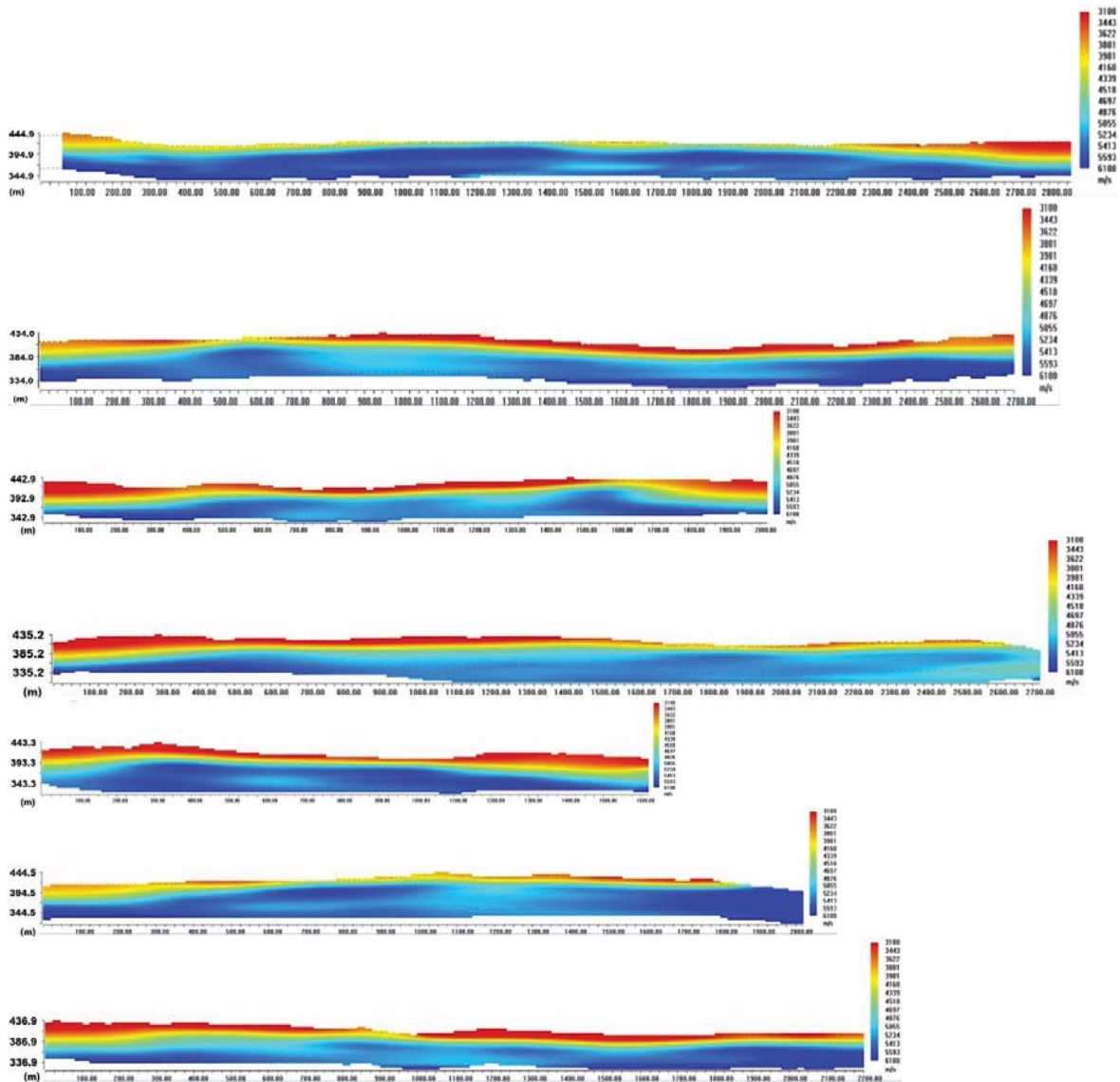


Figure 17. P wave velocity in the near surface along the 2D lines, from top to bottom: Line 1.1, Line 1.2, Line 2, Line 3, Line 3.1, Line 4 and Line 5. The velocity scale is the same for all lines, from 3100 m/s (red) to 6100 m/s (blue).

The 3D near-surface velocity field reconstructed by tomographic inversion is shown in Figure 18.

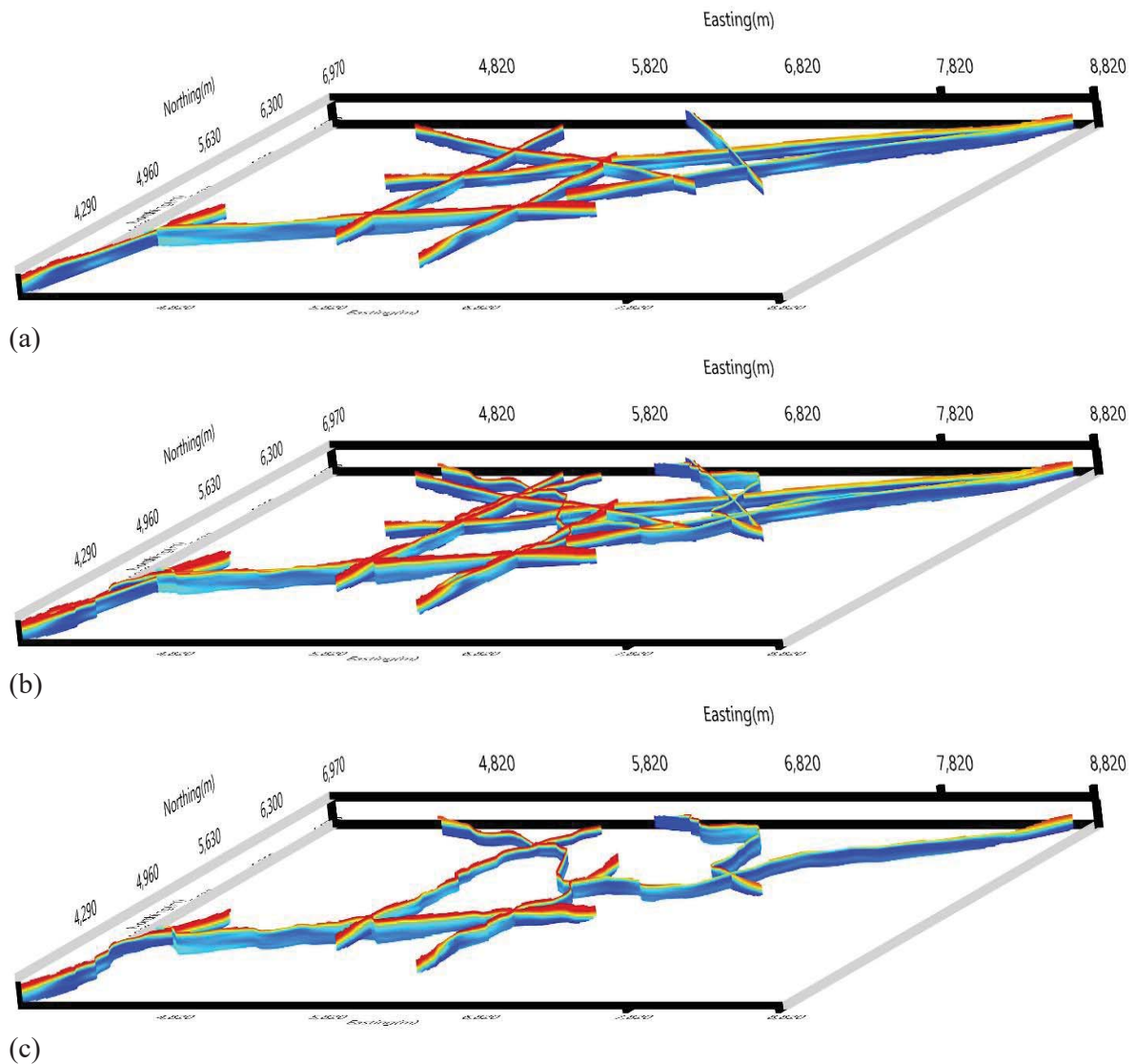


Figure 18. 3D view of the near surface P wave velocity derived on: (a) best fit linearly approximated crooked lines, (b) linear best-fit line approximations and 3D crooked line representations, and (c) velocity reconstruction along crooked lines. Easting and Northing show reduced coordinates (after removal of least significant digits) and the color scale is the same as in Figure 17, from 3100 m/s (red) to 6100 m/s (blue).

3.5 Static corrections

Travel times computed on the tomographic velocity distributions were compared with the picked times, after removing the local residuals, as shown in Figure 15. Time differences between the picked times and tomographic travel times were used as static corrections. The corrections were applied using arrival times computed on the 3D velocity field obtained by 3D tomographic inversion from all data sets (all seven crooked 2D lines, as Line 1 has been processed as two separate lines, Line 1.1 and Line 1.2). The correction was applied for $V_p = 5750$ m/s and datum of -75 m below the surface. The velocity and depth values were evaluated from the tomographic charts. The bedrock appears to be above 75 m depth at all locations along the measured 2D lines and 5750 m/s appears indeed to be a representative value for the bedrock at that depth.

An example of a receiver gather before and after static corrections is shown in Figure 19 and the verification of the travel times computed on the P wave velocity distributions derived by tomographic inversion is shown in Figure 20.

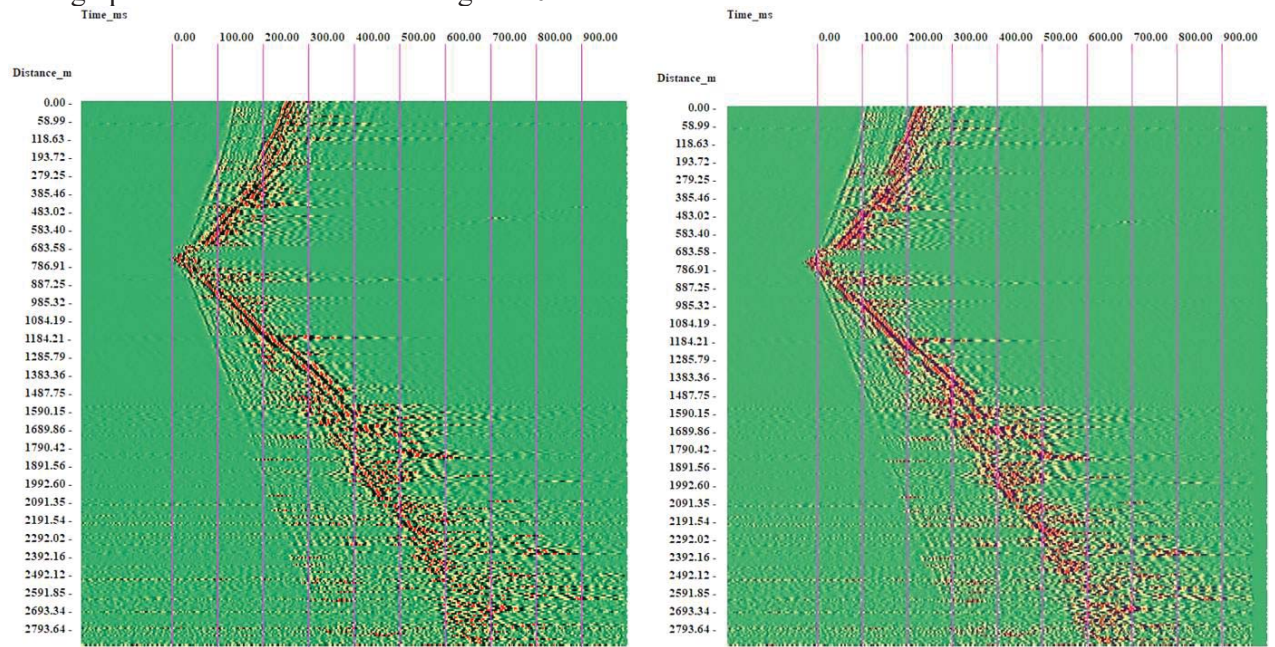


Figure 19. Receiver gather for source 20 on Line 1, before (left) and after (right) static corrections were applied and datum set at -75m below surface.

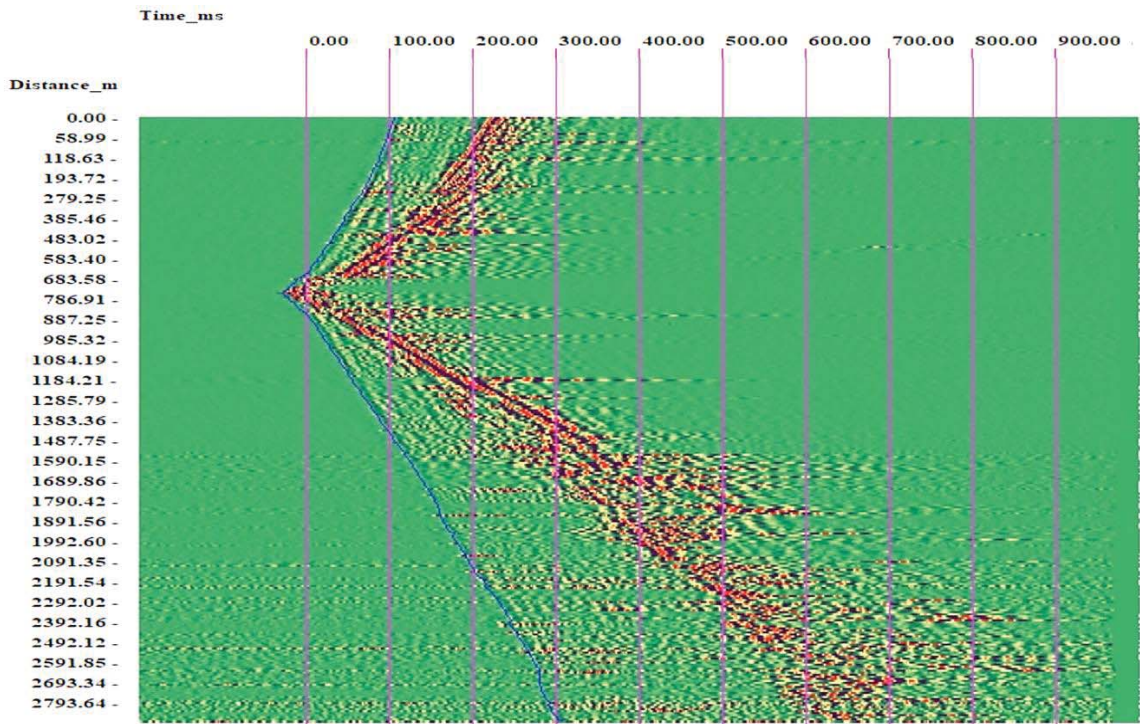


Figure 20. Receiver gather for source 20 on Line 1, after static corrections were applied and with arrival times computed on the P wave velocity field derived by tomographic inversion (shown in Figure 17) and with the datum set at -75m below surface.

3.6 Conditioning of the data profiles

After applying static corrections, the datum was set at -75m below surface at each point, i.e., the datum copies the actual topography 75m below. This approach was used instead of the more usual fixed elevation datum, as the transition from the low velocity near-surface zone to the high-velocity characteristic for the bedrock follows a similar pattern.

3.6.1 Removal of direct wave fields

The processing flow continued with the removal of the direct wave fields. The ground-roll and the S-wave and P-wave first onsets, as well as the P-S conversions which could be identified as such, were suppressed by means of variable slope median filters, with an initial prediction for the slope being given by a best estimate of first arrival times. Statistical estimators of the wavelet were used to refine the slope prediction and update the travel times. Exact input arrival times are therefore not needed, which considerably helps especially with suppressing ground-roll, which varies significantly both in velocity and wavelet character.

The processing steps used at this stage are described in Table 5 and illustrated in Figure 21 to Figure 23.

Table 5. Processing sequence for removal of direct waves arrivals.

AGC	window 100 samples (100 ms)
Variable slope median - both on shot and receiver gathers	slope: best fit along estimated S-wave arrivals (2500m/s - 3400 m/s) in a running panel of 21 traces in a window of 25 samples; alpha-trim - 0.5 (0=average, 1=median)
Variable slope median - both on shot and receiver gathers	slope: best fit along estimated surface-wave arrivals (1700m/s - 2400 m/s) in a running panel of 21traces in a window of 25 samples; alpha-trim - 0.5 (0=average, 1=median)
Variable slope median - both on shot and receiver gathers	slope: along P-wave arrivals after statics panel (traces) – 21 window (samples) – 25 alpha-trim - 0 (0=average, 1=median)
Band-pass filter	0-phase Butterworth Order of filter – 4 Low frequency limit (Hz) – 20 High frequency limit (Hz) – 160
Inverse AGC	window 100 samples (100 ms)
AGC	window 400 samples (400 ms)

Typical results after processing all data lines as described above are illustrated in Figure 22 and Figure 23.

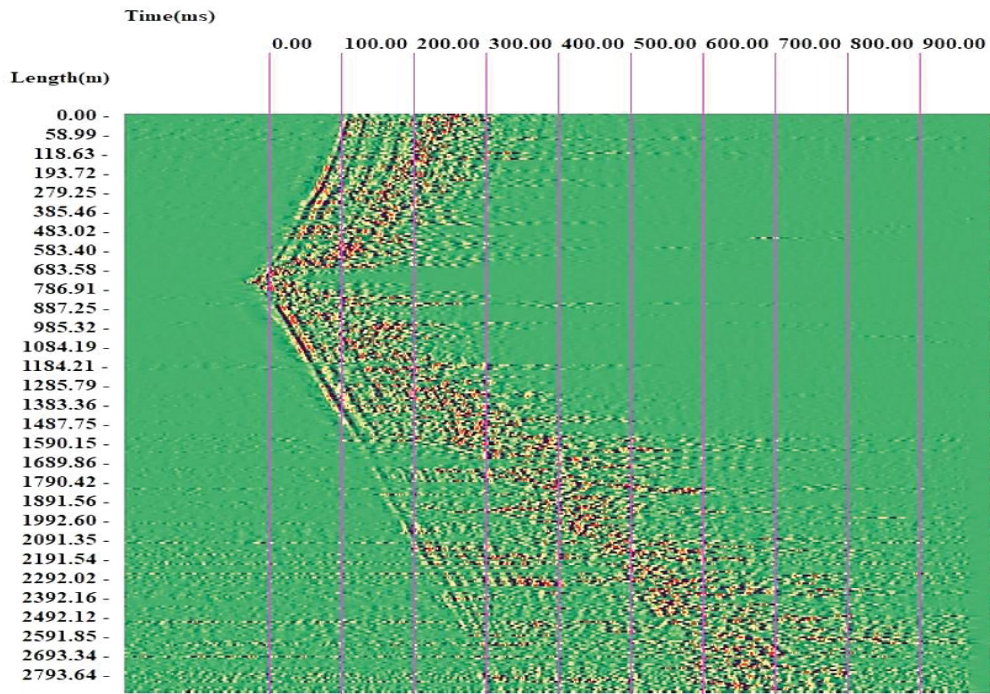


Figure 21. Receiver gather for source 20 on Line 1, after removal of shear (V_s 2900 – 3400 m/s) and surface wave fields (V_{surf} 1900 – 2300 m/s).

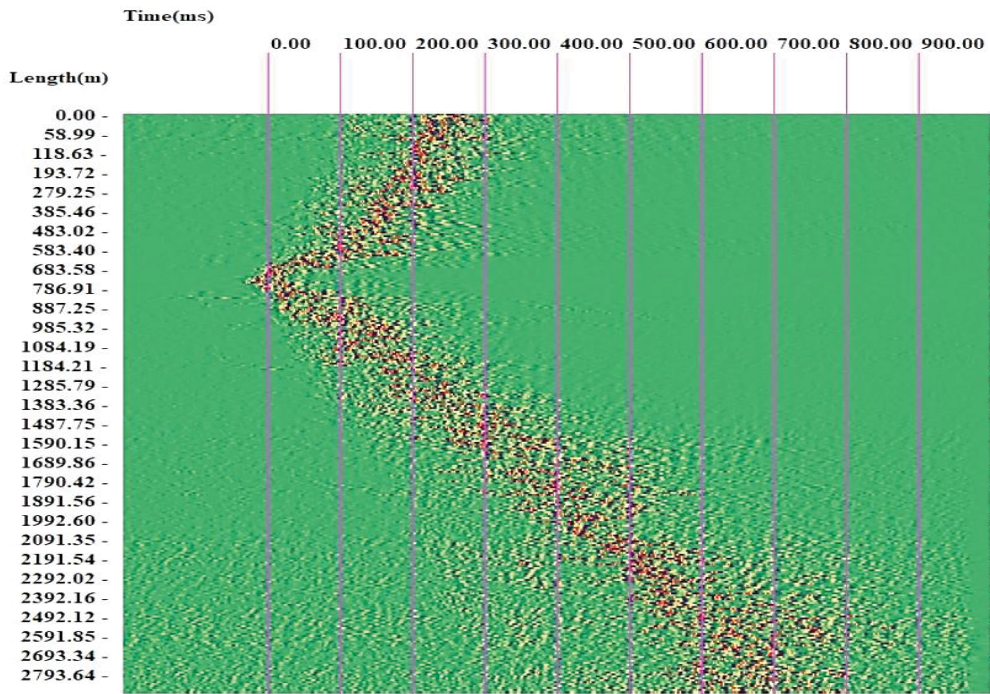


Figure 22. Same as in Figure 21, after removal of compression wave field.

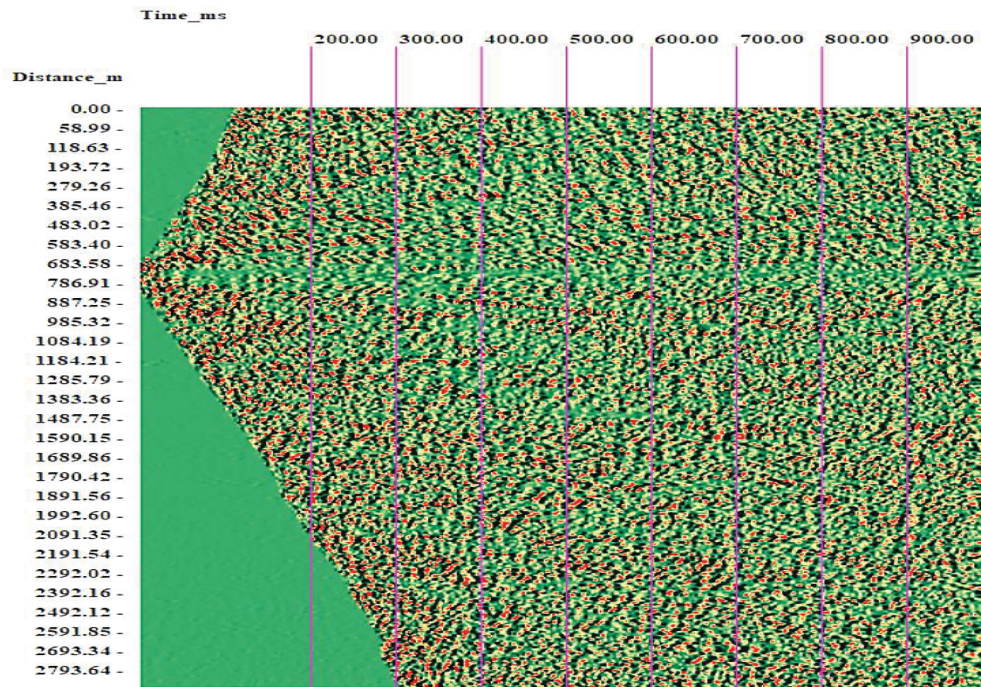


Figure 23. Same as in Figure 22, after amplitude equalization & trace balancing.

3.6.2 Image Point filtering and reflector enhancement

Reflector enhancement by non-linear filtering using a model driven Radon transform technique (Image Point filtering, defined by Cosma and Heikkinen, 1996) has been attempted. An example is shown in Figure 24. This procedure increases visibly the continuity and coherence of certain patterns representing potential seismic reflectors. However, this type of filtering was not retained at this stage in the main processing flow, as non-linear interventions introduced in the processing flow in between fully linear operations can actually increase the uncertainty instead of decreasing it.

Therefore, the 2D data were minimally processed, as described above, before proceeding to 3D pre-stack depth migration. The input to depth migration consisted of profile versions like the one shown in Figure 23. Non-linear reflector enhancement, including Image Point filtering, were postponed towards the end of the processing, to be applied if and when needed.

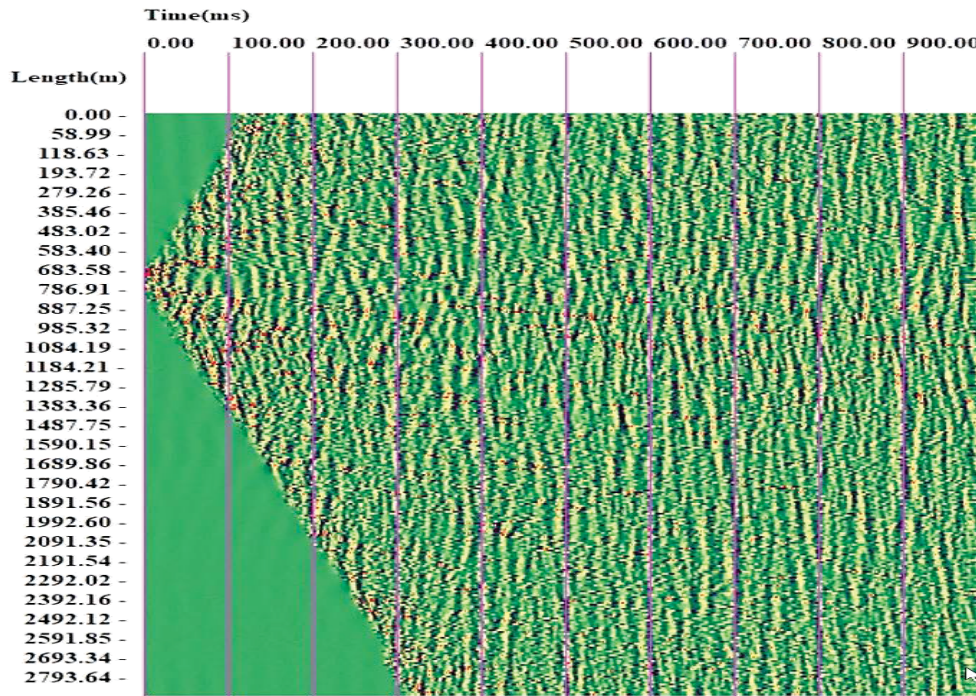


Figure 24. Same as in Figure 22, after amplitude equalization and Image Point filtering.

3.7 Migrated profiles positioning and datum

2D migration best fit lines were used in a similar manner as with the tomographic inversions, that were described in Section 3.4. As with tomography, these lines were used only as projection axes, the migration paths and reflection points being computed in 3D (the reflection points are an extension of the midpoint concept used in conventional 2D migration). The location of these lines is illustrated in Figure 16 (bottom) of Section 3.4.

Following the conclusions listed in Section 3.4, the processing lines were lowered by 75 m below their calculated positions on surface. To maintain the consistency of possible off-line reflectors, as shown in Section 3.8, Figure 28, the coordinates for each line were calculated independently and then lowered by 75m below the local surface. The static corrections described in Section 3.5 were applied for this datum. The midlines used for the 3D migrations are therefore not all at the same elevation nor necessarily horizontal, since these were computed as best fit lines over the true topography. The processing line elevations are listed in Table 6.

Table 6. Processing line elevations for the midlines of the migrated 2D profiles.

Processing line elevations	Min (m)	Max (m)	Average (m)	Deviation from horizontal average (m)	Depth sampling interval (m)
Line 1	343.79	346.75	345.25	+ / - 1.48	5
Line 1.1	347.04	347.18	347.1	+ / - 0.07	5
Line 1.2	341.35	345.18	343.25	+ / - 1.91	5
Line 2	346.74	359.76	353.25	+ / - 6.51	5
Line 3	343.01	350.62	346.81	+ / - 7.61	5
Line 3.1	329.92	348.05	338.98	+ / - 9.06	5
Line 4	354.61	359.58	357.09	+ / - 2.48	5
Line 5	327.27	351.56	339.41	+ / - 12.15	5

3.8 3D Kirchhoff migration & 3D CMP Radon migration

Both 3D Kirchhoff and 3D CMP Radon depth migrations were computed for all lines. The quality of the 3D Kirchhoff migration was found to be poorer than the one of its 3D CMP Radon counterpart, both in terms of noise and of recognizable coherence of events likely to be associated with P-wave seismic reflectors. A relevant example is shown by the comparison of the migrated profiles for Line 1.2, shown in Figure 25 and Figure 26. However, the Kirchhoff and 3D CMP Radon profile versions describe the same reality and the former, albeit noisier, can be consulted, e.g. for confirming local details where the interpretation of the latter leaves room for doubt.

The pre-stack data used to calculate the 3D migrations was not affected by time errors, as the time picking had been thoroughly verified, as noted in Section 3.3. Likewise, the derivation of the refraction statics by 3D tomography, as described in Section 3.4, was checked for errors (see Section 3.5) and none of these processing steps are likely to influence the quality or introduce a bias in the migrated profiles.

The name NMOPT migration previously used (Enescu et. al. 2003 and Enescu et. al. 2004) is rather restrictive and can be misleading, as it directly relates to the Normal Move Out and P-Tau computation methods, of which none is rigorously applicable in this 3D geometry. A more accurate description for the migration algorithm used here is as a CMP-Radon method, as named here (a detailed description is given in Appendix B). Indeed, Move Out corrections are not “Normal” in a crooked line case where the midpoints must be computed for each dip and azimuth in the selected range of possible reflectors. Likewise, although the stacking technique used bears computational similarities to the P-Tau transform, the procedure can be more generally termed as a model driven Radon transform.

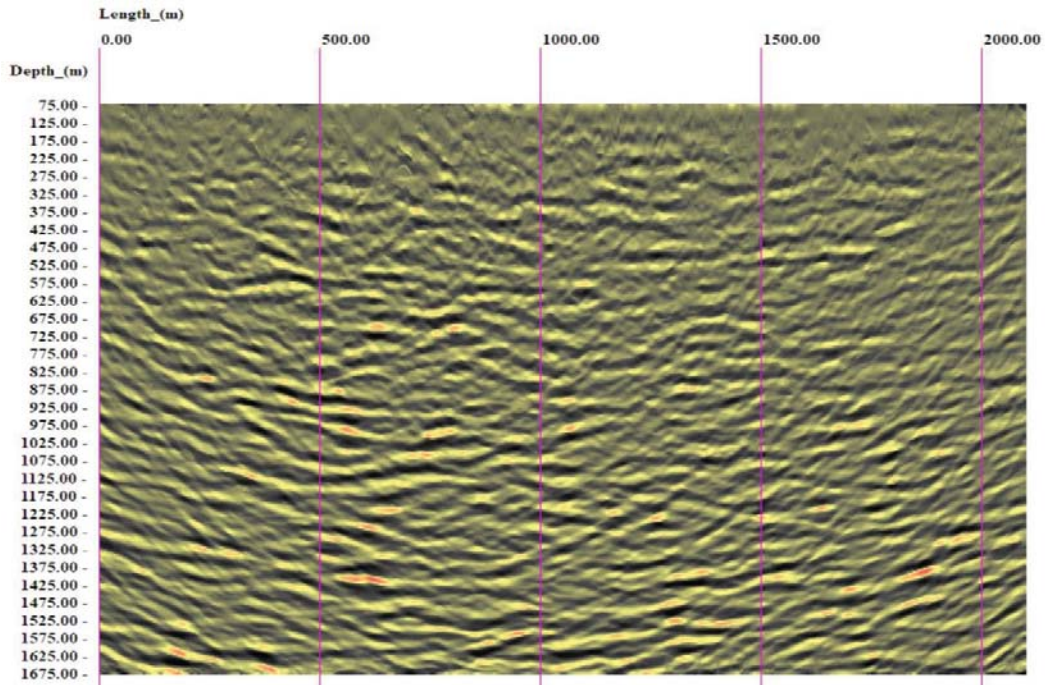


Figure 25. Line 1.2, Kirchhoff migration (with amplitude equalization & trace balancing).

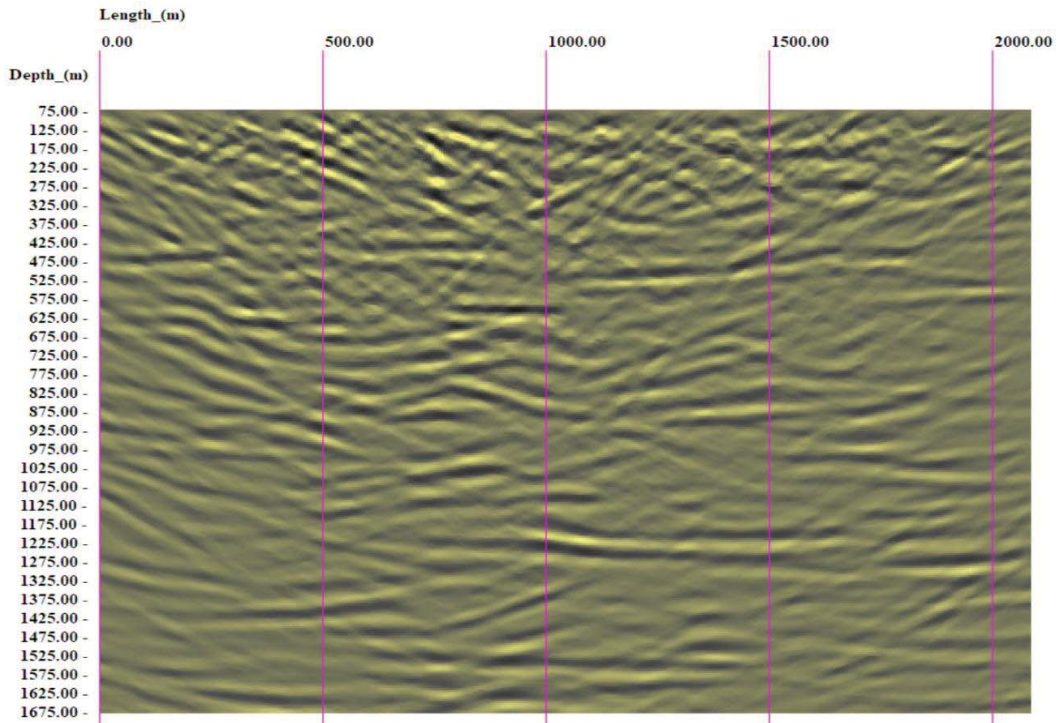


Figure 26. Line1.2 3D CMP Radon migration, (with amplitude equalization & trace balancing).

A sharper version of the migrated profile shown in Figure 26 was obtained, as illustrated in Figure 27 by bi-dimensional band pass filtering (0.004 m^{-1} - 0.016 m^{-1} to 0.04 m^{-1} - 0.06 m^{-1} along the Depth axis and 0.00 m^{-1} - 0.003 m^{-1} to 0.01 m^{-1} - 0.03 m^{-1} along the line Length axis). Note that in a distance-depth profile, the band-pass values are wavenumbers. In this representation, certain coherent patterns noticeable as continuous over large areas appear to be composed of shorter, more local portions, occasionally also displaying a vertical shift between adjacent ones. The procedure is therefore useful for finding and interpreting discontinuities with higher accuracy. Conversely, the more extensive features which can be recognized in the wider band profiles like the one in Figure 26 enable recognizing possible site-scale trends.

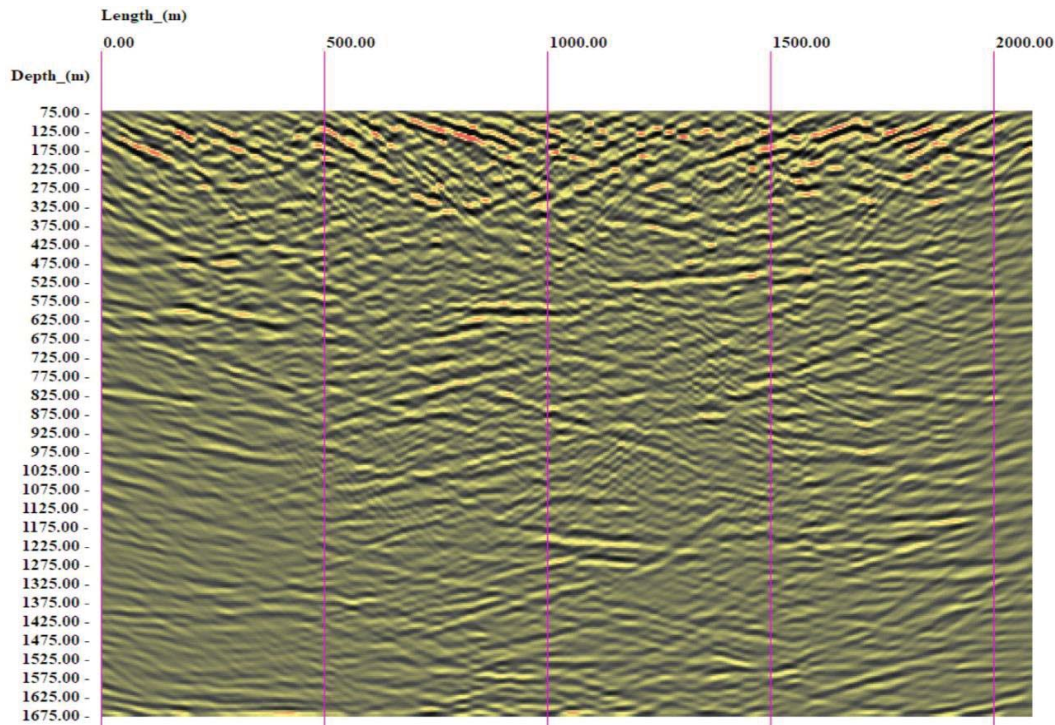


Figure 27. Same as in Figure 26, with band pass filtering and spectral equalization.

To take advantage of the crooked line geometry, migration was performed for a range of ‘off-plane’ dips. As shown in Appendix B, equation B1, and exemplified in Figure 28, the apparent ‘depth’ in a migrated section generated from crooked line data varies with the ‘off-plane’ angle.

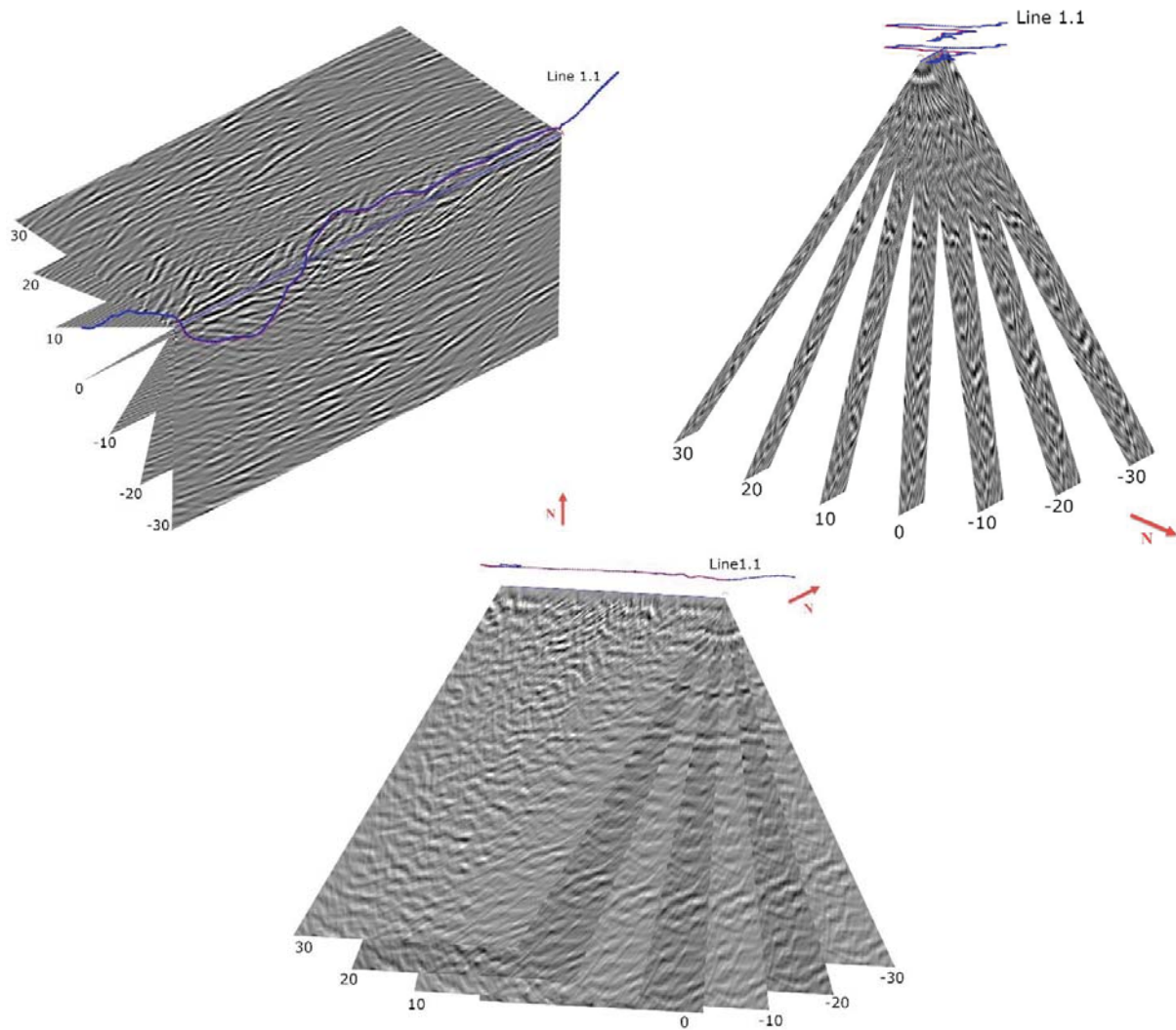


Figure 28. 3D migration oriented to different directions around the migration axis. 0 denotes vertical down direction below the migration axis, while ± 10 , ± 20 and ± 30 mark the directions 10° , 20° and 30° laterally up from vertical, on both sides of the vertical down plane.

Based on the refraction tomographic inversion results detailed in Section 3.4, the effects of the overburden and weathering essentially disappear below a depth of approximately 75 m, the compressional velocity in the bedrock displaying a rather uniform value $V_p=5750$ m/s. However, refraction tomography indicates this velocity in the upper rock layer. At larger depths the velocity is possibly higher.

A fitting procedure of the depths of reflectors interpreted from seismic and the depths of events present in the IG_BH01 borehole logs was used to derive a velocity vs. depth function. A “marker” reflector, identified in borehole IG_BH01 as described in Figure 60 was used for calibration. A good fit between seismic reflectors and IG_BH01 events was obtained for a gradual increase from $V_p = 5750$ m/s to $V_p = 6000$ m/s between 75 m and 300 m depth and $V_p = 6000$ m/s at depths larger than 300 m below surface. The migrations were recomputed with this assumption, the result being displayed in Figure 29 for the initial guess $V_p = 5750$ m/s below 75 m depth and Figure 30 with increasing the velocity to $V_p = 6000$ m/s below 300m depth, which agrees with the general trend of the V_p sonic log in borehole IG_BH01, as shown in Figure 61, Appendix A.

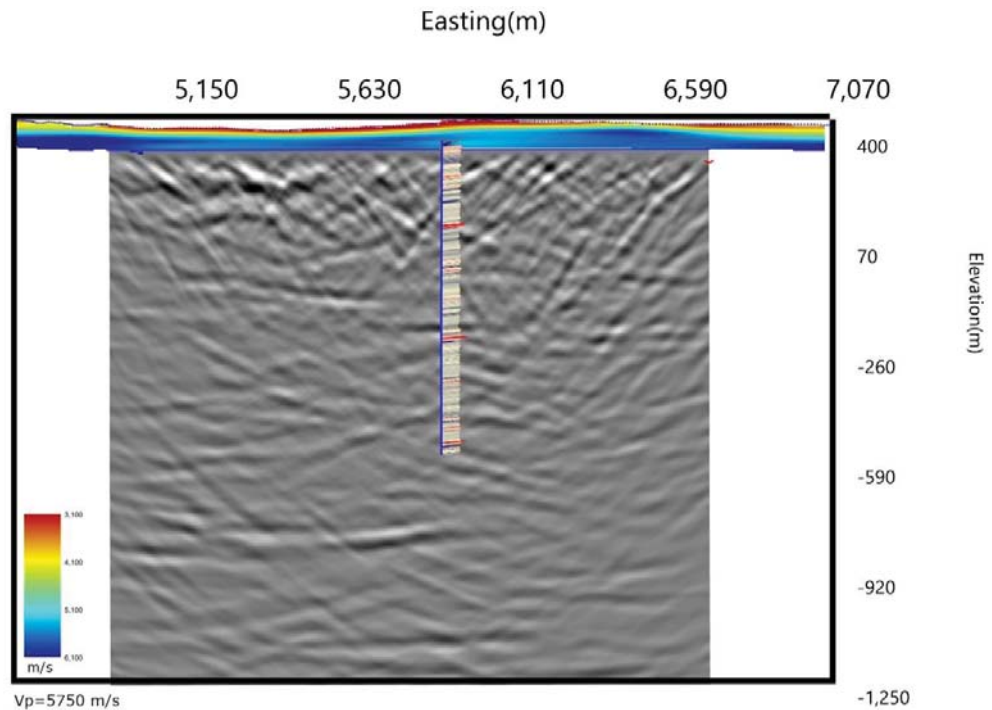


Figure 29. Line 1.2 migrated section, with $V_p=5750$ m/s, together with the reflectivity log along borehole IG_BH01 and the near surface velocity profile along the same line. Depth scale is as shown in Figure 35.

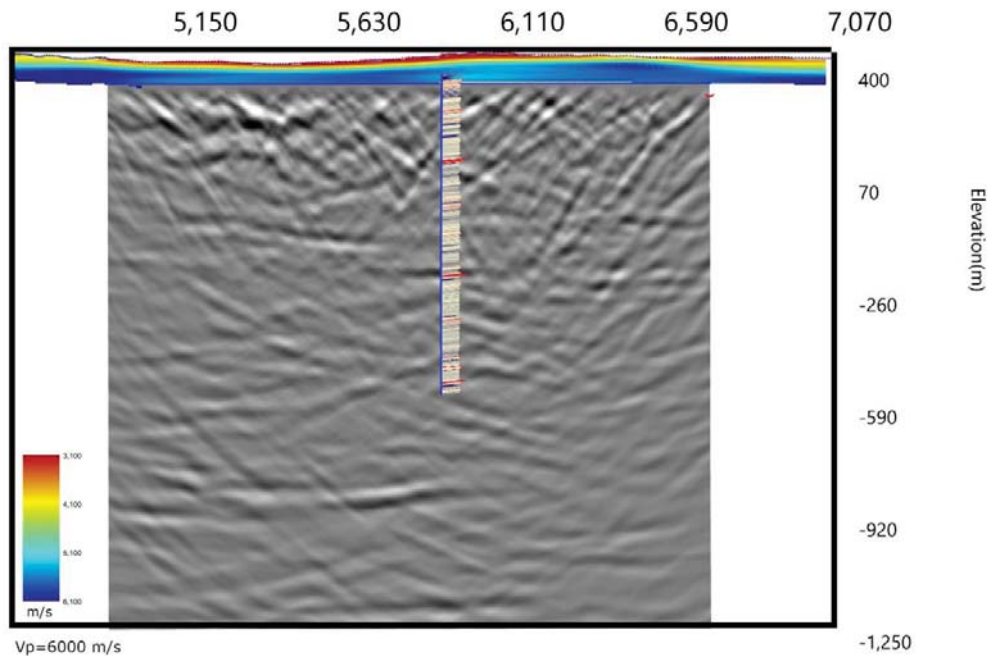


Figure 30. Line 1.2 migrated section, with $V_p=6000$ m/s, together with the reflectivity log along borehole IG_BH01 and the near surface velocity profile along the same line. Depth scale is as shown in Figure 35.

Sections 3.8.1 to 3.8.8 present front views of the depth migrated results computed vertically down, as 3D CMP Radon migration and 3D CMP Radon migration with bi-dimensional high pass and spectral equalization. The corresponding 3D Kirchhoff migrated sections are shown in Appendix C. The velocity field used consists of a variable velocity layer derived by tomography from surface to 75 m depth under each source/receiver station, a transition from 5750 m/s to 6000 m/s between 75 m and 300 m and a constant 6000 m/velocity below 300 m depth below surface.

Likewise with the tomographic inversion described in Section 3.4, segmenting Line 1 into two parts appears to be the better option for imaging the reflectors directly beneath the line, as processing the whole Line 1 can lead to offsets too large from the locations where actual reflections occur. It was not used here in subsequent interpretation. However, examining the Line 1 data processed as one set can be useful as an additional tool in the attempt to recognize steep, off line targets. The full length Line1 is shown in Section 3.8.1. Line1.1 and Line1.2 are approximately equal in length and nearly perpendicular. As such, they image very different regions of the bedrock. It has therefore been opted to use Line 1.1 and Line 1.2 for interpretation and further studies. It must be noted that the straight lines used to position the processed profiles are merely best fit axes for the actual crooked lines while migrations are computed in 3D.

As discussed in this section, the Kirchhoff migrations were computed primarily as a reference to a commonly used processing routine. The higher noise and reduced coherence make them less useful for interpreting site-scale features. They can however occasionally find limited use with confirming local details in the profiles, e.g., phase discontinuities caused by crossing events with different dips.

Both versions of the CMP Radon migrations were used for interpretation. The full band version has been useful for inferring wider site trends and, where applicable, fitting amongst different profiles. The band pass filtered versions offer more detail and have been found more informative for interpreting discontinuities.

3.8.1 3D migrations, Line 1

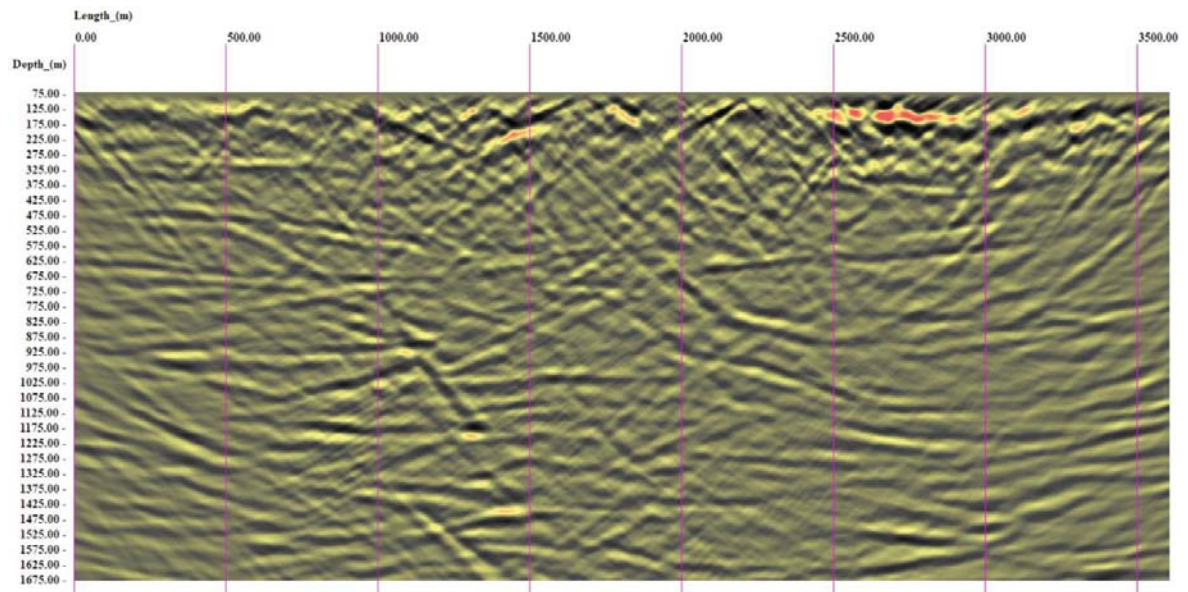


Figure 31. Line1 3D CMP Radon migration with amplitude equalization & trace balancing.

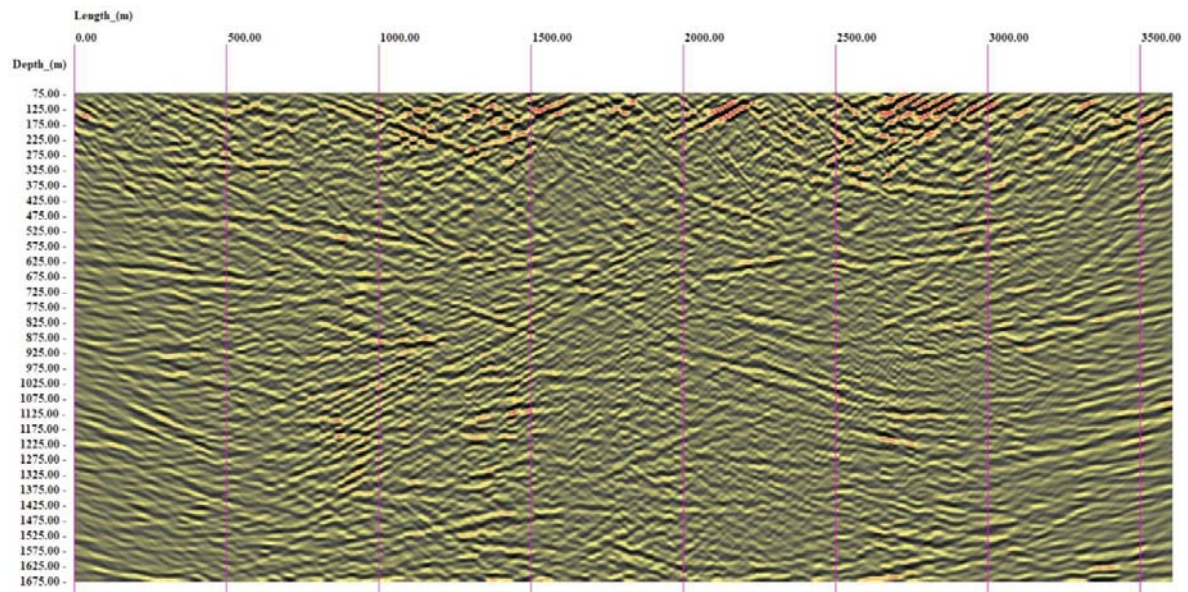


Figure 32. Same as in Figure 31, with bi-dimensional band pass filtering and spectral equalization.

3.8.2 3D migrations, Line 1.1

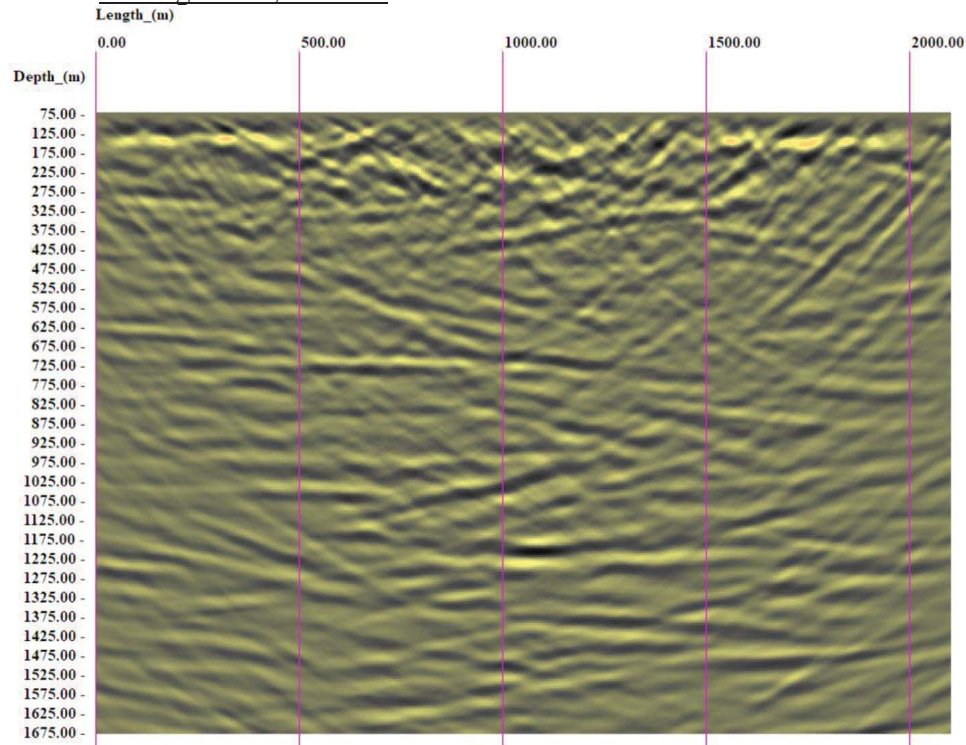


Figure 33. Line1.1 3D CMP Radon migration, with amplitude equalization & trace balancing.

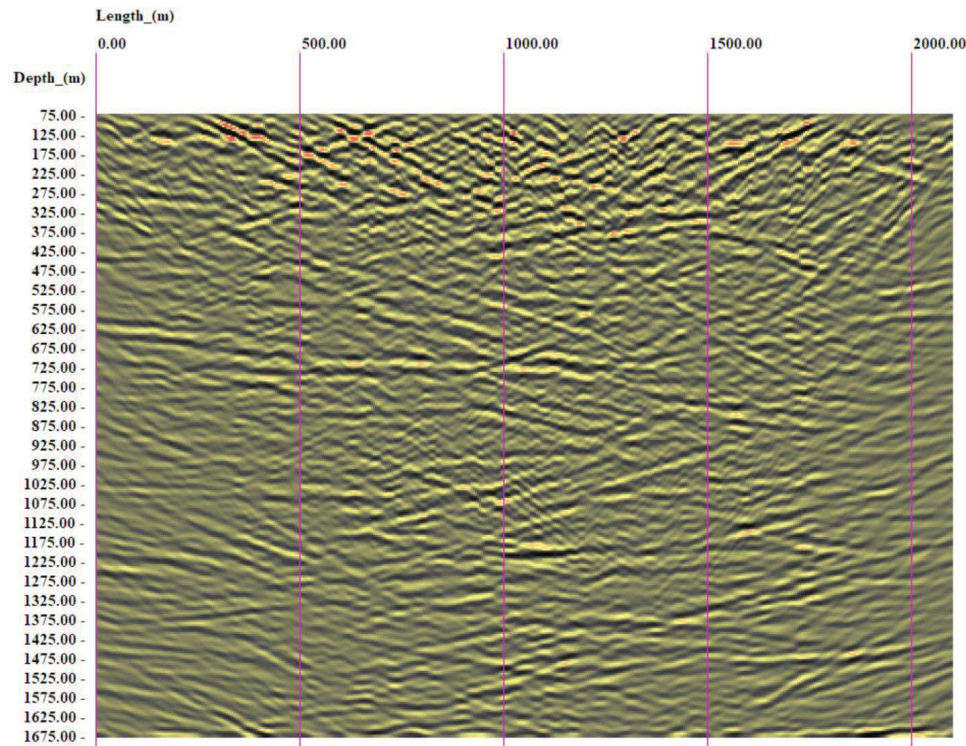


Figure 34. Same as in Figure 33, with bi-dimensional band pass filtering and spectral equalization.

3.8.3 3D migrations, Line 1.2

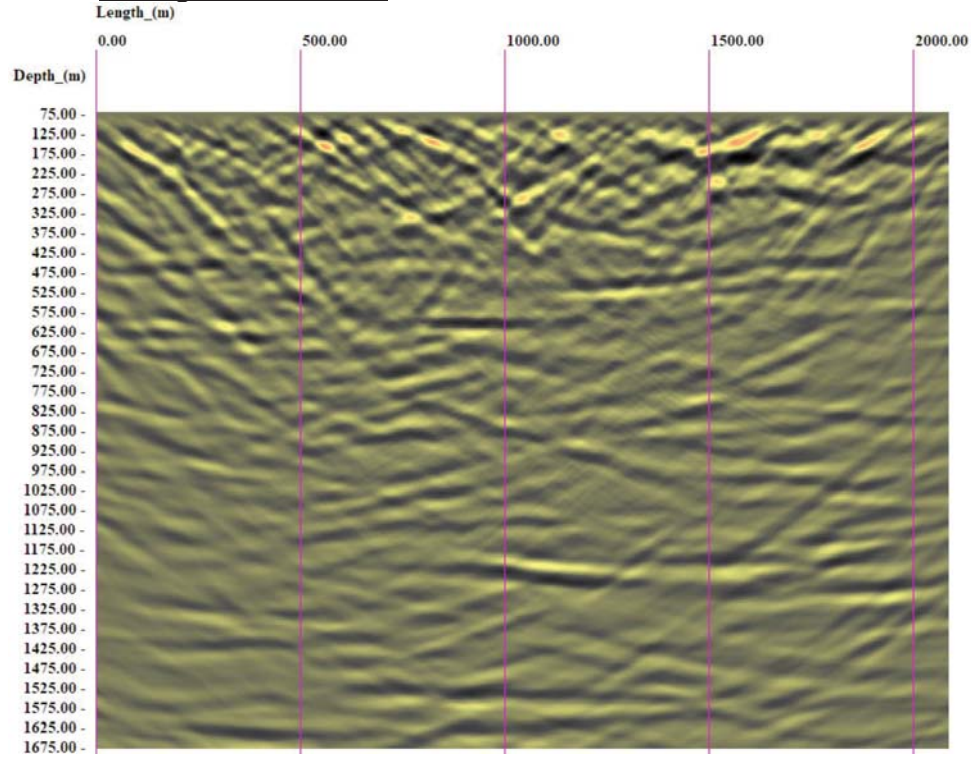


Figure 35. Line 1.2 3D CMP Radon migration with amplitude equalization & trace balancing.

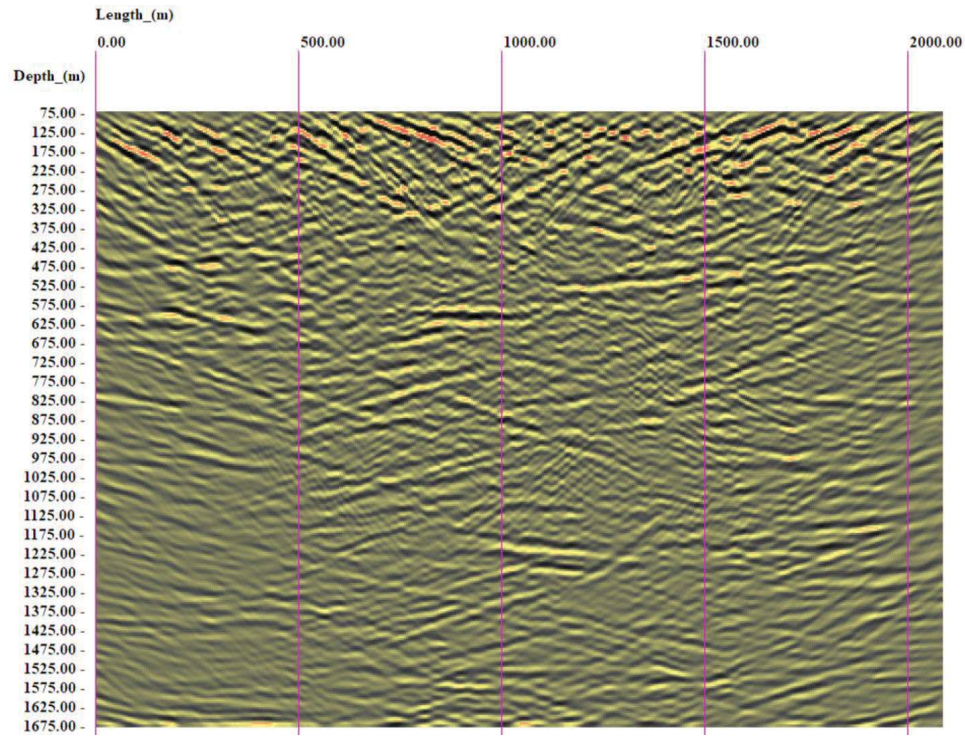


Figure 36. Same as in Figure 35, with bi-dimensional band pass filtering and spectral equalization.

3.8.4 3D migrations, Line 2

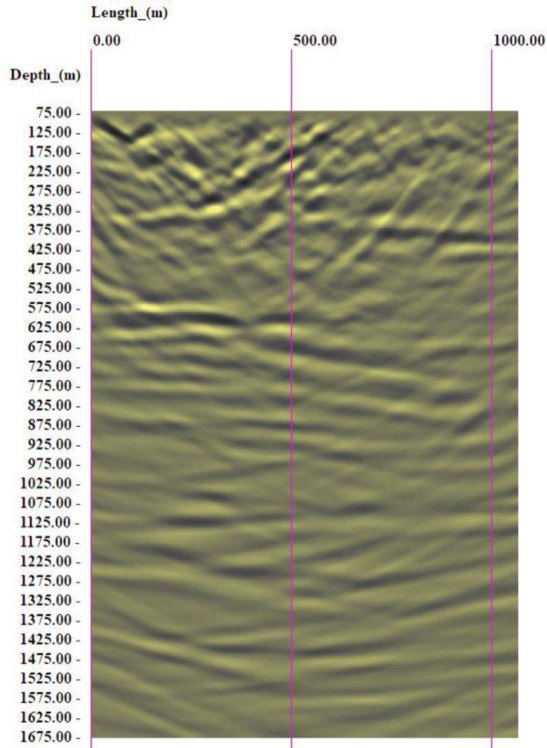


Figure 37. Line 2 3D CMP Radon migration with amplitude equalization & trace balancing.

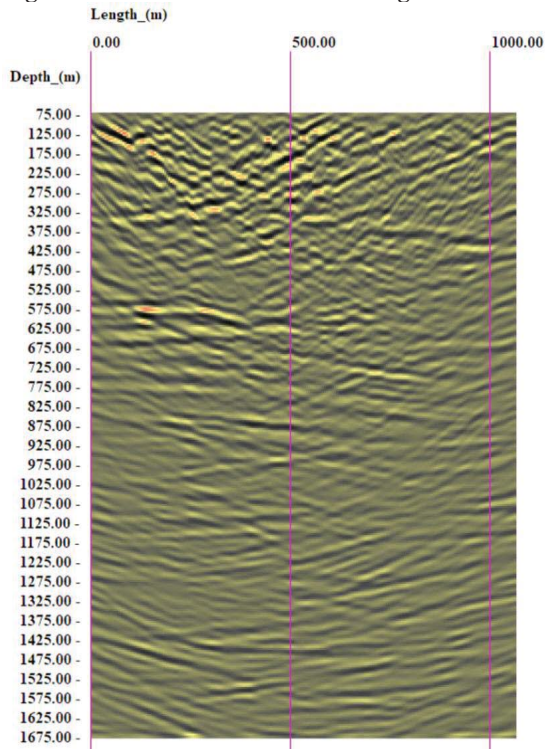


Figure 38. Same as in Figure 37, with bi-dimensional band pass filtering and spectral equalization.

3.8.5 3D migrations, Line 3

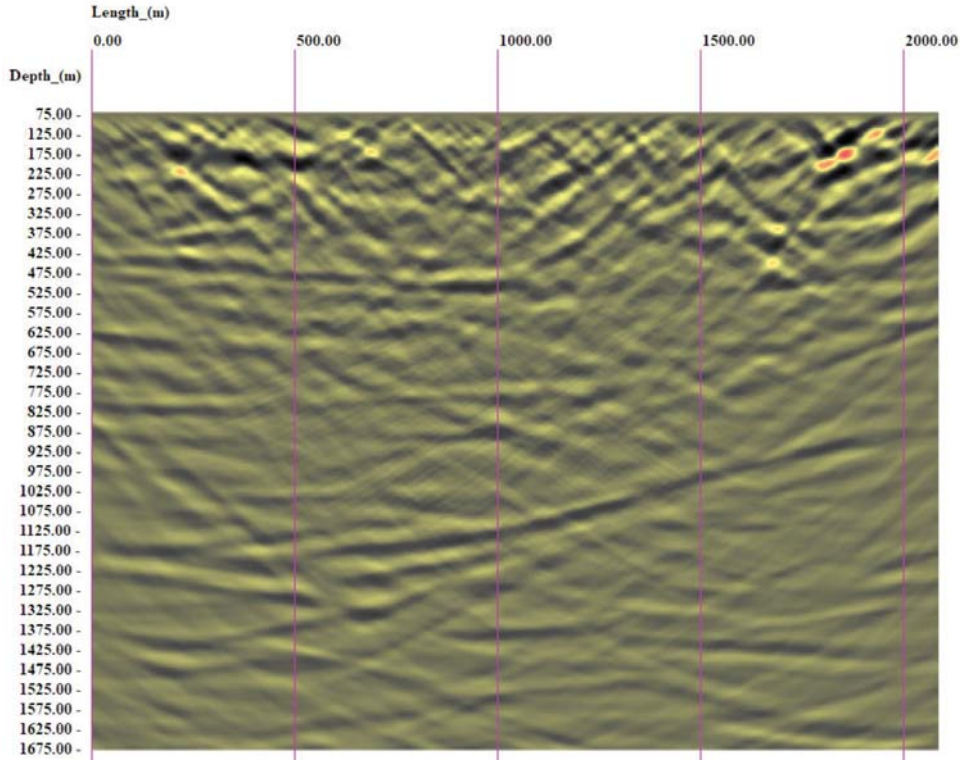


Figure 39. Line 3 3D CMP Radon migration with amplitude equalization & trace balancing.

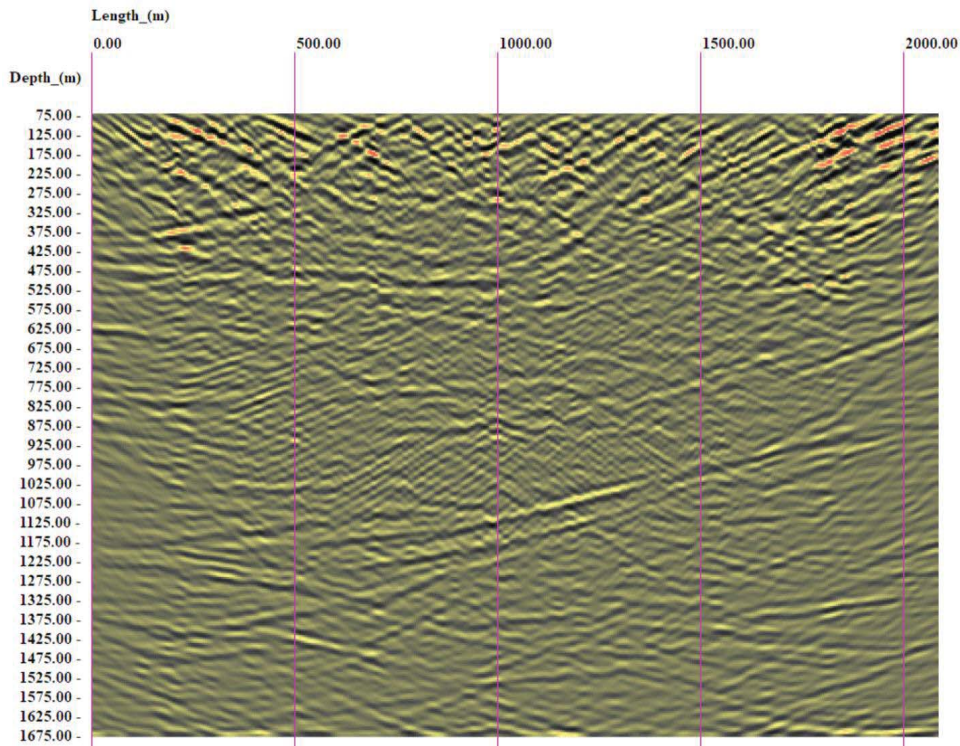


Figure 40. Same as in Figure 39, with bi-dimensional band pass filtering and spectral equalization.

3.8.6 3D migrations, Line 3.1

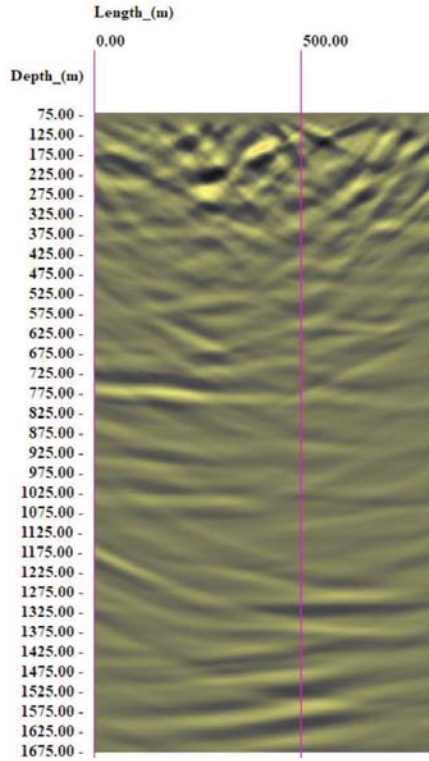


Figure 41. Line 3.1 3D CMP Radon migration with amplitude equalization & trace balancing.

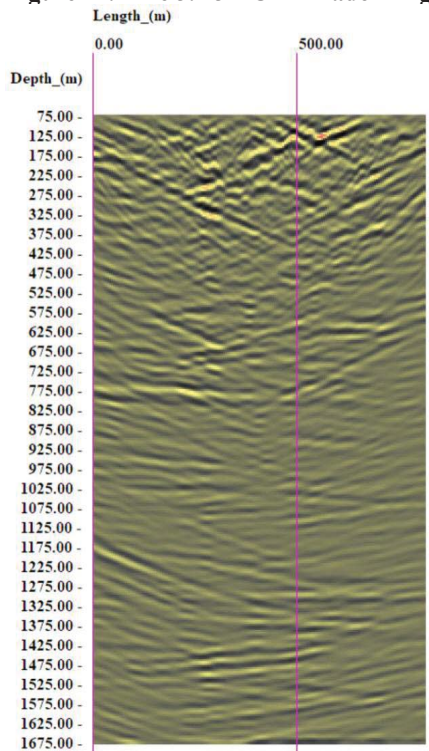


Figure 42. Same as in Figure 41, with bi-dimensional band pass filtering and spectral equalization.

3.8.7 3D migrations, Line 4

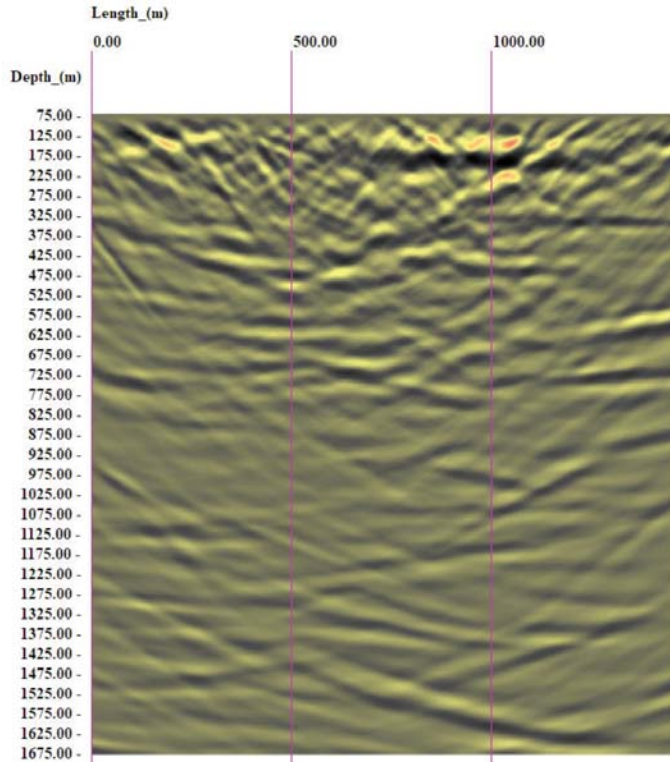


Figure 43. Line 4 3D CMP Radon migration with amplitude equalization & trace balancing.

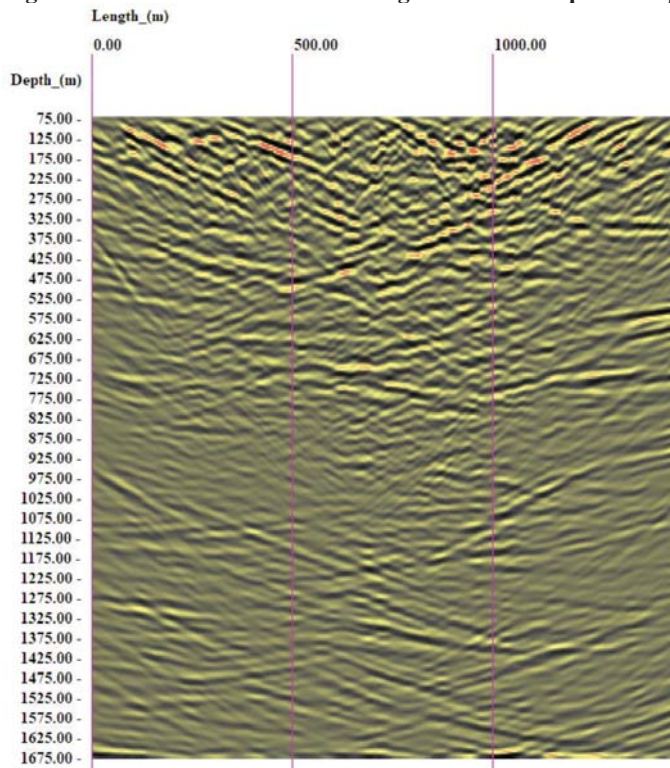


Figure 44. Same as in Figure 43, with bi-dimensional band pass filtering and spectral equalization.

3.8.8 3D migrations, Line 5

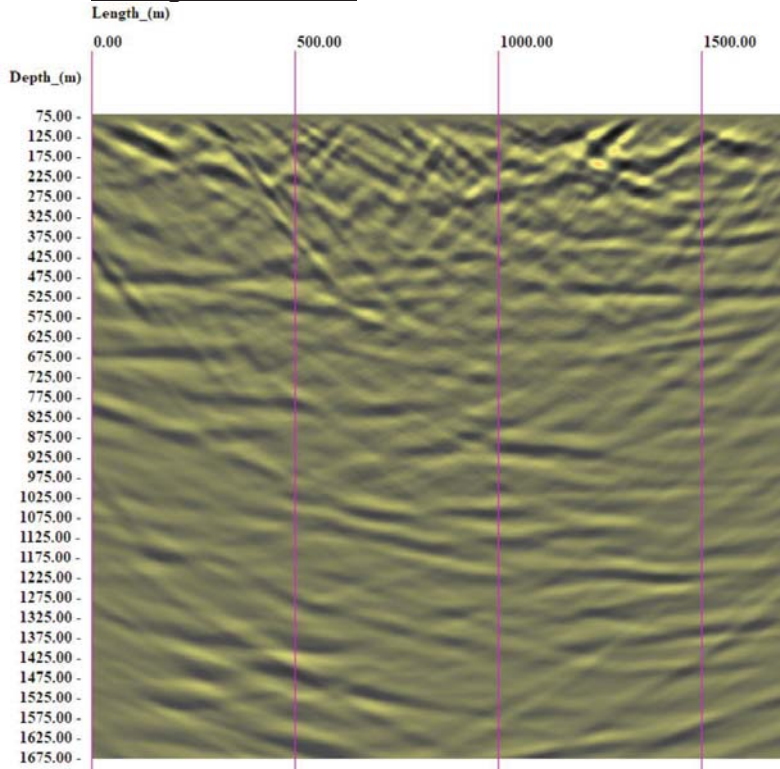


Figure 45. Line 5 3D CMP Radon migration with amplitude equalization & trace balancing.

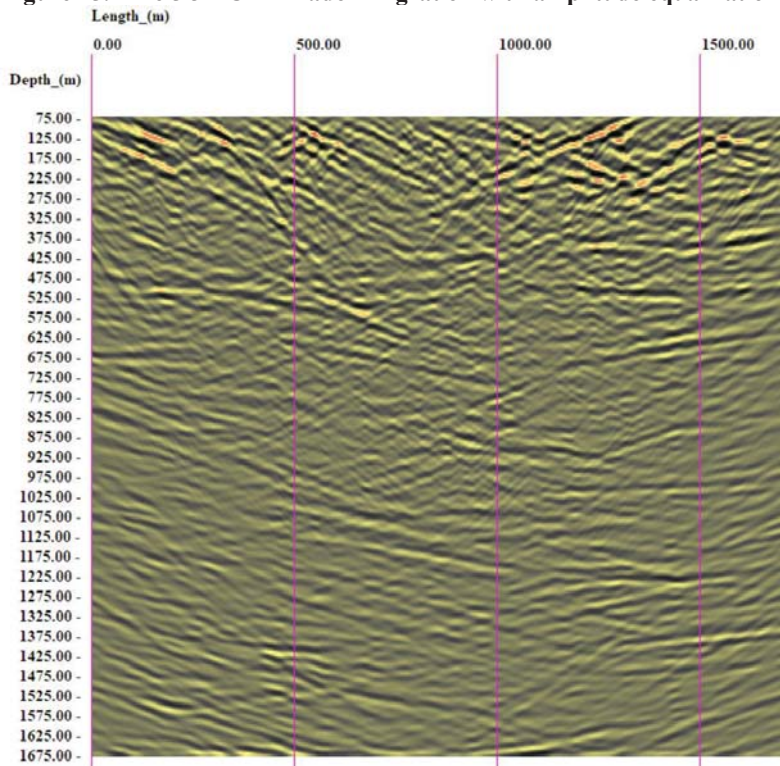


Figure 46. Same as in Figure 45, with bi-dimensional band pass filtering and spectral equalization.

4 Reflector interpretation and positioning

The Revell Batholith is composed primarily of biotite granodiorite-tonalite to biotite tonalite (representing more than 97% of the bedrock encountered in three boreholes), accessory felsic dykes and amphibolite. Seismic impedance calculated in borehole IG_BH01 shows mainly low-magnitude variability associated with most of the geological features in the borehole, such as intervals of higher fracture frequency and the suites of felsic dykes. The largest impedance contrasts in the borehole occur at locations of observed amphibolites, which have a significant density contrast with the main biotite granodiorite-tonalite bedrock. The limited impedance contrasts between the other geological features in the borehole prevent seismic from being a reliable reflector discriminator.

Figure 47 and Figure 49 present 3D images of all full-band migrated profiles viewed from the south and from the north, respectively. Several sub-horizontal and shallow dipping features are evident in each profile and, in some cases, appear to continue from one profile to another, forming possible pseudo-surfaces that are continuous across the site. Overall, the observed reflections have diverse orientations, crisscrossing each other at various angles. However, most reflected features are dipping generally northerly with most apparent dip values below 20 degrees.

Reflections were traced in the seismic profiles by looking at phase continuity and amplitude of the reflection. As an initial threshold, a trace length of approximately 500 m of minimum perceived continuity has been considered as a target threshold for an interpretable reflector, with the degree of confidence increasing for two or more contiguous segments. This threshold was identified to interpret the most significant reflections within the seismic data. In addition, the apparent continuity of reflections from one profile to another was also used during the interpretation to increase the degree of confidence of the reflection trace. However, the continuity of the seismic features appears as enhanced in the full-band migrations, due to the smoothing effect of the lower frequencies, hence the continuity can also be overemphasized (i.e. Figure 47 and Figure 49). Furthermore, the continuity along the edges of the profiles may vary when profiles are migrated in a non-vertical direction, as shown in Figure 28. Therefore, such continuity trends should be considered carefully, and their validity checked more locally in the band-pass filtered profiles, as the ones shown in Figure 48 and Figure 50, when interpreting reflection patterns. This is shown in Appendix D. The possible continuity across profiles of the seismic features interpreted in single profiles is illustrated in Section 4.1.

Reflections in the upper 250 to 300 m of the section tend to have also higher apparent dip angles and also display higher overall amplitudes, as revealed by the more intense coloring in Figure 47 to Figure 50. Both higher apparent dips and amplitudes can be caused by shallow off-plane back scattering, as discussed in Section 4.2. The shallow events fulfilling the 500 m minimum perceived continuity condition set to be identified as reflectors, were nonetheless retained in order to maintain consistent reflector picking criteria. These shallow off-plane back scattering effects are believed to be partly caused by off-plane refracted arrivals possibly from steeply dipping and sub-vertical features. These events are suggested not to be moderately dipping features in the seismic section.

Based on the seismic impedance from IG_BH01, it is believed that the majority of high-amplitude reflections in the seismic data are the result of discrete amphibolite units in the subsurface. It is possible, however, that individual interpreted seismic reflections may also

represent zones of amphibolites that are either clustered together or are laterally continuous as different segments of amphibolites throughout the subsurface.

Although increases in fracture frequency observed in IG_BH01 do not directly correlate with seismic impedances or observed seismic reflections, it is possible that elevated fracture frequencies at other locations in the subsurface may possess such an impedance contrast to result in a reflection. Likewise, elevated fracture frequencies may result in increased phase continuity, thus fulfilling the phase criterion of interpretable reflectors.

However, both amphibolites and local increases in fracture frequencies observed in boreholes IG_BH02 and IG_BH03 could be linked to possible high amplitude reflections within the seismic data in proximity to the boreholes. Making a direct correlation in this case is difficult due to these boreholes IG_BH02 and IG_BH03 plunging southerly, away from the edge of the seismic data.

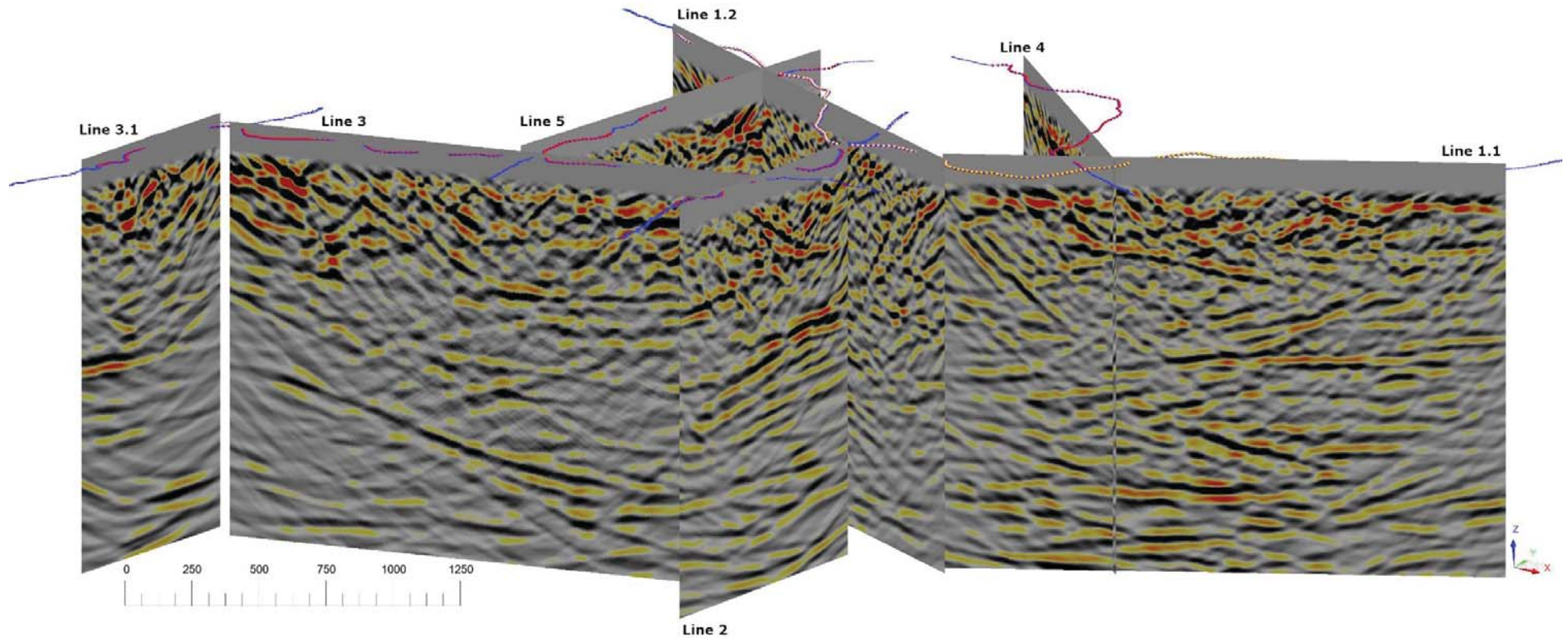


Figure 47. Full-band migrated profiles viewed from the S-SE. Scale bar is in meters.

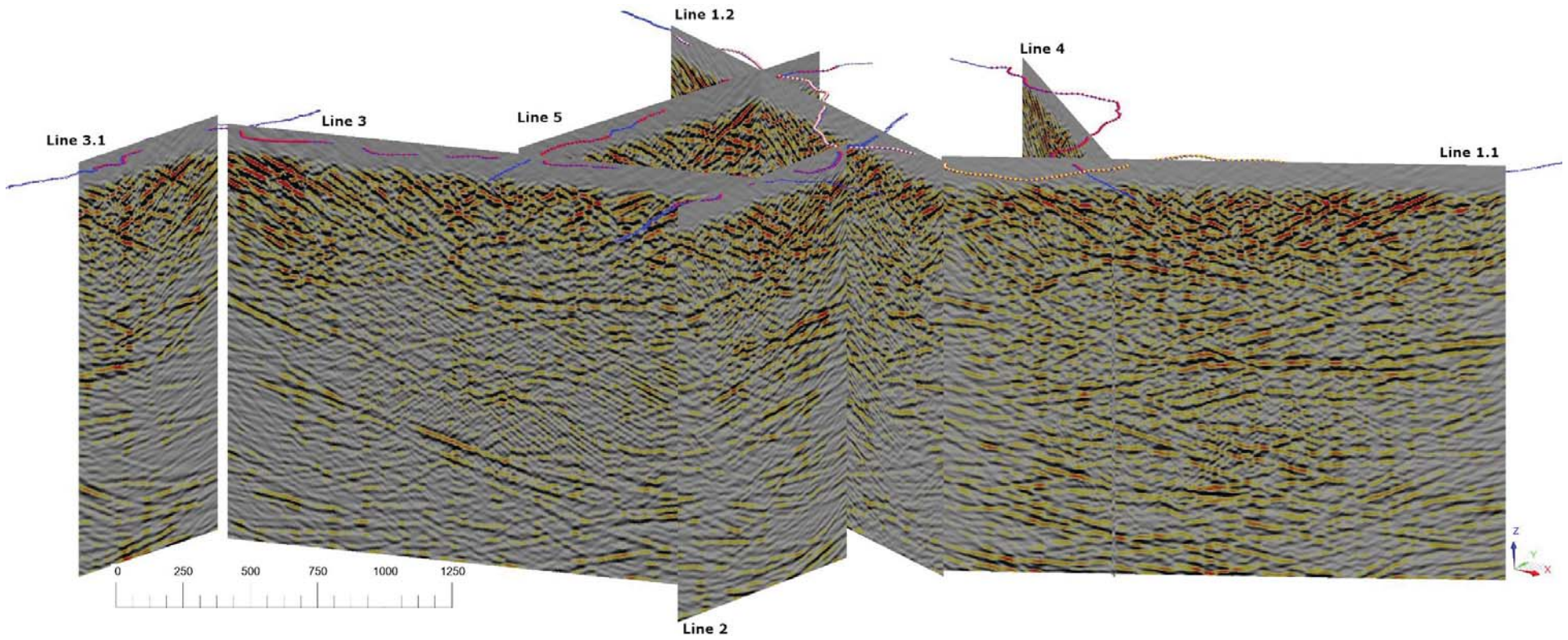


Figure 48. High band pass filtered migrated profiles viewed from the S-SE. Scale bar is in meters.

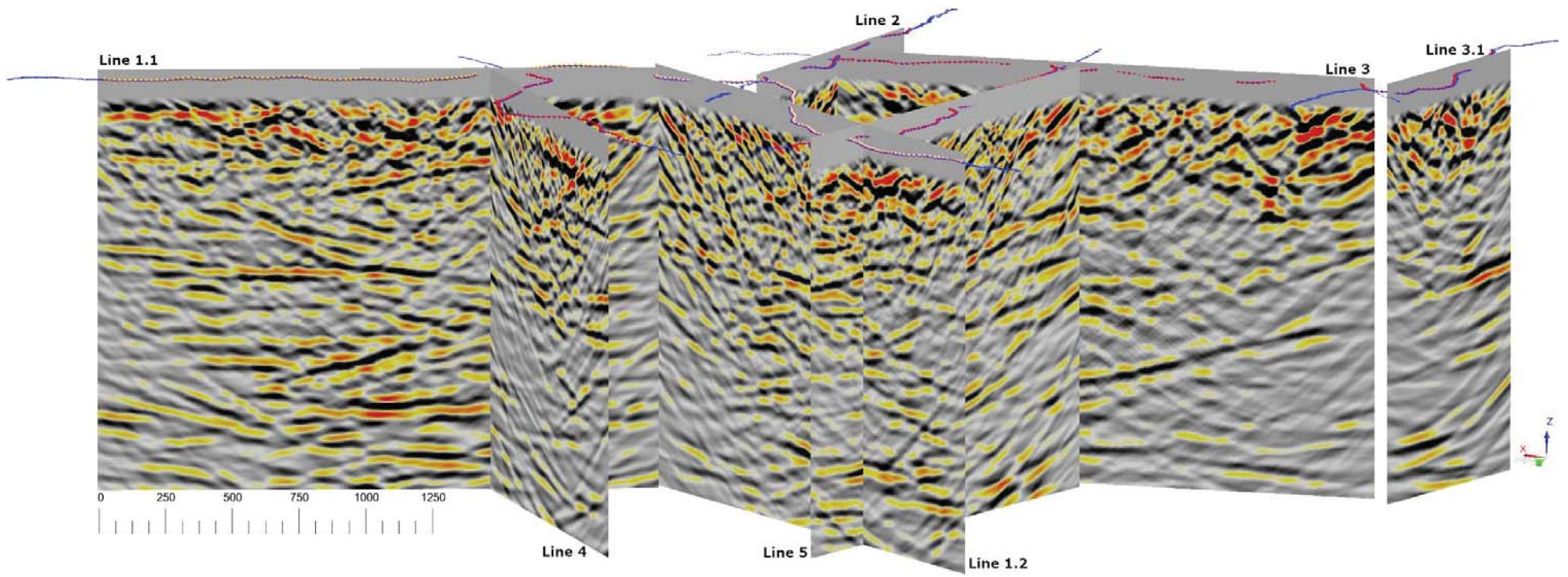


Figure 49. Full-band migrated profiles viewed from the N-NW. Scale bar is in meters.

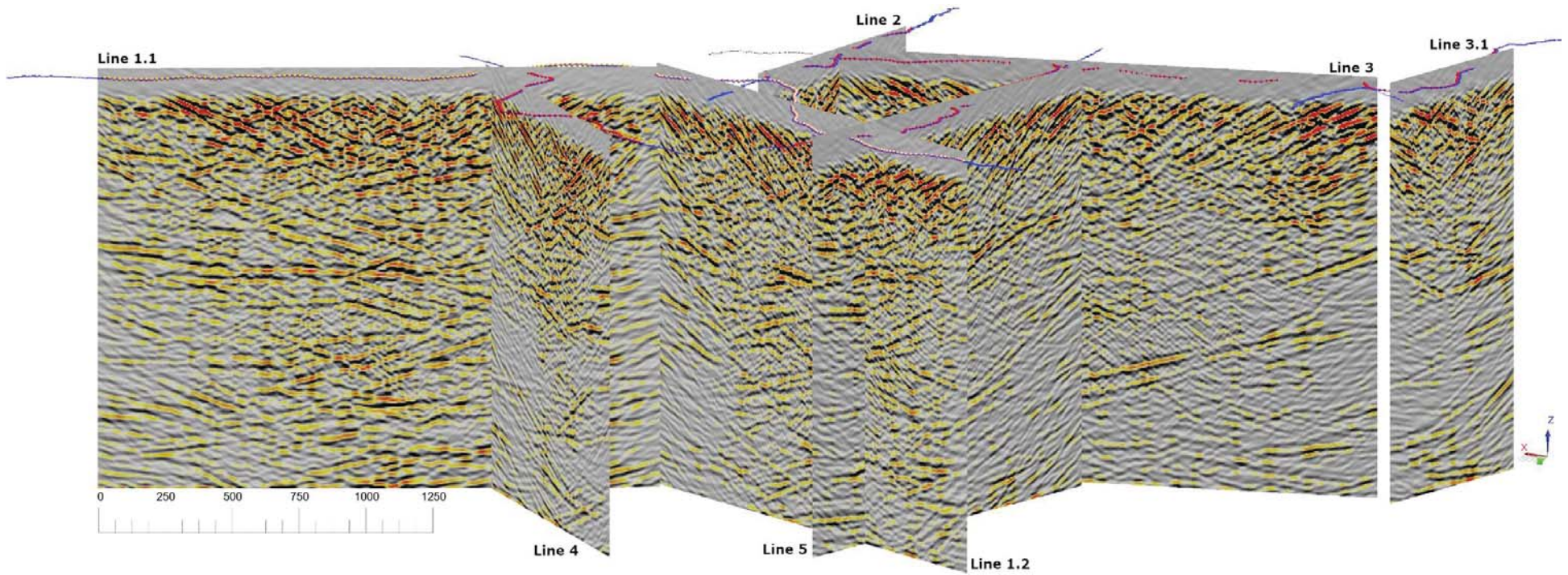


Figure 50. High band pass filtered migrated profiles viewed from the N-NW. Scale bar is in meters.

4.1 Validation of reflectors in multiple seismic lines

The continuity of seismic features from one migrated profile to another can help defining their dominant dip and strike. However, joining different parts of a seemingly continuous geometrical trend as one and the same feature can be subjective. The main difficulty in hard rock is that the continuity of a feature must be followed while it is criss-crossing with other features, locally vanishes or is transversely offset. To make the decision on the continuity, hence of the identity, of a given feature one has to take into consideration knowledge including structural geology as well as analyze borehole logging and other seismic and geophysical data at various scales, as available.

4.1.1 Line 1.1 and Line 1.2

Figure 51 and Figure 52 display migrated profiles along Line 1.1 and Line 1.2, these jointly forming the longest lined measured, with an average orientation approximately E-W. Both these figures display the seismic reflectivity log along borehole IG_BH01, inferred from velocity and density geophysical logging, while Figure 52 shows also the interpreted seismic reflectors, as in Figure 72 and Figure 73 (Appendix D). There is a good correlation between the interpreted seismic reflection events and the seismic reflectivity log in borehole IG_BH01, although the difference of scale between seismic and logging data makes the correlation difficult to discern in Figure 52. It is easier to observe the correlation in Figure 60 (Appendix A), where the synthetic seismograms along borehole IG_BH01 and the Line 1.2 migrated section have similar spatial frequencies. The interpreted reflector events are mostly sub-horizontal and gently dipping, in a northerly direction, with some variations (NW-N-NE) and appear to continue between Line 1.1 and Line 1.2.

Some of the events appearing deeper than the bottom of the borehole IG-BH01 (below -500 m elevation) display slightly larger apparent dips, of approximately 20 degrees or higher, both E-NE and W-SW, and are also continuing in both profiles.

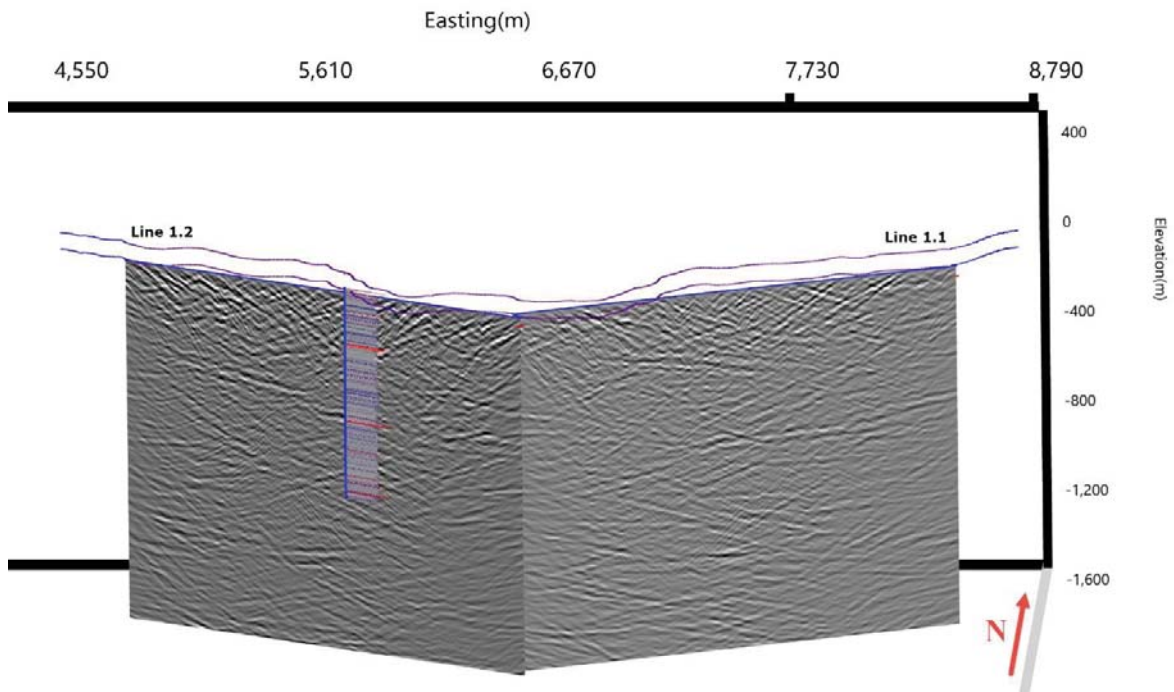


Figure 51. 3D view of migrated sections for Line 1.1 (same as in Figure 34) and Line 1.2 (same as in Figure 36), together with the seismic reflectivity log along borehole IG-BH01. View from S-SW. Easting and Northing labels show reduced coordinates (after removal of least significant digits: 5480000 was subtracted on Northing and 550000 was subtracted on Easting).

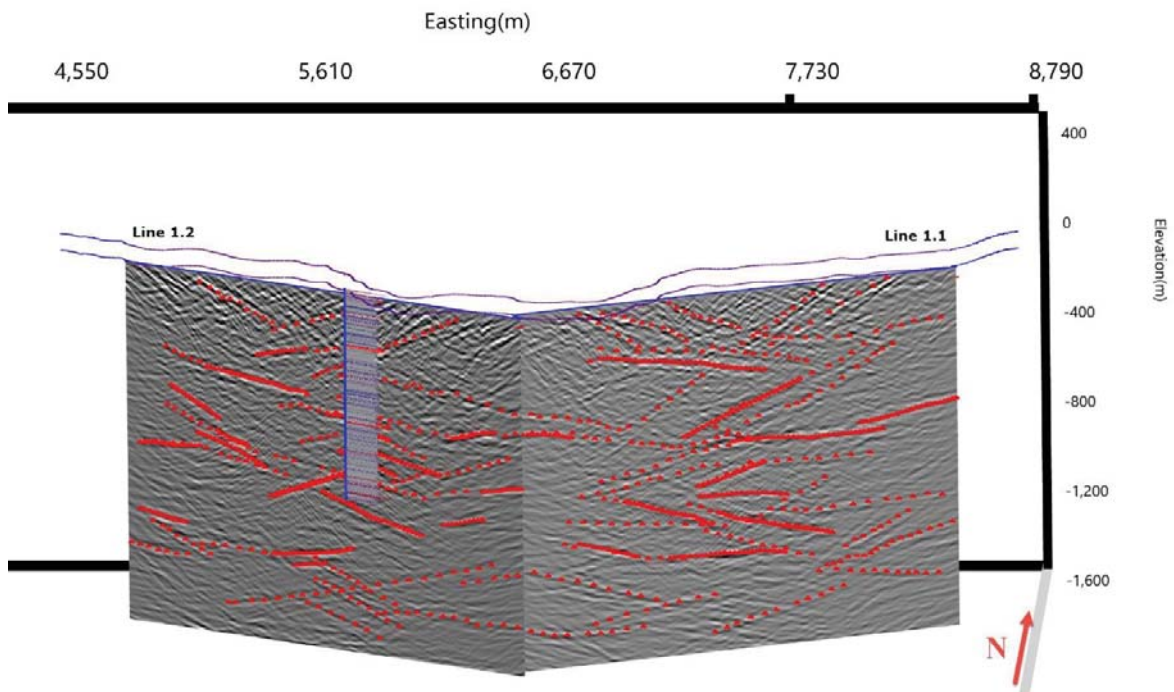


Figure 52. 3D view of migrated sections for Line 1.1 (same as in Figure 34) and Line 1.2 (same as in Figure 36), together with the seismic reflectivity log along borehole IG-BH01 and the interpreted seismic reflectors. View from S-SW.

4.1.2 All Seismic Lines

Figure 53 and Figure 54 display 3D views of all migrated profiles, with the seismic reflectivity logs along boreholes IG_BH01, IG_BH02 and IG_BH03 and the interpreted seismic reflectors, as previously shown in Appendix D.

As noted in the previous Section, a good correlation can be observed between the interpreted seismic reflection events and the seismic reflectivity borehole logs. The same gently and generally northerly dipping trends can be noticed, which continue between adjacent profiles.

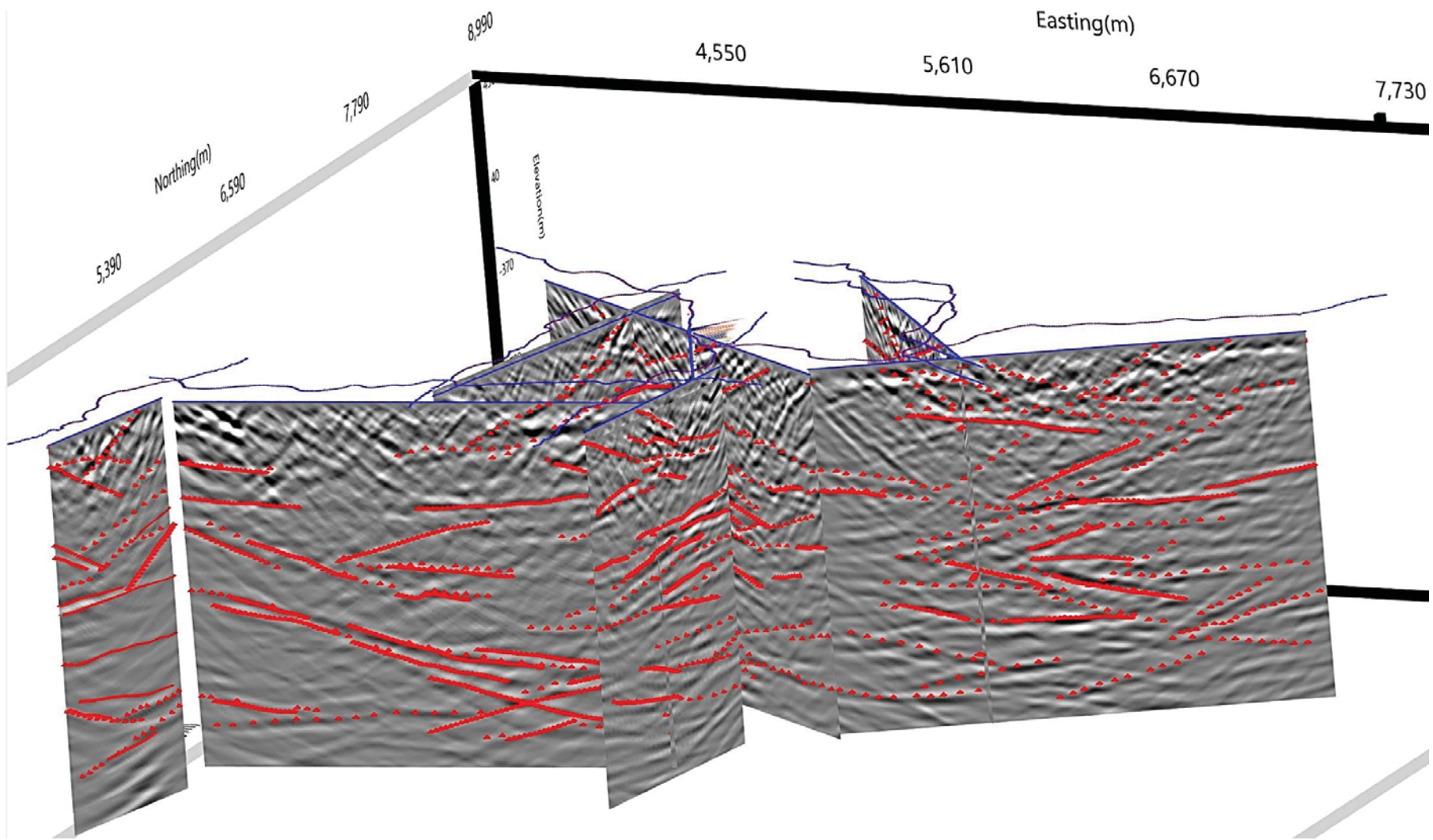


Figure 53. 3D view from S-SE of the bi-dimensional high-pass migrated profiles from all 2D lines, with the interpreted seismic reflectors. Easting and Northing labels show reduced coordinates (after removal of least significant digits: 5480000 was subtracted on Northing and 550000 was subtracted on Easting).

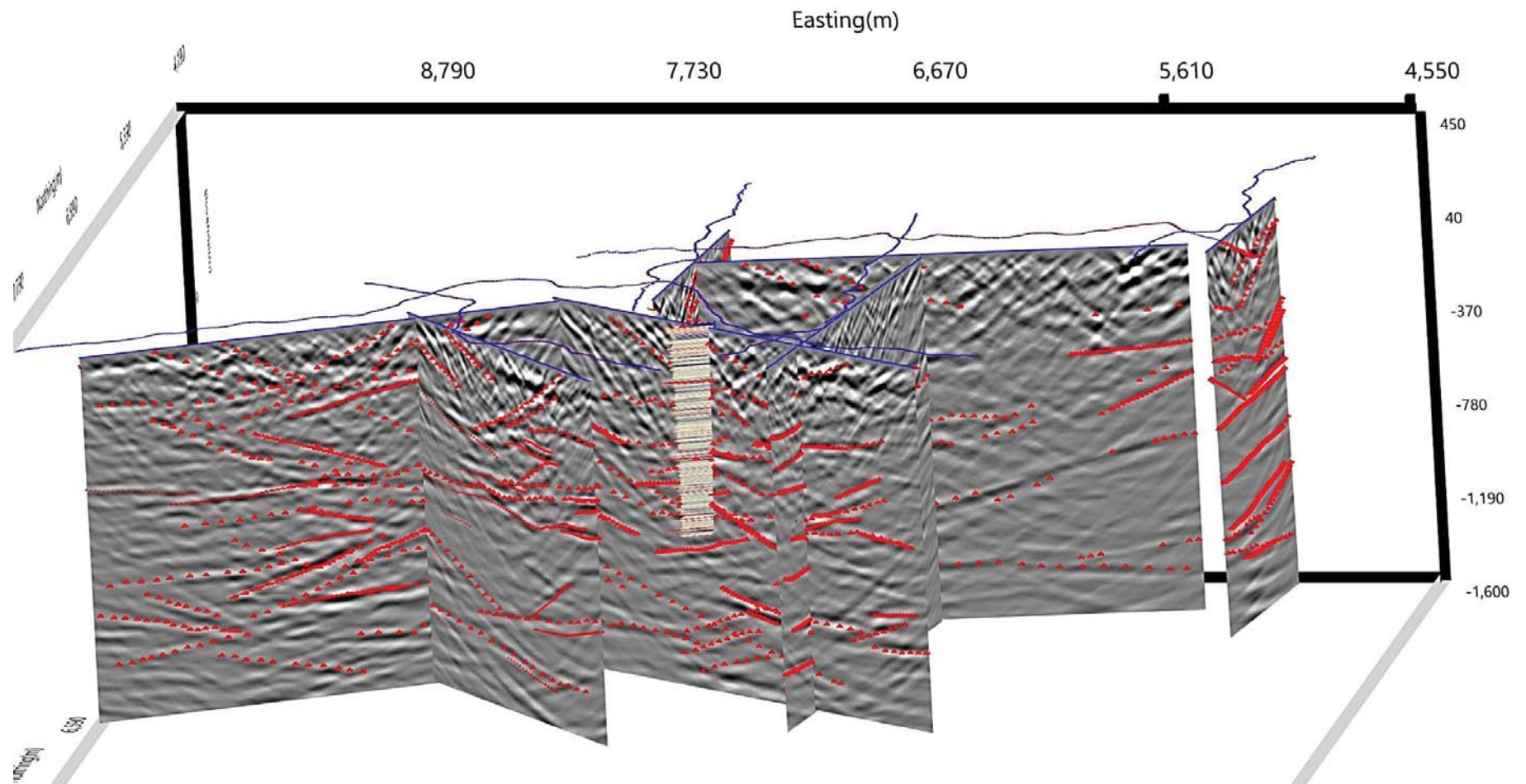


Figure 54. 3D view from N-NW of the bi-dimensional high-pass migrated profiles from all 2D lines, with the interpreted seismic reflectors. Easting and Northing labels show reduced coordinates (after removal of least significant digits: 5480000 was subtracted on Northing and 550000 was subtracted on Easting).

4.2 Shallow off-line reflections

As mentioned in the beginning of Section 4, the migrated profiles display an increased density of features in the upper 200-300m, which include events with higher apparent dip and amplitude. These are believed to be partly caused by off-plane refracted back scattering, i.e., by steeply dipping and sub-vertical features. We noted in Section 3.5 that tomographic inversion revealed a velocity contrast at approximately 75 m depth which causes the direct arrivals to be sharply refracted. This is further clarified by the example presented in Figure 55 which shows the same tomographic profile as Figure 17 (Line 5) with the addition of the refracted rays corresponding to a single source and all receivers on the profile. It can be seen that refracted wave fronts travelling horizontally leave the sources and arrive at the receivers almost vertically. This is also true for reflected wave fields. Shallow low-dip events appearing in the migrated profiles can in fact be refracted wave responses of high-dip scatterers positioned laterally to the lines and can therefore be treated as possible migration artifacts in the vertical or sub-vertical migrated profiles. The apparent depth of such possible artifacts is limited by the higher attenuation within the upper bedrock in which refracted wave fronts travel. This could be caused by subtle increased fracture intensity in the upper bedrock. High angle refraction therefore explains both the higher concentration of events in the shallow zone of 200-300 m and the overall increased energy in the upper region of the profiles.

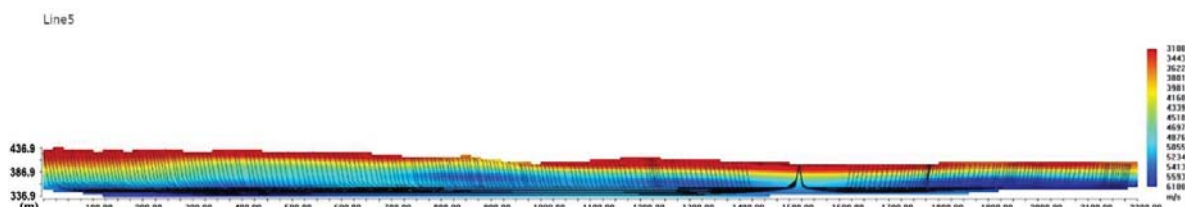


Figure 55. Tomographic reconstruction of the P wave velocity in the near surface along Line 5 with overlaid refracted rays for one source and all receivers. The velocity scale is the same for all lines, from 3100 m/s (red) to 6100 m/s (blue).

It should also be noted that some of the shallow scatterers appear as remarkably continuous coherent events, i.e., potential reflections. For this reason, we interpreted them as such in Appendix D, although, following the discussion above in this section, they may be positioned laterally rather than underneath the lines. These events are bound to be produced by targets either vertical or dipping towards the line, as reflectors that dip away from the acquisition line cannot return much wave energy from available sources to available receivers (Nedimovic, 2003b). For the crooked line layouts, the amplitude, position in the profile and shape of the events vary when rotating the profile around its datum axis. To test this possibility, we have produced horizontal migration profiles for Line 1.2 and Line 4.

Figure 56 and Figure 57 illustrate a known diabase dyke, presumed vertical, located in the proximity of Line 1.2 and Line 4. The upper graph of Figure 56 displays the horizontally migrated profile for Line 1.2. The lower graph of this figure shows the horizontally migrated profile for Line 4. Traces that could be associated with the dyke are visible in both Line 1.2 and Line 4.

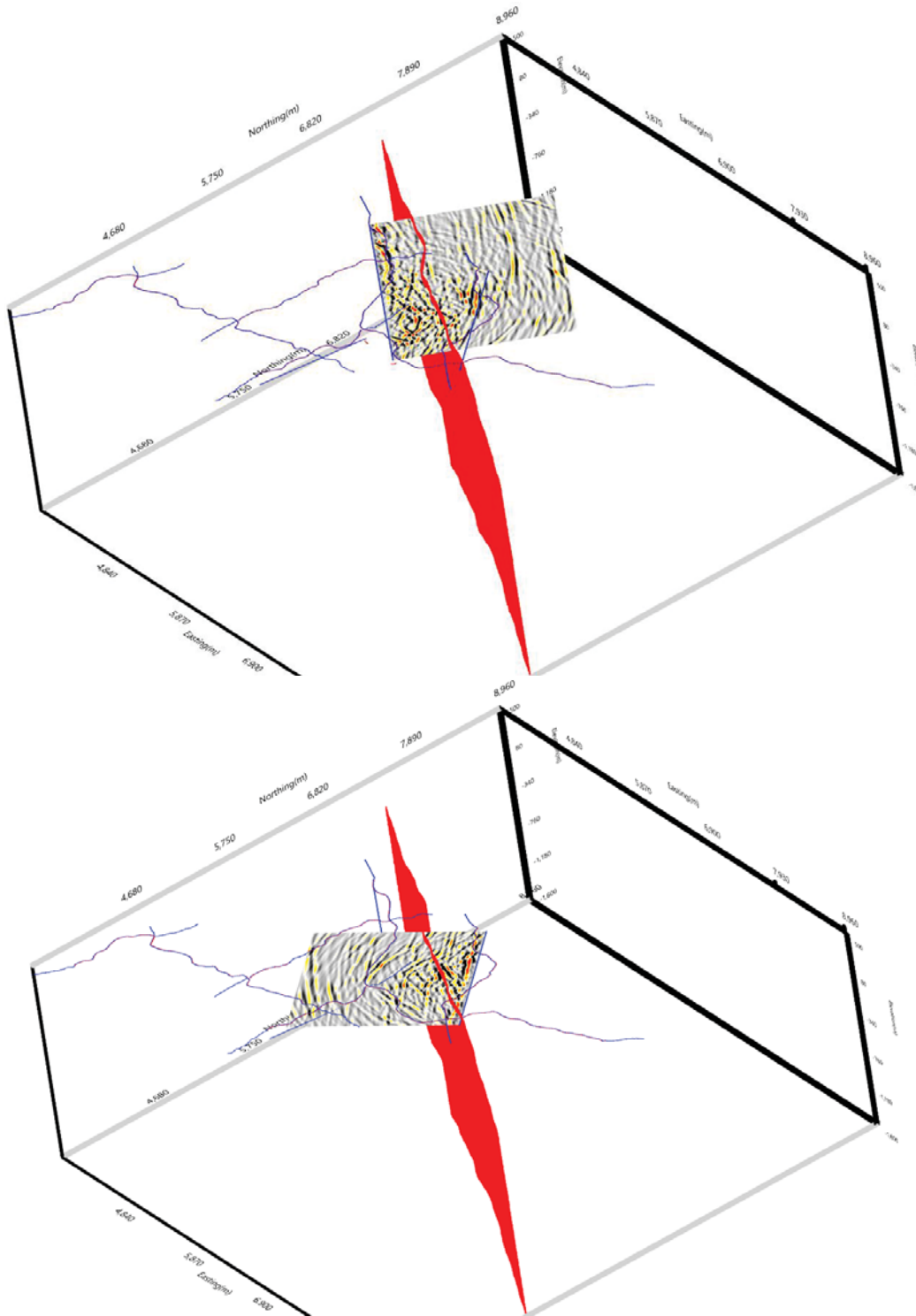


Figure 56. 3D view of the horizontally migrated profiles from Line 1.2 (top) and Line 4 (bottom), together with the steeply dipping dyke (red). Easting and Northing labels show reduced coordinates (after removal of least significant digits: 5480000 was subtracted on Northing and 550000 was subtracted on Easting).

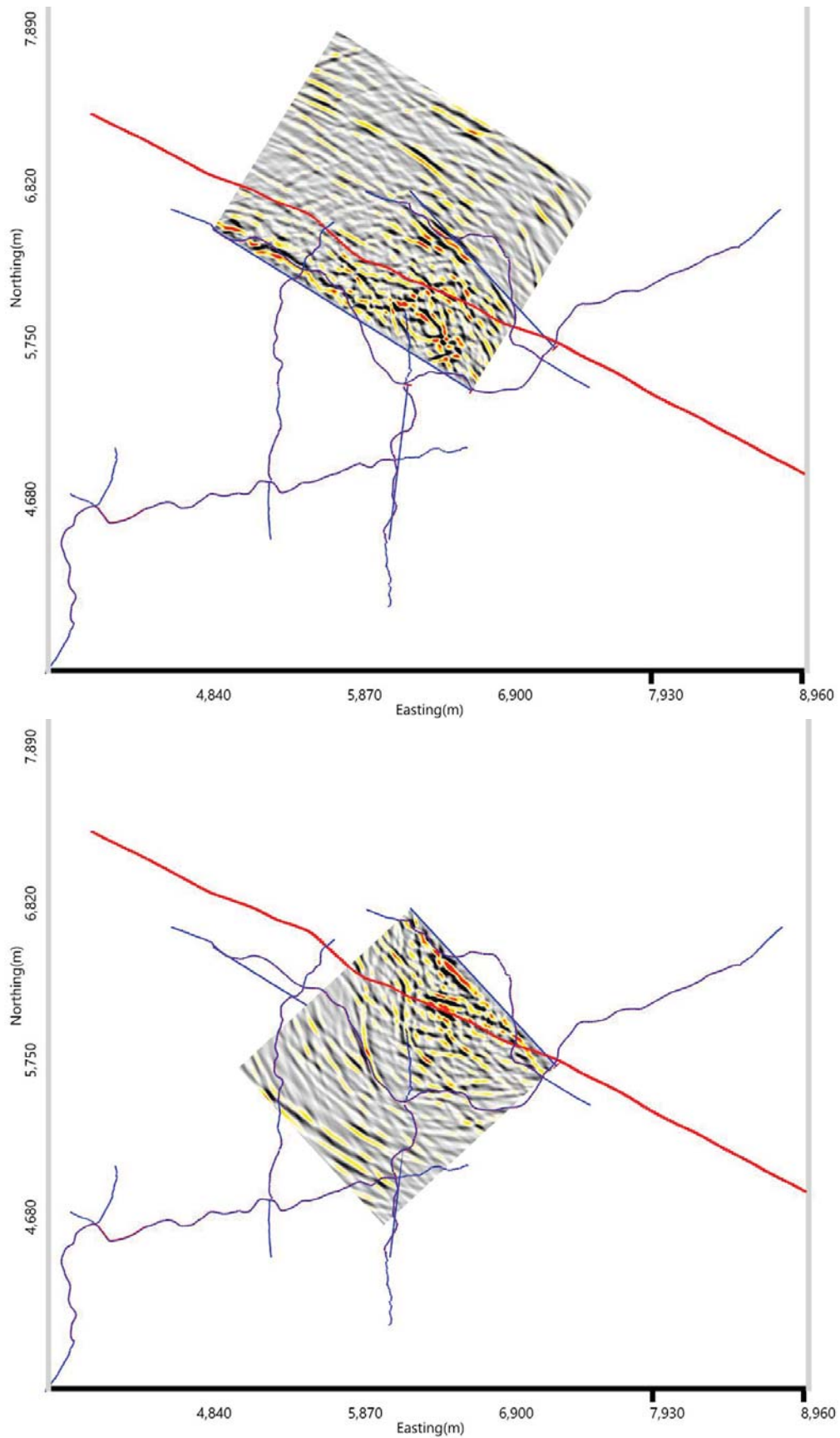


Figure 57. View from top of the horizontally migrated profiles from Line 1.2 (top) and Line 4 (bottom), together with the steeply dipping dyke (red).

It is then relevant to ask what is the likelihood of misinterpreting an off-plane subvertical feature as a sub-horizontal reflector in depth. The key difference is that horizontally refracted waves attenuate more rapidly in the less competent superficial rock layer than waves travelling in depth in nearly vertical planes. The horizontal distance from Line 1.2 to the presumed location of the dyke is around 250 - 300 m, which is mentioned above as limit for likely contamination with off-plane back scattering. In the Line 4 profile, the event presumably associated with the vertical dyke disappears abruptly at a distance from the line of 250 - 300 m. It follows that any reflector interpreted at a smaller depth than this limit should be considered carefully by also taking into account possible off-plane reflectors. The risk of misinterpretation at larger depths decreases rapidly.

5 Summary

The multi-line 2D reflection seismic program was completed in an attempt to delineate gently dipping sub-surface structural and bedrock features in the crystalline hard rock at the Revell Site.

The survey was performed in winter, on frozen trails. Recording up to 300 geophone stations instead of the 200 channels planned increased the fold and helped improving data quality. In total, six intersecting seismic profiles were processed and interpreted to image subsurface features in the study area.

The geology of the Revell Site includes sub-vertical to steeply inclined mafic dykes and a lower volume of felsic dykes with variable orientation, gently dipping amphibolites with a mean dip angle of 30°, and a discontinuous network of sub-horizontal to gently inclined fracture zones. Identifying and mapping such features by surface seismics has been challenging because of their diverse dips, and variable strikes. The seismic acquisition layout and processing routines needed to be designed with 3D imaging capabilities in mind. Moreover, the surface footprint of the survey was limited to roughly 10 km², whereas the depth of interest reached 1.5 km. This rather high vertical to horizontal ratio and the diversity of target orientations increased the complexity of the imaging task. 3D imaging was attempted by means of a multi 2D crooked line setup, with geophone extensions at the end of each line, to increase fold and extend the dip aperture. This setup proved able to map sub-horizontal and gently dipping reflectors in the required dip range and, in some cases, follow them from one adjacent profile to another. A chapter has been included focusing on steep off-line features and on means of recognizing them as possible artifacts in the downwards migrated profiles.

Reflectivity charts were inferred using local variations of velocities along each borehole. The amphibolite occurrences in boreholes proved important because they were also identified in the seismic profiles, however with limited detectable lateral extent, and were used as marker units.

Static corrections were applied using 3D tomography inversion of P-wave travel times to produce stable velocity fields.

Multiple mode propagation occurred due to the complex coupling between the shallow overburden and the upper bedrock, and scattering in the upper bedrock. Efficient signal processing routines were applied to isolate direct P-wave and S-wave direct arrivals, as well P-S conversions and interface waves at the contact of the bedrock with the overburden. P-wave reflections were thus recognized and extracted from the complex wave field produced by coherent and incoherent scatterers.

Both 3D Kirchhoff and 3D CMP Radon depth migrations were computed for all lines. The quality of the 3D Kirchhoff migration was found to be poorer than the one of its 3D CMP Radon counterpart, both in terms of noise and of recognizable coherence of events likely to be associated with P-wave seismic reflectors. With the Radon migration, reflectors are constructed as a piecewise set of oriented plane elements instead of point diffractors. This drastically reduced migration artifacts. Nonlinear signal conditioning routines were not included in the processing flow, in order to avoid potential artifacts introduced by nonlinearity. The focus in the processing was set on evidencing significant characteristics of the wave modes while observing back-traceability of all operations performed.

The P-wave velocity and density logs were used to calculate the acoustic impedance and derive the reflectivity along the BH01. Using the derived reflectivity log, a synthetic seismogram was generated and tied to the seismic data. Amphibolite layers along the borehole, as expected, resulted in reflections with high positive polarity along the synthetic seismogram. These reflections could be tied to the strong reflections in Line 1.2 and be traced along this line. This correlation suggests that strong reflections elsewhere in the seismic lines may also be caused by potential amphibolite layers. Despite interpreting these reflectors as amphibolite, it is also possible that other features, with or without a combination with amphibolite, cause these strong reflections. Therefore, it is recognized that there is remaining uncertainty in the interpretation. As more boreholes are drilled, the interpretation of these seismic reflectors will continue to be tested.

6 References

- Cosma, C., 1995. Characterisation of subsurface structures by remote sensing. Keynote address. Proceedings of the 1st International Congress on Rock Mechanics (ISRM), Tokyo, Japan.
- Cosma, C. and Heikkinen, P. 1996. Seismic Investigations for the Final Disposal of Spent Nuclear Fuel in Finland. *Journal of Applied Geophysics* vol. 35, pp. 151–157.
- Cosma, C., Olsson, O., Keskinen, J. and Heikkinen, P.J., 2001a. Seismic characterisation of fracturing at the Äspö Hard Rock Laboratory, from the kilometre scale to the meter scale. *International Journal of Rock Mechanics and Mining Sciences*, vol. 38, 6, pp.
- Cosma, C. and Enescu, N., 2001b. Characterization of Fractured Rock in the Vicinity of Tunnels by the Swept Impact Seismic Technique. *International Journal of Rock Mechanics and Mining Sciences*, vol. 38, no. 6, pp. 815 – 821.
- Cosma, C., Balu, L. and Enescu, N., 2010a. 3D VSP Migration by Image Point Transform. *Geophysics*, vol. 75, no. 3 _May-June 2010_; P. S121–S130 10.1190/1.3396316.
- Cosma, 2017. 3-D Borehole Seismic Techniques Application to Optimized Mine Development. The sixth Decennial Minerals Exploration Conference, Exploration 17, Toronto, Canada, October 2017
- Enescu, N., Cosma, C., & Balu, L. 2003. Seismic VSP and crosshole investigations in Olkiluoto, 2002. Posiva Working Report 2003-13, 131 p. (*POSIVA-2003-13_Working-report_web.pdf* available from <https://www.posiva.fi/en/index/media/reports.html>)
- Enescu, N., Cosma, C., and Balu, L. 2004. Reflection Seismics Using Boreholes at Olkiluoto in 2003 - from Investigation Design to Result Validation. Posiva Working Report 2004-62, 333 p. (*POSIVA-2004-62_Working-report_web.pdf* available from <https://www.posiva.fi/en/index/media/reports.html>)
- Enescu, N., Cosma, C., Juhlin, C., Ohman, I. and Heikkinen, E., 2008. Hard Rock High Resolution 3D Seismic Investigations at Olkiluoto, Finland, 70th EAGE Conference & Exhibition — Rome, Italy.
- Nedimovic, M. R. and West, G., 2003a. Crooked-line 2D seismic reflection imaging in crystalline terrains: Part 1, data processing. *Geophysics*, Vol. 68, No. 1 (Jan-Feb 2003); P. 274–285, 10.1190/1.1543213
- Nedimovic, M. R. and West, G., 2003b. Crooked-line 2D seismic reflection imaging in crystalline terrains: Part 2, migration. *Geophysics*, Vol. 68, No. 1 (Jan-Feb 2003); P. 286–296, 10.1190/1.1543214
- Park, C.B., Miller, R.D., Steeples, D.W. and Black, R.A. 1996. Swept Impact Seismic Technique (SIST). *Geophysics*, vol. 61, no. 6, pp.1789 – 1803.
- Parmenter, A., Waffle, L., DesRoches, A. 2020. An updated bedrock geology map and geological database for the northern portion of the Revell Batholith (No. NWMO-TR-2020-08). Nuclear Waste Management Organization.

Parmenter, A., Waffle, L., DesRoches, A. 2021b (*in prep*). Phase 2 Initial Borehole Drilling and Testing, Ignace Area. WP10 – Geological Integration Report for Borehole IG_BH02 (no. APM-REP-01332-0265). Nuclear Waste Management Organization

Parmenter, A., Waffle, L., DesRoches, A. 2021c (*in prep*). Phase 2 Initial Borehole Drilling and Testing, Ignace Area. WP10 – Geological Integration Report for Borehole IG_BH03 (no. APM-REP-01332-0266). Nuclear Waste Management Organization.

Parmenter, A., Waffle, L., DesRoches, A., Carvalho, J., Neufeld, A. 2021a (*in prep*). Phase 2 Initial Borehole Drilling and Testing, Ignace Area. WP10 – Geological Integration Report for Borehole IG_BH01 (no. APM-REP-01332-0260). Nuclear Waste Management Organization.

Golder (Golder Associates Ltd.) and PGW (Paterson, Grant, and Watson), 2017. Phase 2 Geoscientific Preliminary Assessment, Geological Mapping, Township of Ignace and Area, Ontario. Prepared for Nuclear Waste Management Organization (NWMO). NWMO Report APM-REP-01332-0225. Mississauga, Canada.

DesRoches, A., Waffle, L., Parmenter, A. 2021. 3D Site-Scale Geological Model in the Revell Batholith: Model Version 1.0 (No. NWMO-TR-2021-12). June 2021. Nuclear Waste Management Organization.

Golder Associates Ltd., 2018a. Phase 2 Initial Borehole Drilling and Testing, Ignace Area: WP2 Data Report - Borehole Drilling and Coring for IG_BH01 (No. APM-REP-01332-0229). Nuclear Waste Management Organization.

Golder Associates Ltd., 2019. Phase 2 Initial Borehole Drilling and Testing, Ignace Area: WP5 Data Report - Geophysical Well Logging for IG_BH01 (No. APM-REP-01332-0234). Nuclear Waste Management Organization.

Golder Associates Ltd., 2020a. Phase 2 Initial Borehole Drilling and Testing, Ignace Area. WP02 Data Report - Borehole Drilling and Coring for IG_BH303 (No. APM-REP-01332-0241). Nuclear Waste Management Organization.

Golder Associates Ltd., 2020b. Phase 2 Initial Borehole Drilling and Testing, Ignace Area. WP05 Data Report - Geophysical Well Logging for IG_BH03 (No. APM-REP-01332-0268). Nuclear Waste Management Organization.

Golder Associates Ltd., 2020d. Phase 2 Initial Borehole Drilling and Testing, Ignace Area. WP02 Data Report – Borehole Drilling and Coring for IG_BH02 (No. APM-REP-01332-0240). Nuclear Waste Management Organization.

Golder Associates Ltd., 2020f. Phase 2 Initial Borehole Drilling and Testing, Ignace Area. WP05 Data Report – Geophysical Well Logging for IG_BH02 (No. APM-REP-01332-0269). Nuclear Waste Management Organization.

NWMO, Nuclear Waste Management Organization, 2010. Moving Forward Together: Process for Selecting a Site for Canada's Deep Geological Repository for Used Nuclear Fuel, Nuclear Waste Management Organization. (Available at www.nwmo.ca).

Appendix A. Synthetic seismograms

P-wave sonic, S-wave sonic and density logs were available for three boreholes (IG_BH01, IG_BH02 and IG_BH03), for which these were used to compute Zoeppritz synthetics with several minimum phase wavelets, in the frequency bands 10 – 50 Hz, 10 – 100 Hz and 10 – 150 Hz. Only the results for borehole IG_BH01 are shown here, as only these were used for depth calibration of the 2D lines depth migrations. The wavelets used for the synthetics generation are shown in Figure 58, while the synthetic seismograms computed in the three frequency bands are shown in Figure 59. The seismograms were calculated for offsets ranging from 0 to 2000 m, hence at various incidence angles, on time windows from 0 to 360ms for IG_BH01, while the corresponding TVD depth interval is as listed in the figure caption. This interval was chosen from just below the borehole casing to the bottom of the borehole.

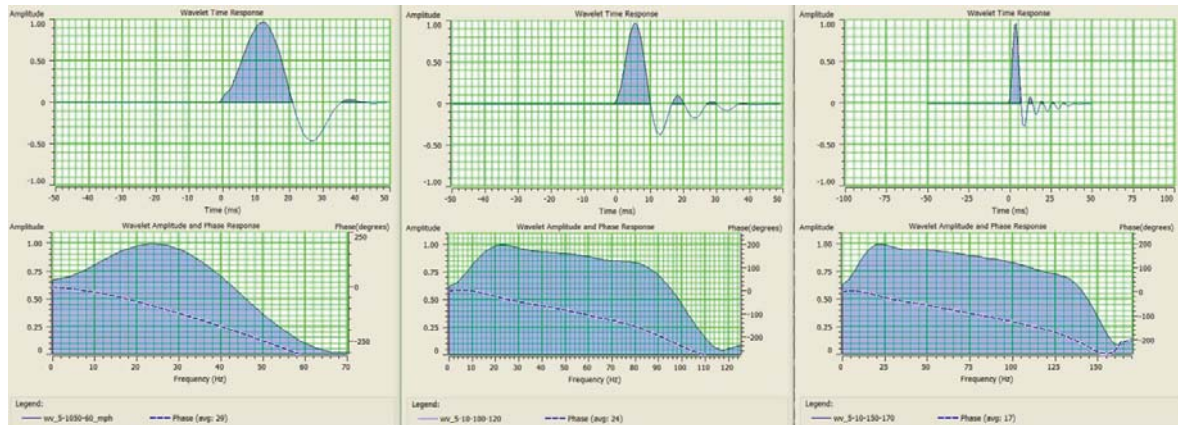


Figure 58. Wavelets and their amplitude and phase spectra for the minimum phase wavelets used for generating the synthetic seismograms for the Ignace site boreholes.

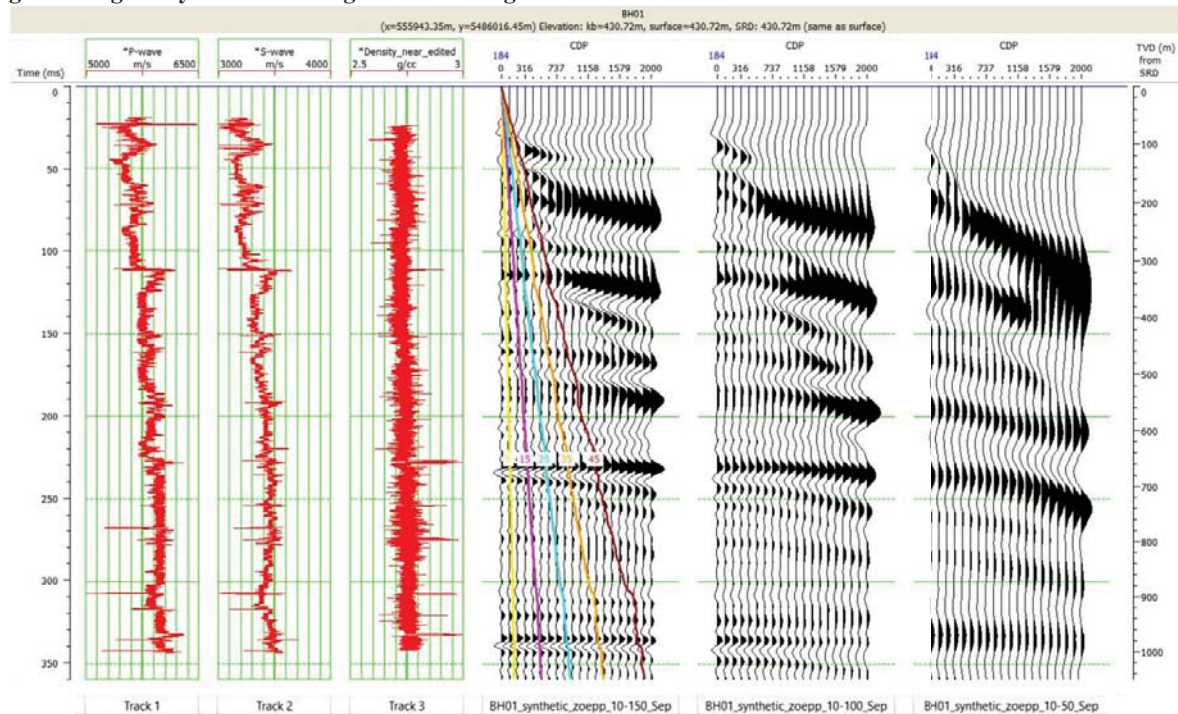


Figure 59. Zoeppritz synthetics along borehole IG_BH01, on a time interval from 0 to 360 ms, corresponding to a TVD interval from 70 to 1000m. Colored lines on the 10 – 150 Hz CDP gather mark inclined incidence angles (15, 25, 35 and 45 degrees) with respect to the vertical (shown as the yellow line, labeled 0). The next synthetic gathers were computed in the 10 – 100 Hz and 10 – 50 Hz bands, respectively.

Figure 60 illustrates a comparison between the migrated profile of Line 1.2, the closest to borehole IG_BH01, and two synthetic gathers, computed in the 10 – 50 Hz and 10 – 100 Hz frequency band.

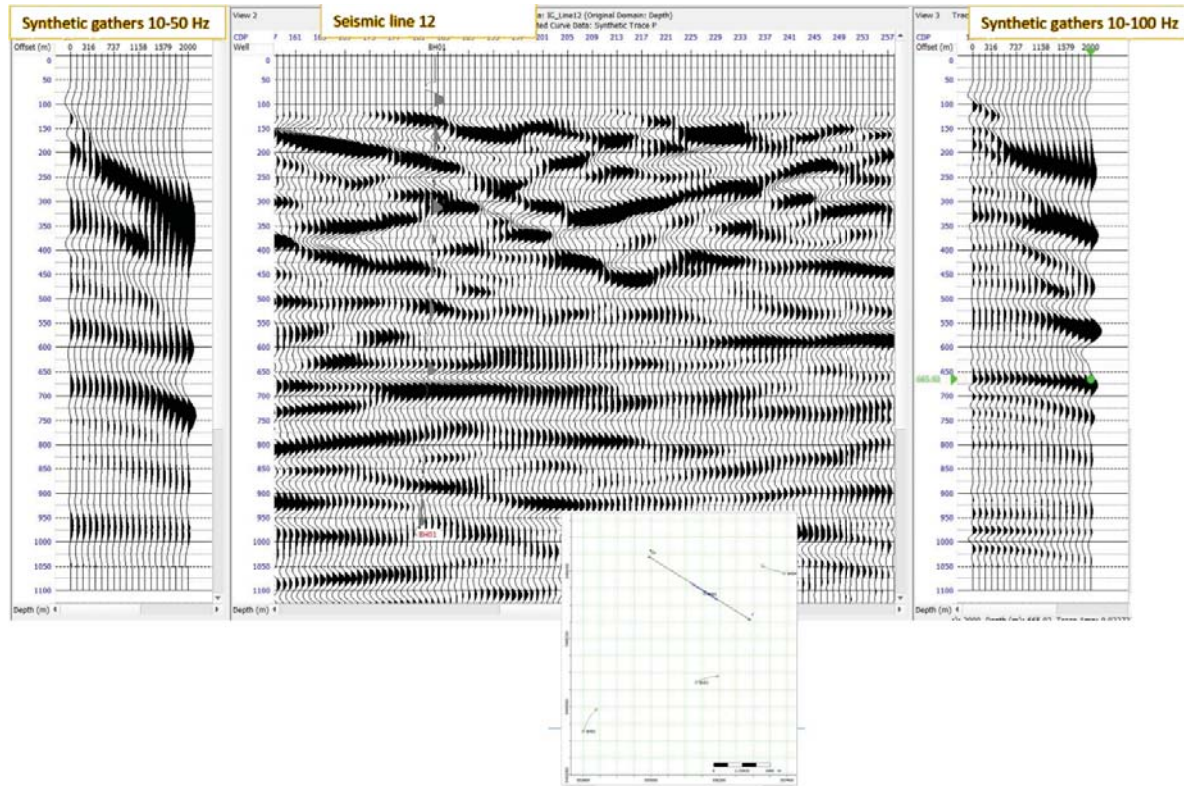


Figure 60. Line 1.2 migrated section (middle), with the synthetic seismograms along borehole IG_BH01, in depth (TVD), on the left the lower frequency synthetic gather (10 – 50 Hz) and on the right the higher synthetic gather (10 – 100 Hz) on which the amphibolite “marker” reflector at 665.93m (this depth corresponds to peak amplitude of the reflector) in borehole IG_BH01 is underlined by the green dot and arrow. This “marker” reflector corresponds to the prominent density log variation at 660m, as seen in Figure 61.

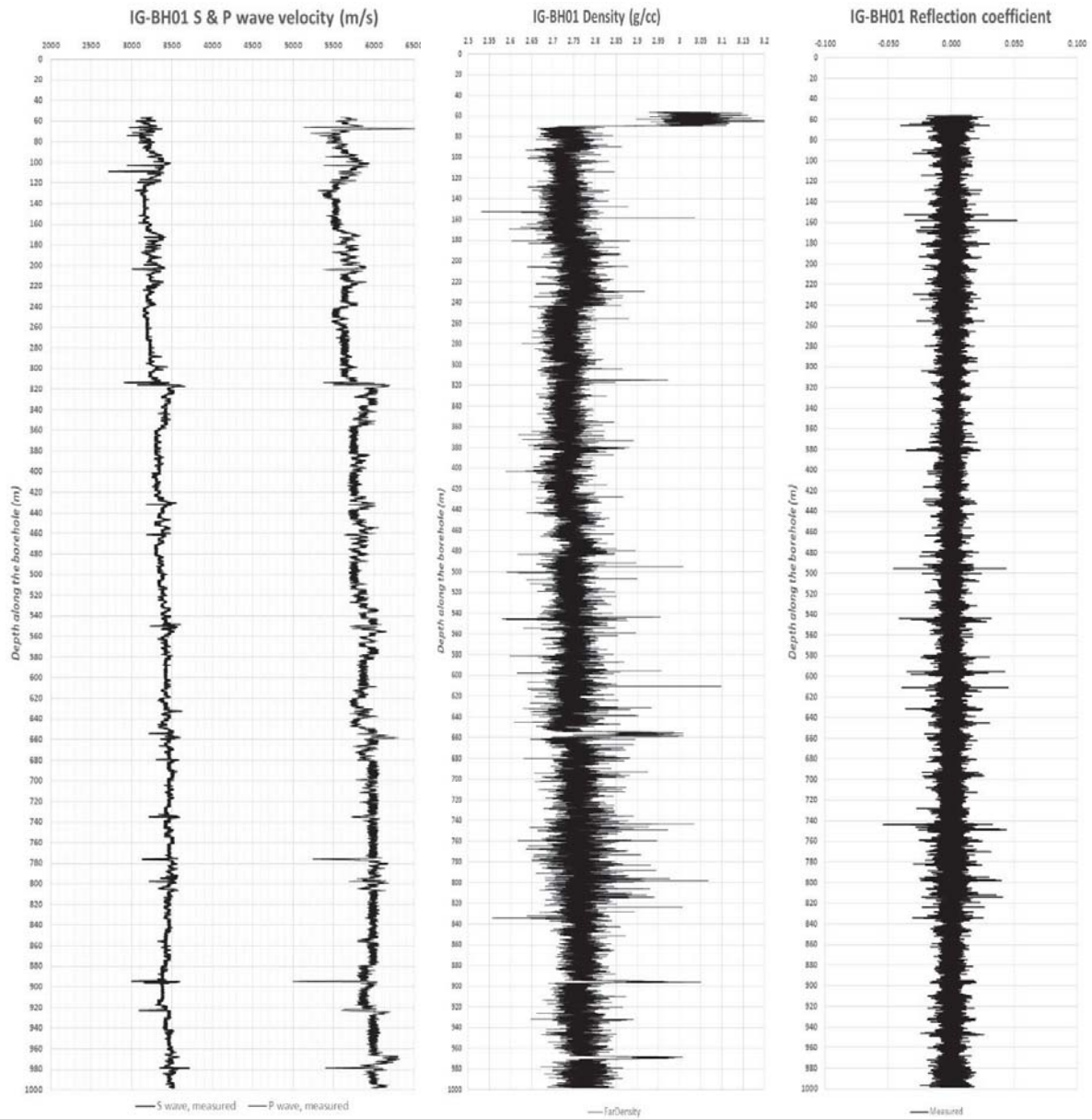


Figure 61. Borehole IG-BH01 logs: S & P wave velocities, density and reflectivity.

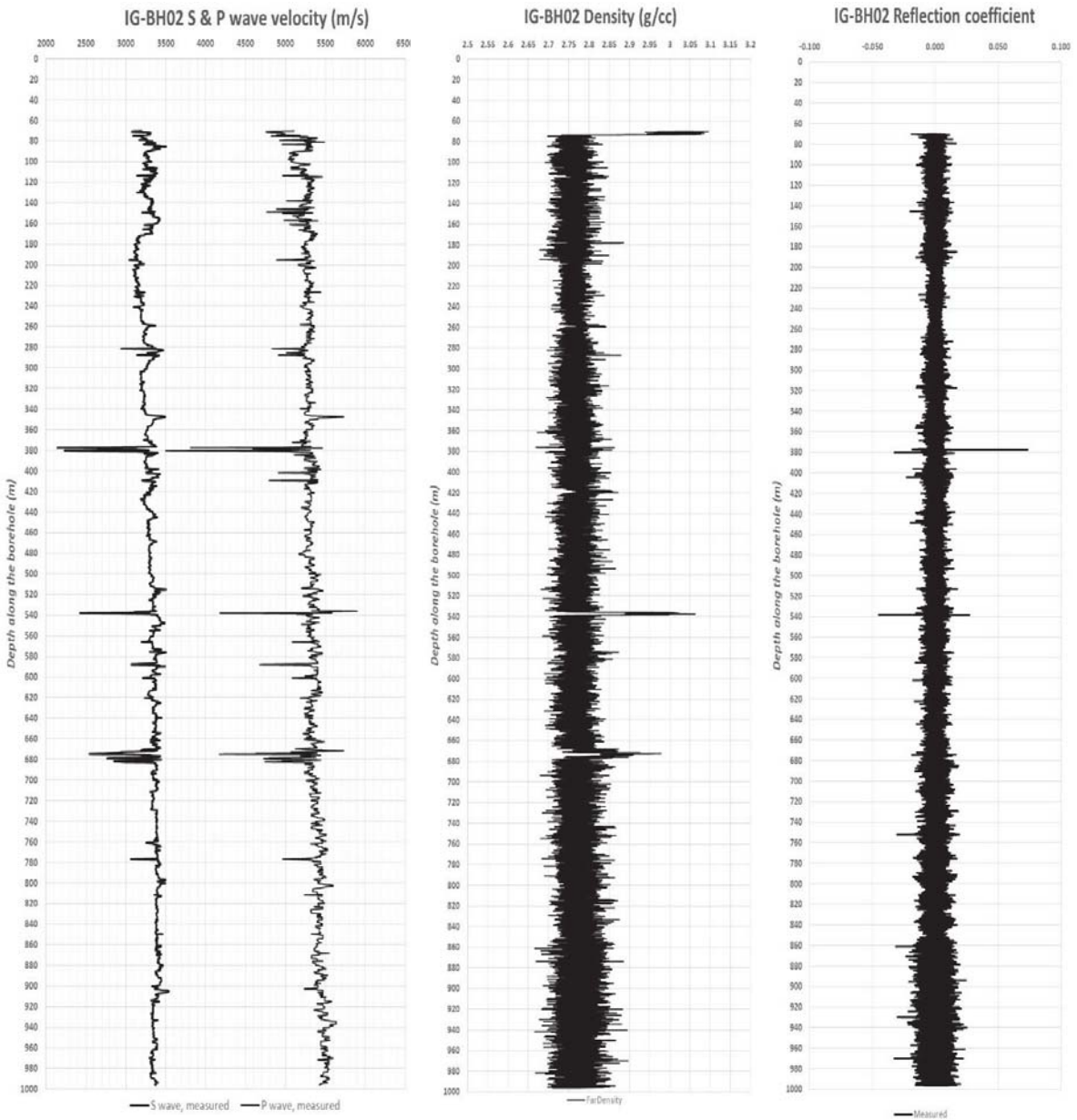


Figure 62. Borehole IG-BH02 logs: S & P wave velocities, density and reflectivity.

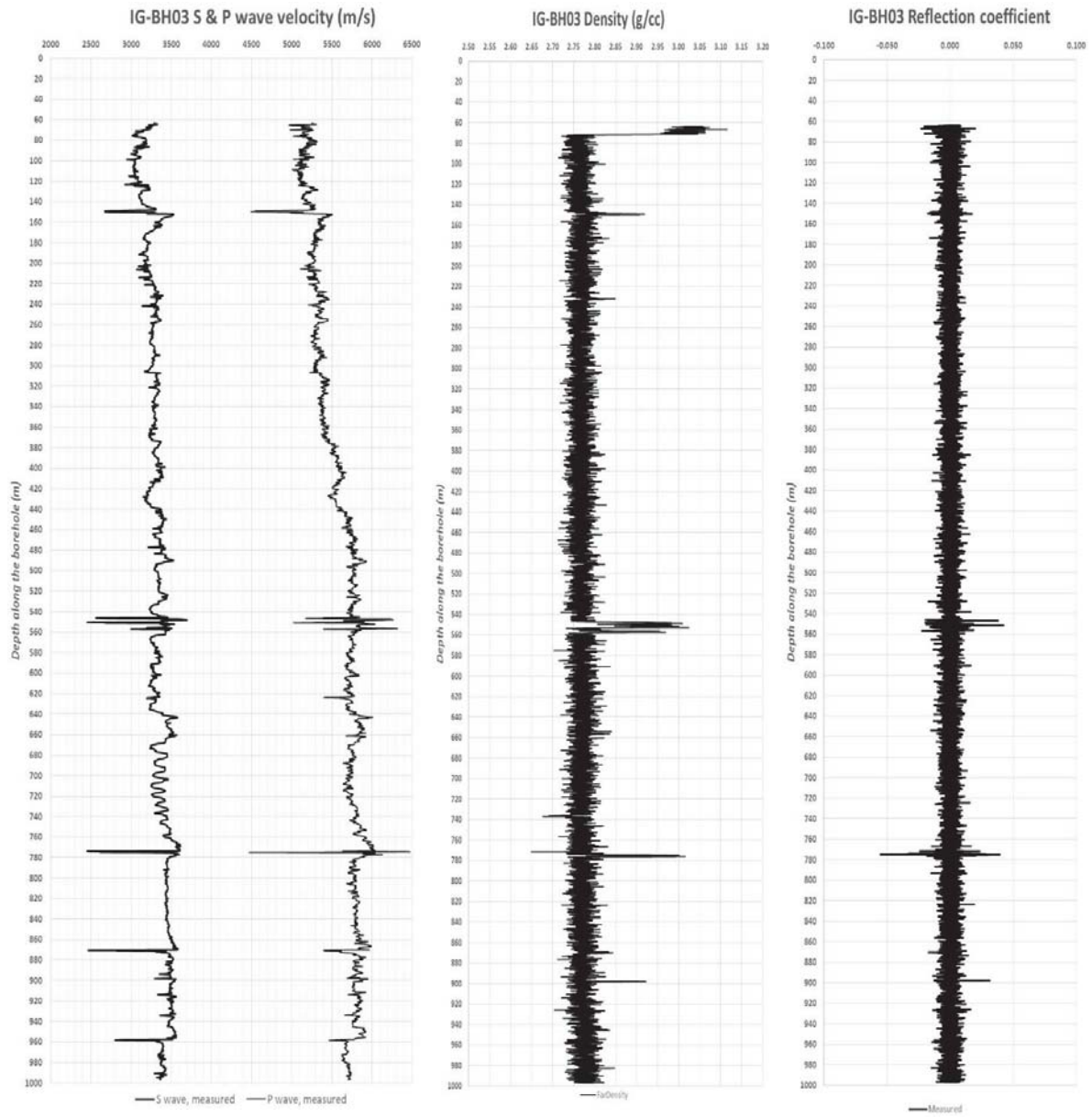


Figure 63. Borehole IG-BH03 logs: S & P wave velocities, density and reflectivity.

Appendix B. The CMP Radon 3D migration method

Vibrometric developed a proprietary procedure for 3D rock imaging by using multiple and/or crooked 2D lines, as well as VSP and cross-hole setups, starting from a variation of the CMP (Common Mid-Point) stack and a version of the Radon transform similar in many ways to the τ - p transform.

With CMP stacking the reflections from different source and receiver locations (but with the same source-receiver midpoint) are enhanced by summing the traces after removing the travel time shifts due to different propagation paths, i.e. performing move-out corrections. With parallel sources and receiver lines laid on surface (or in boreholes), the source-receiver midpoints are distributed along the median line of the boreholes and it is reasonable to compute the move-out corrections with respect to this line. If non-parallel or crooked lines are used in a truly 3D environment, the term

Common Mid-Point loses its meaning, as the reflected wave paths must be computed as a function of the depth, and local dip and strike of each potential target.

In this case, the move-out correction depends on the angle θ between the normal to the reflector and the Z -axis, which is defined to be the best 3D linear approximation of the positions of all the stations in the set to be processed. Because the sources and the receivers are not along the same line, the correction also depends on the azimuth ϕ . Therefore, the stacking must be computed for the whole range of θ - ϕ combinations.

The move out correction Δt is the difference between the true travel time of the reflection and the two-way travel time t_z from the source-receiver midpoint (M) to the same planar reflector. The correction Δt depends on θ and the azimuth ϕ :

$$\Delta t = \sqrt{t_z^2 + (\Delta z/c)^2 + (\Delta x/c)^2 - (\Delta z \cos(\theta) + \Delta x \sin(\theta) \cos(\phi))^2 / c^2} - t_z \quad (\text{B.1})$$

where

$$t_z = 2h_z/c; \quad \Delta z = z_s - z_d$$

The parameter h_z is the distance from the reflector to the midpoint, z_s and z_d are the source and reflector positions along the midline and Δx is the lateral distance between source and receiver.

At each midpoint $z = (z_s + z_d)/2$ the traces are stacked after move out correction:

$$g_\phi(z, \theta, t_z) = \sum_s \sum_d G(z_s, z_d, t = t_z + \Delta t(\theta, \phi, t_z)) \quad (\text{B.2})$$

where $G(z_s, z_d, t)$ is the trace recorded at the receiver position z_d from the source point z_s and $g_\phi(z, \theta, t_z)$ is the stacked trace at the midpoint z .

In each stacked section the reflections which have the values of θ and ϕ close to the ones used in the move-out correction will be summed constructively. Events from reflectors with different orientations will be suppressed. It is thus possible to estimate the 3D-orientation of the reflectors by calculating the stack for different values of θ and ϕ and comparing the sections.

A limitation appears in the case of straight, parallel source-receiver arrays and reflectors nearly parallel to the midline, as defined above. For these reflectors the value of θ is close to 90° , and the correction (5.49) simplifies to the form:

$$\Delta t \approx \sqrt{t_z^2 + (\Delta z/c)^2 + (\Delta x \sin(\phi)/c)^2} - t_z \quad (\text{B.3})$$

If the move out correction is calculated using a wrong value of ϕ , the reflections in different traces (different Δz) are still in phase and add up constructively in stacking, although at a wrong value of t_z . In other words, the events parallel to the midline appear at all azimuths but with different two-way travel times t_z . This limitation does not appear for crooked lines and it is therefore important to conserve the original geometry through the whole process, avoiding projections to a given datum or any other arbitrary level or line.

If stacking were performed, e.g. for 36 values of the azimuth ϕ (i.e. each 10°) and 180 values of the dip θ , the number of different sections would be 6480, which are obviously too many to be of any practical use. A key observation, which also constitutes the core of the idea of the method, is that in each section we are only interested in reflectors with the same orientation as used when computing the moveout correction for that specific section. These reflections follow straight lines in the respective moveout section and therefore have a constant slowness p . The slowness can be expressed as

$$p = \cos(\theta)/v, \quad (\text{B.4})$$

where v is the seismic velocity and θ the dip of the reflector. It is therefore possible to reduce the relevant information in a moveout section to only one trace by slant-stacking along the slowness p , corresponding to the dip θ used in the move-out correction. Each moveout section produces thus one trace

$$\Gamma_\phi(p, \tau) = \sum_z g_\phi(z, \theta; t_z = \tau + pz) \quad (\text{B.5})$$

The procedure is equivalent to performing a τ - p transform for only one slowness p . By repeating the operation with a certain increment of the slowness p and arranging them one below another in the same profile, a complete τ - p section is obtained where each p trace is related to the dip θ by the expression (5.4)

The inverse τ - p transform:

$$\gamma_\phi(z, t) = \sum_p \Gamma_\phi(z, \tau = t - pz) \quad (\text{B.6})$$

reproduces a move-out section containing reflections with all the possible dips, for the specified azimuth. A complete image of the reflectors with the same azimuth ϕ is therefore obtained. After that, the sections can be compared directly with the geological structures of the site and the transmission tomograms.

The final processing result consists of one trace for each azimuth. However, the number of sections is relatively small and therefore easy to interpret.

In the discussion above, we assumed a constant velocity. If the velocity varies considerably, the reflections would not stack constructively. A procedure similar to the one used for variable velocity IP transform is used to compute corrected travel times

Reflections can be enhanced using coherency of the signals along the stacking path, for example by multiplying the stacked trace with the semblance of the nearby traces:

$$\Gamma_{\phi}(p, \tau) = \sum_z g_{\phi}(z, \theta; t_z = \tau + pz) S(z; p, \tau) \quad (\text{B.7})$$

The semblance S is defined as

$$S(z; p, \tau) = \frac{\sum_{\delta=-T}^T \left(\sum_{\xi=-\Delta z}^{\Delta z} g_{\phi}(z' = z + \xi, \theta, t_z = \tau + pz + \delta) \right)^2}{N \left(\sum_{\xi=-\Delta z}^{\Delta z} \sum_{\delta=-T}^T g_{\phi}(z' = z + \xi, \theta, t_z = \tau + pz + \delta) \right)^2}, \quad (\text{B.8})$$

where N is the number of traces within the window $(z - \Delta z, z + \Delta z)$ used in the semblance calculations.

Appendix C. Kirchhoff migrated sections

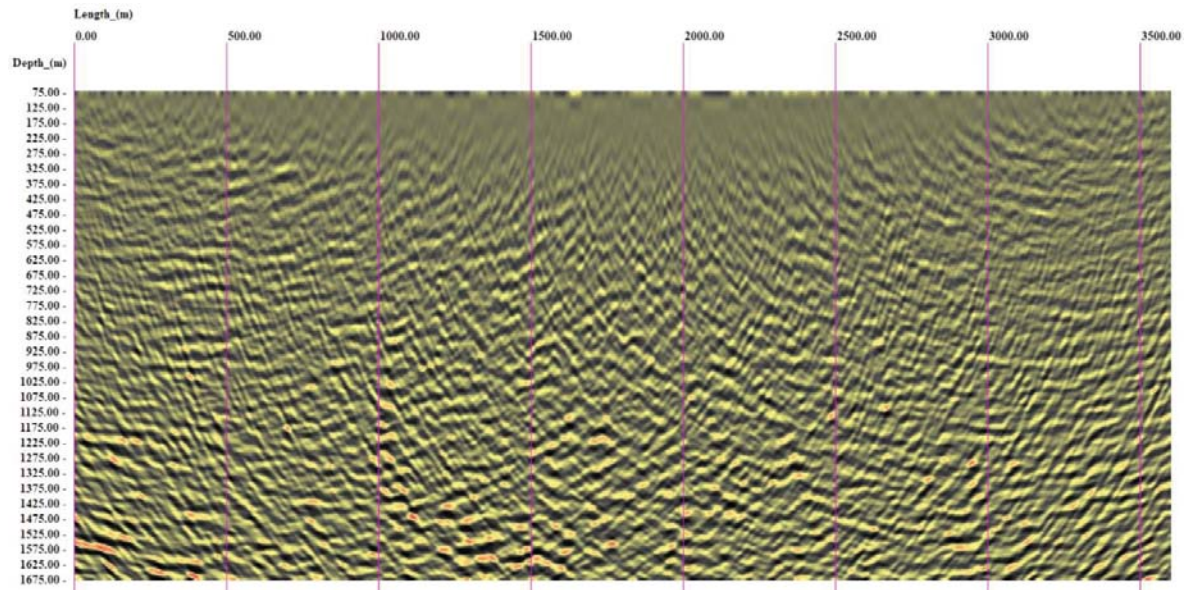


Figure 64. Line 1, Kirchhoff migration with amplitude equalization & trace balancing.

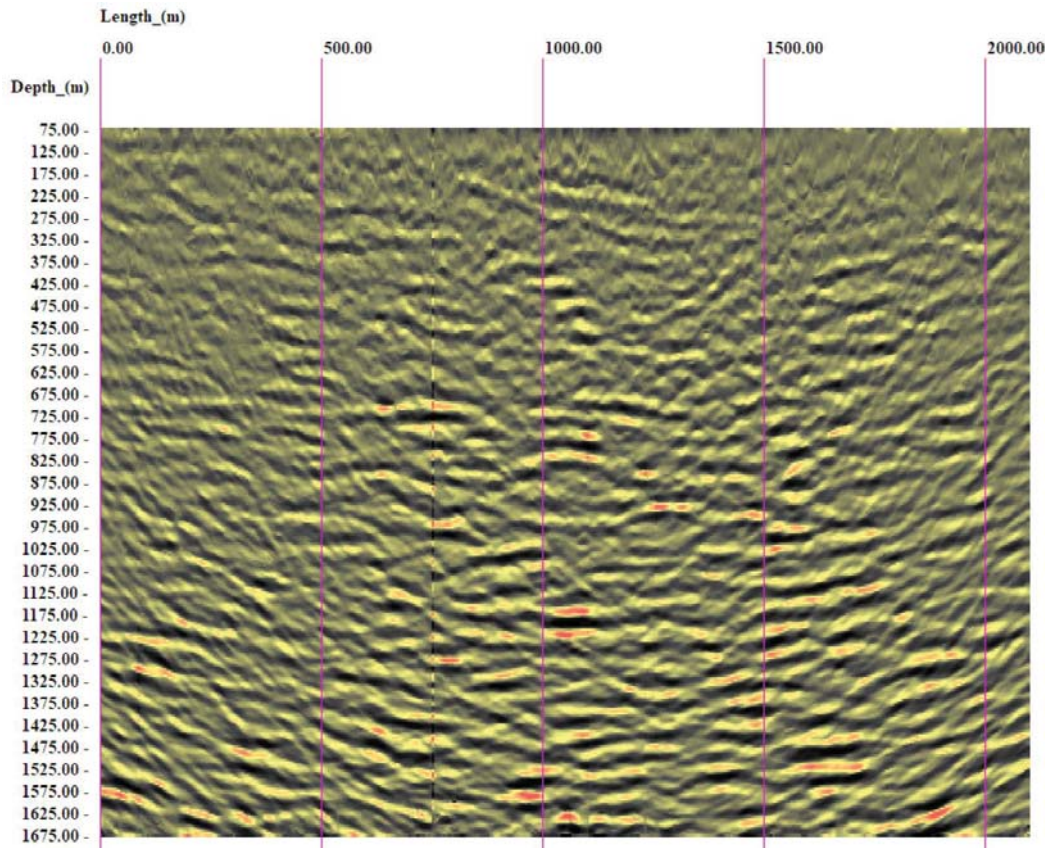


Figure 65. Line 1.1, Kirchhoff migration with amplitude equalization & trace balancing.

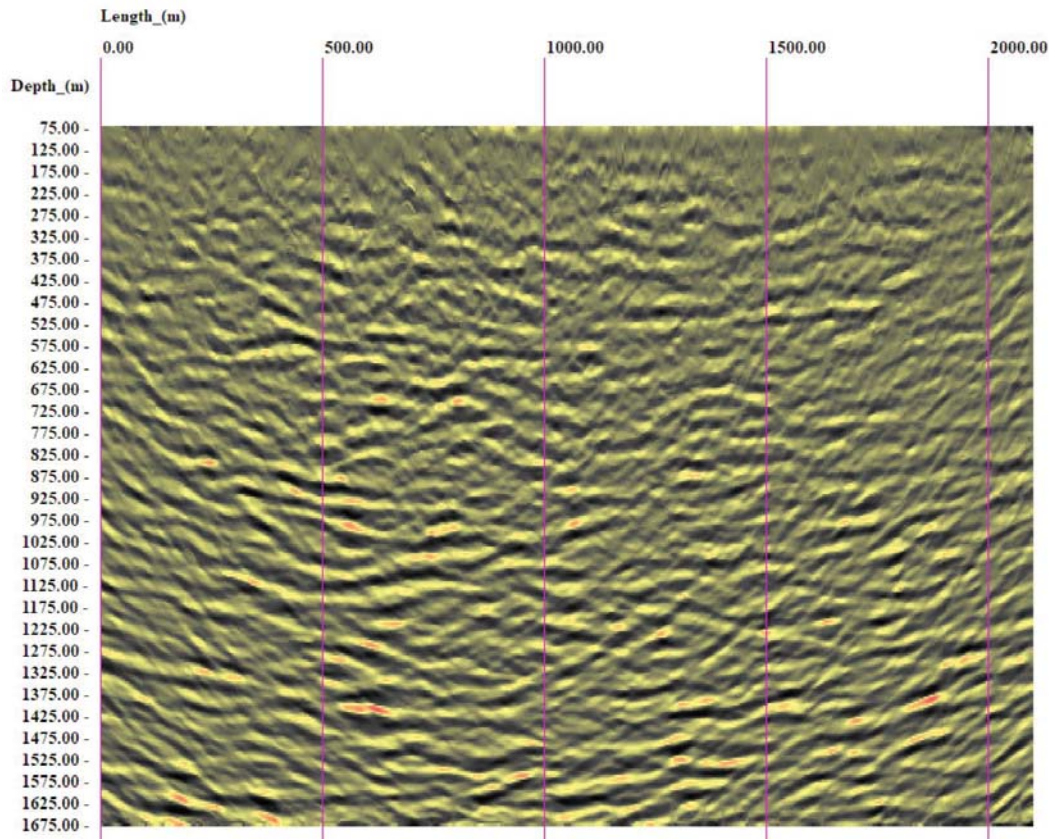


Figure 66. Line 1.2, Kirchhoff migration with amplitude equalization & trace balancing.

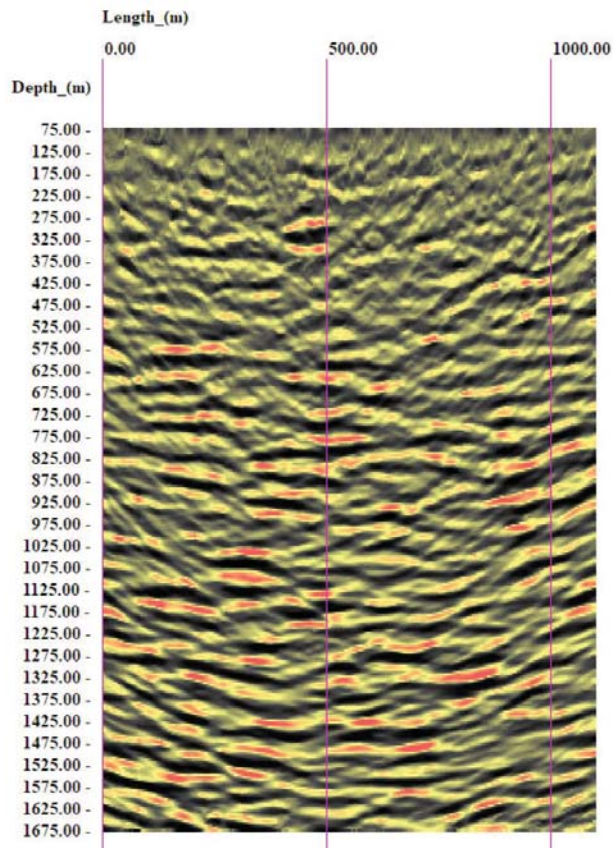


Figure 67. Line 2, Kirchhoff migration with amplitude equalization & trace balancing.

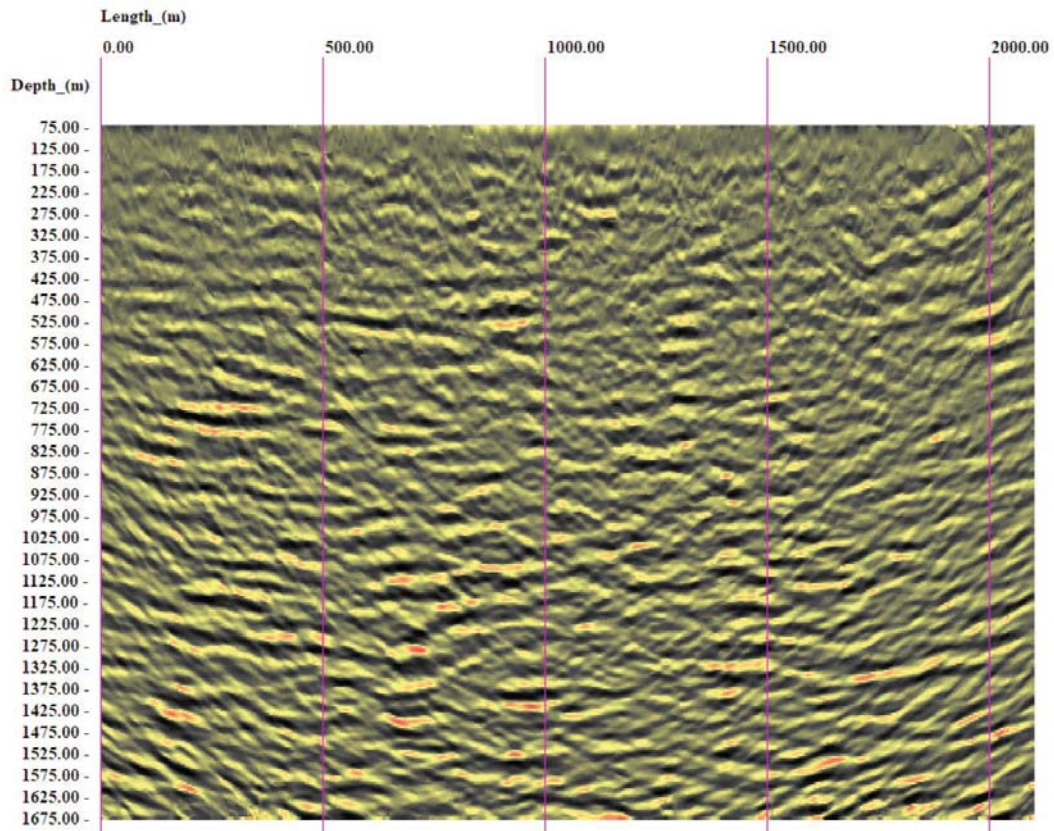


Figure 68. Line 3, Kirchhoff migration with amplitude equalization & trace balancing.

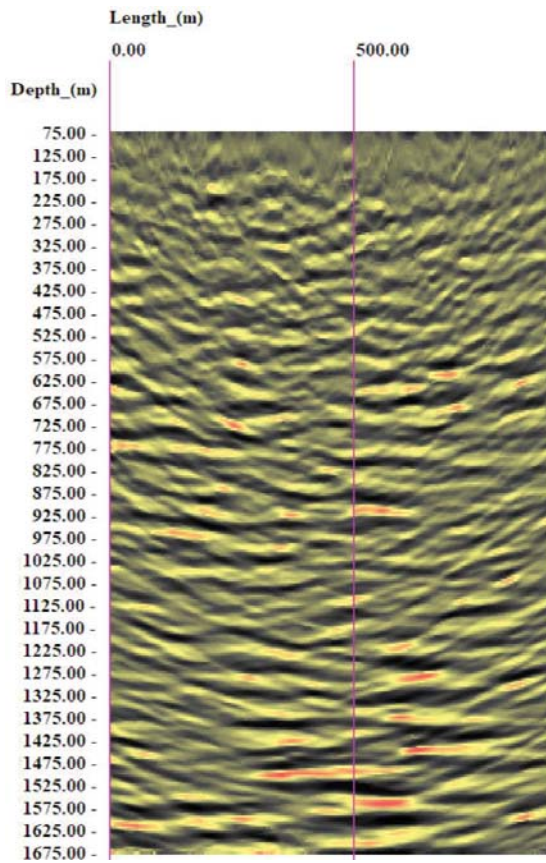


Figure 69. Line 3.1, Kirchhoff migration with amplitude equalization & trace balancing.

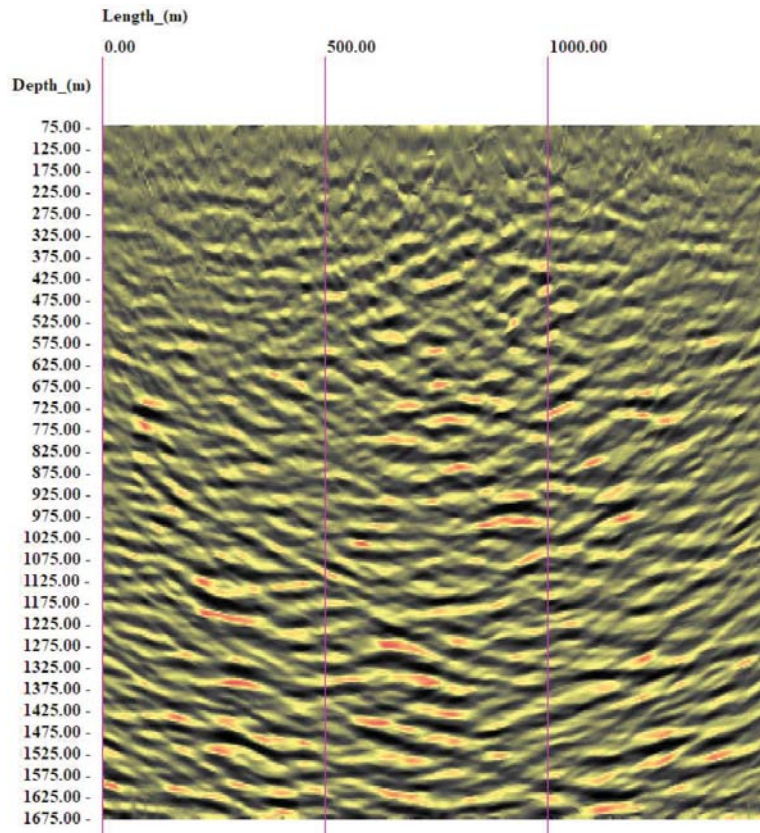


Figure 70. Line 4, Kirchhoff migration with amplitude equalization & trace balancing.

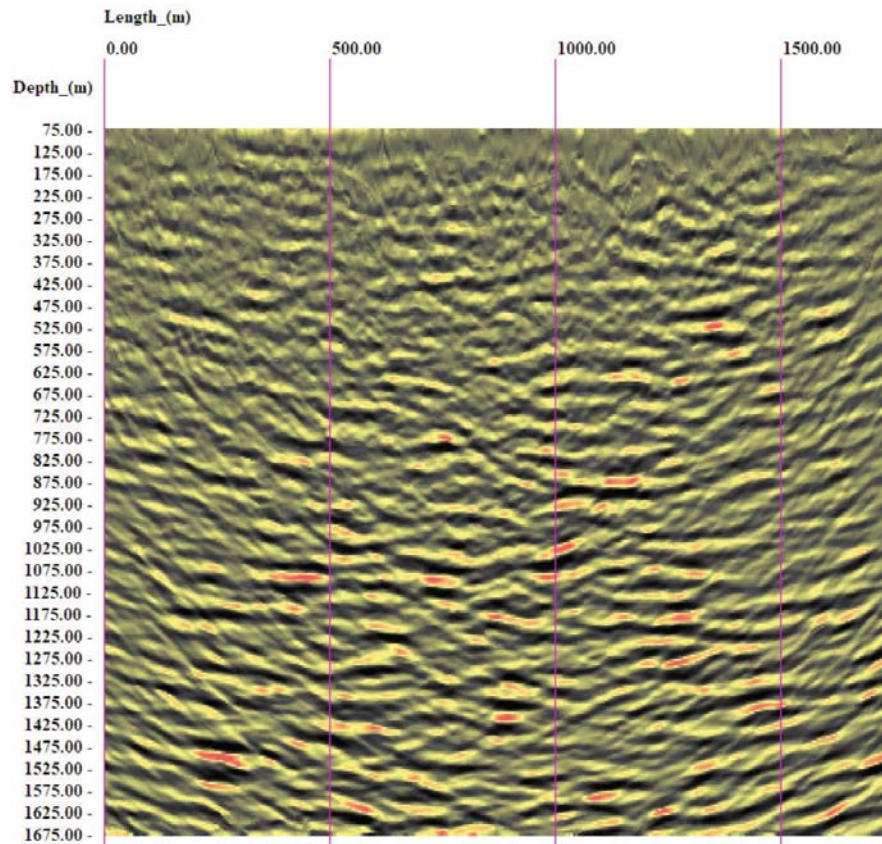


Figure 71. Line 5, Kirchhoff migration with amplitude equalization & trace balancing.

Appendix D. Reflector interpretation

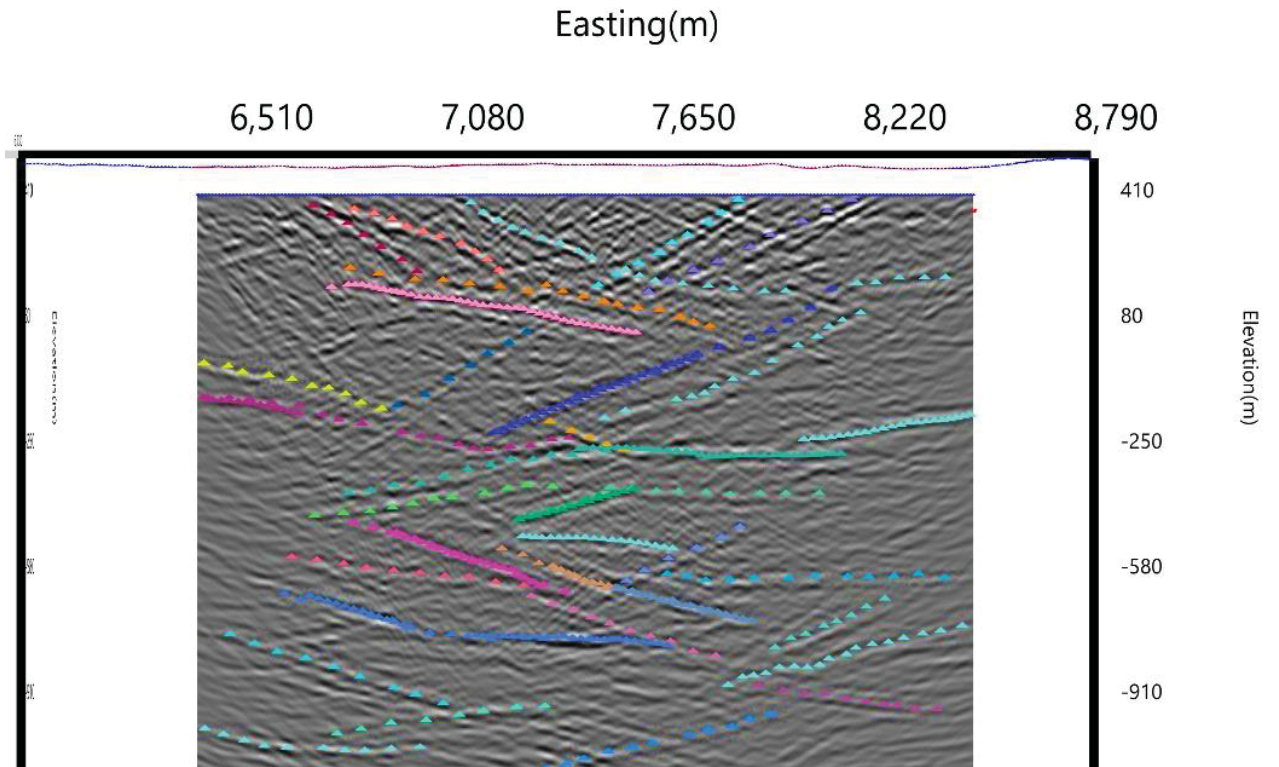


Figure 72. Interpreted seismic reflectors on Line 1.1 (same as in Figure 34), view from SE.

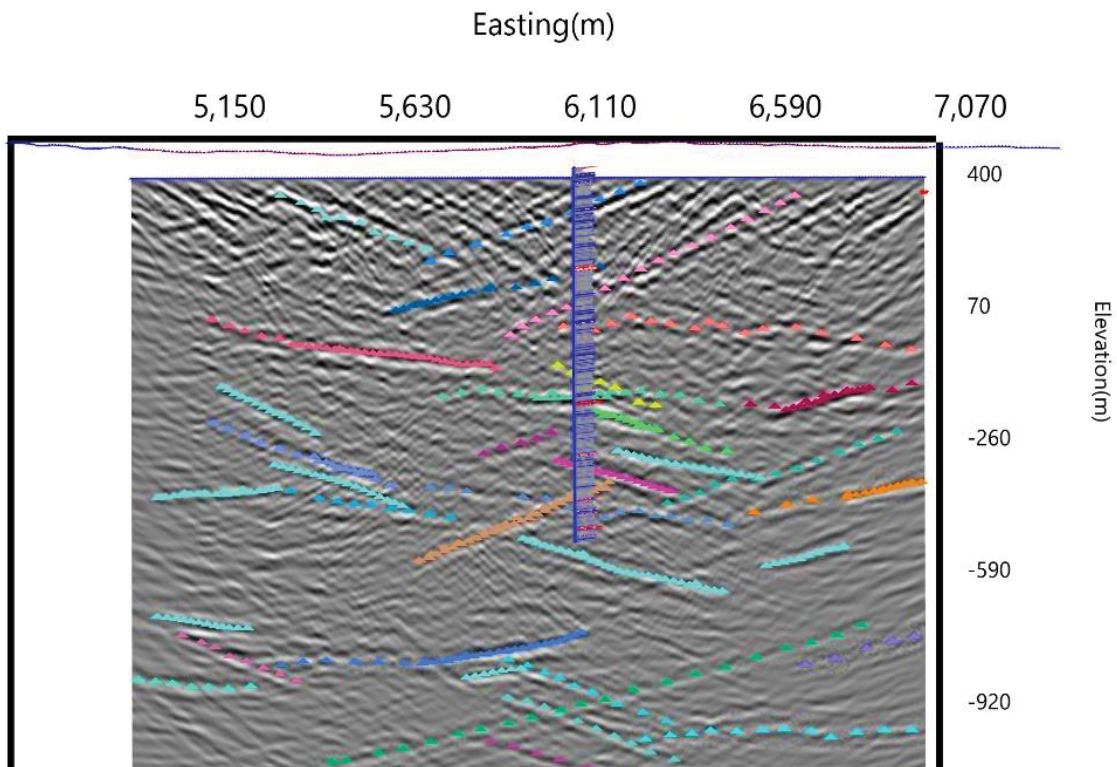


Figure 73. Interpreted seismic reflectors on Line 1.2 (same as in Figure 36), together with the seismic reflectivity log along borehole IG-BH01 (also shown in Figure 61), view from SW.

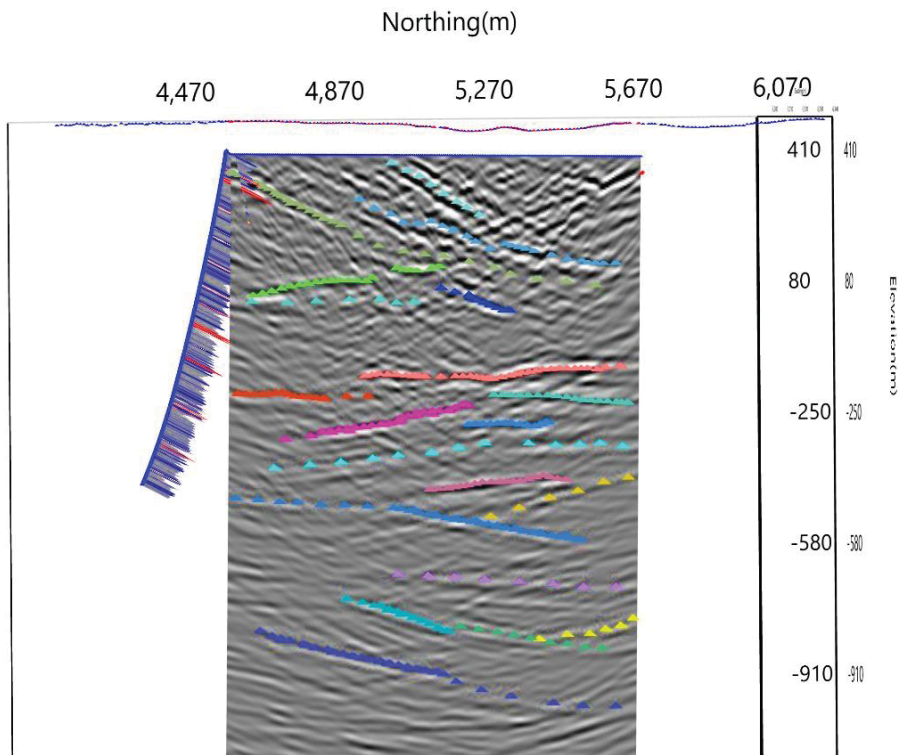


Figure 74. Interpreted seismic reflectors on Line 2 (same as in Figure 38), together with the seismic reflectivity log along borehole IG_BH03 (also shown in Figure 63), view from E.

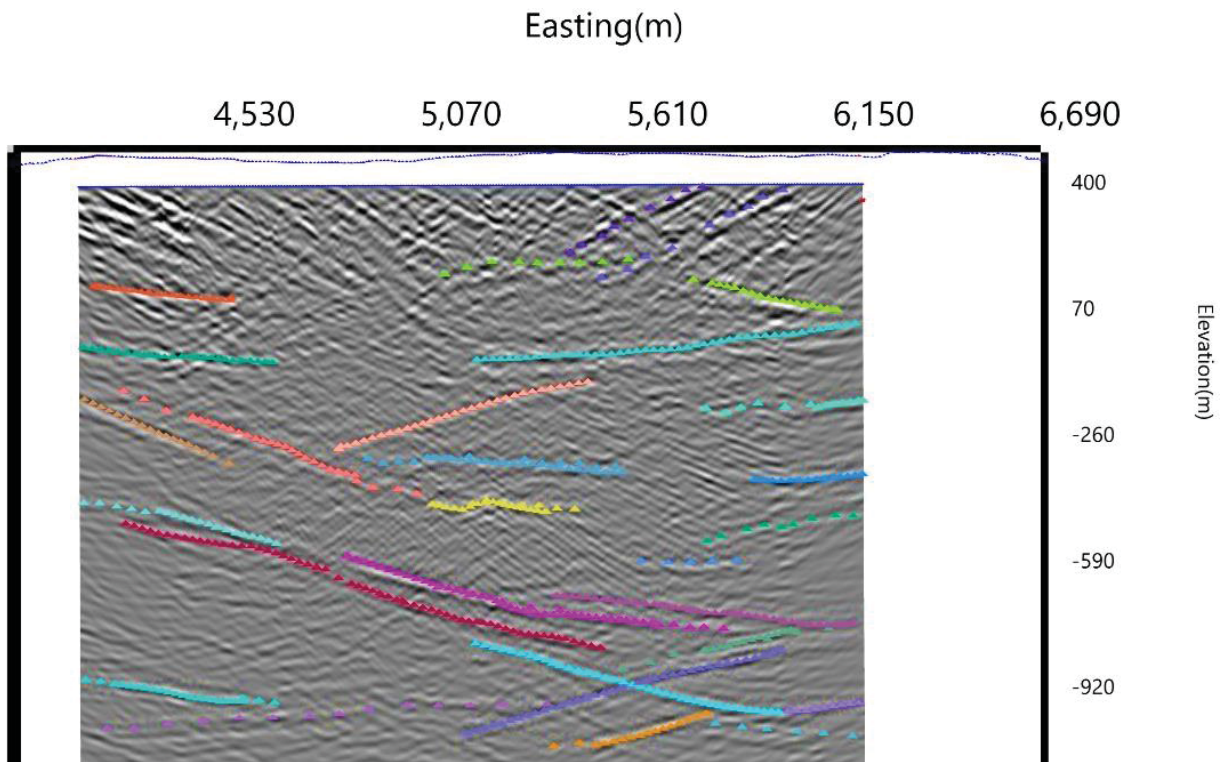


Figure 75. Interpreted seismic reflectors on Line 3 (same as in Figure 40), view from S.

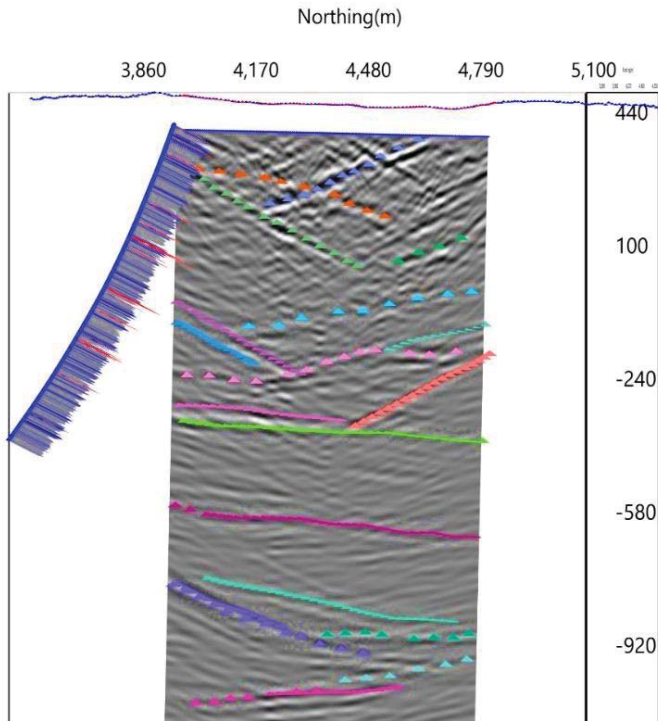


Figure 76. Interpreted seismic reflectors on Line 3.1 (same as in Figure 42) together with the seismic reflectivity log along borehole IG_BH02 (also shown in Figure 62), view from E.

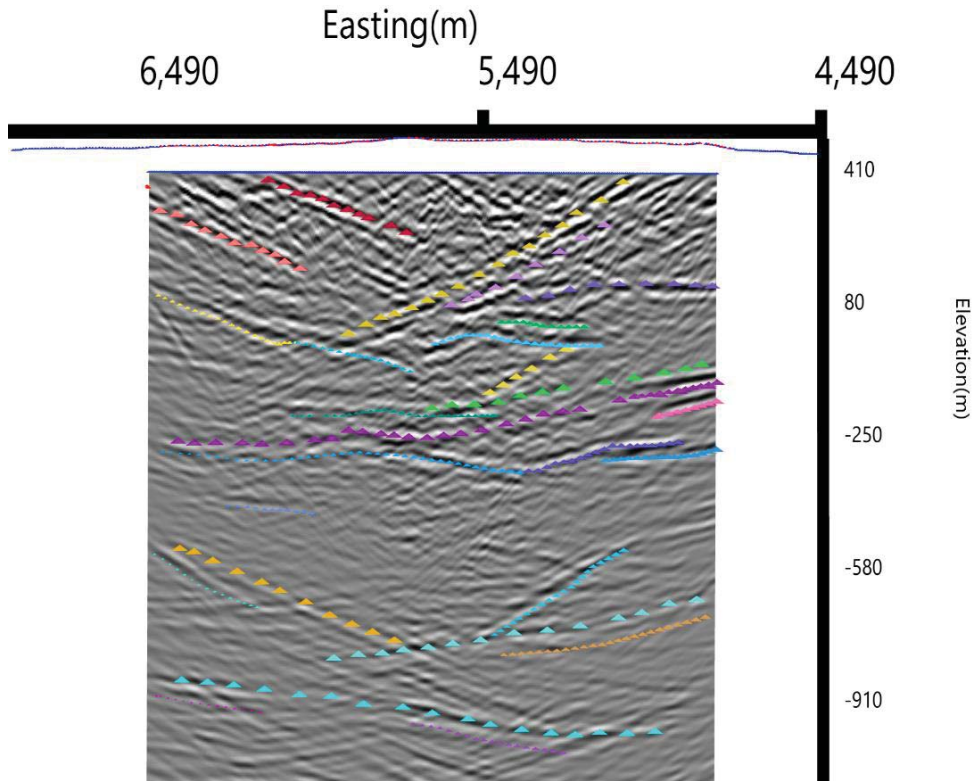


Figure 77. Interpreted seismic reflectors on Line 4 (same as in Figure 44), view from NE.

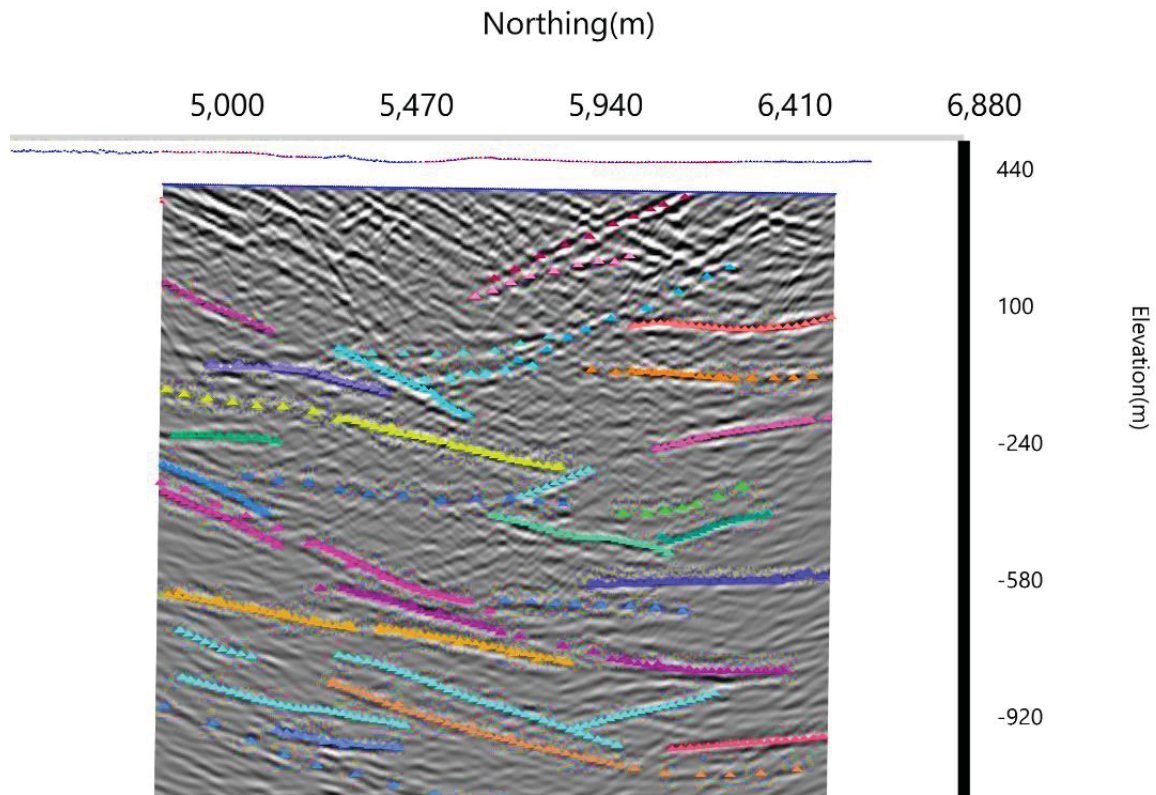


Figure 78. Interpreted seismic reflectors on Line 5 (same as in Figure 46), view from E.